

DEPARTMENT OF MECHANICAL ENGINEERING  
COLLEGE OF ENGINEERING & TECHNOLOGY  
OLD DOMINION UNIVERSITY  
NORFOLK, VIRGINIA 23529

**RADIATIVE INTERACTIONS IN MULTI-DIMENSIONAL  
CHEMICALLY REACTING FLOWS USING MONTE CARLO  
SIMULATIONS**

By

Jiwen Liu, Graduate Research Assistant

and

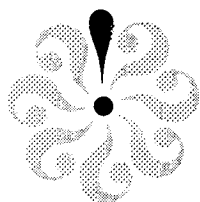
Surendra N. Tiwari, Principal Investigator

Final Report  
For the period ended July 31, 1994

Prepared for  
National Aeronautics and Space Administration  
Langley Research Center  
Hampton, VA 23681-0001

Under  
**Research Grant NAG-1-423**  
Dr. Ajay Kumar, Technical Monitor  
FLDMD-Theoretical Flow Physics Branch

Submitted by the  
**Old Dominion University Research Foundation**  
**P.O. Box 6369**  
**Norfolk, VA 23508**



October 1994

**APPENDIX A: PROGRAM LISTING FOR MONTE CARLO SIMULATION . 132**

**APPENDIX B: PROGRAM LISTING FOR RADIATIVE INTERACTIONS IN**

**LAMINAR FLOWS USING MONTE CARLO SIMULATION . . . . . 151**

## NOMENCLATURE

### Latin Symbols

A	reaction rate constant; also area, $m^2$
C	concentration, $kg.mole/m^3$
$C_p$	specific heat, $J/(kg.K)$
D	diffusion coefficient, $m^2/s$
E	total internal energy, $J/kg$ ; also activation energy, $J/kg$
f	mass fraction
g	Gibbs energy, $J/(kg.K)$
h	static enthalpy, $J/kg$
$h^R$	base enthalpy, $J/kg$
$I_\omega$	spectral radiative intensity, $kW/(m^2.sr.cm^{-1})$
k	thermal conductivity, $J/(m.s.k)$ ; also line intensity to spacing ratio, $cm^{-1}. atm^{-1}$
$k_b$	backward rate constant
$k_{eq}$	equilibrium constant
$k_f$	forward rate constant
L	nozzle length, m
$L_m$	mean beam length, m.
$m_\omega$	total number of narrow bands
M	molecular weight
N	temperature coefficient in reaction rate expression
$N_s$	number of species
$N_r$	number of reactions
p	gas pressure, atm
$q_{cw}$	conductive wall flux, $kW/m^2$
$-\nabla.q_r$	radiative source term, $kW/m^3$

$q_{rw}$	net radiative wall flux, kW/m <sup>2</sup>
$Q$	radiative energy per unit volume, kW/m <sup>3</sup>
$R$	gas constant, J/(kg.K); also random number
$R_u$	universal gas constant, J/(kg.K)
$s, s', s''$	position variables, m
$t$	time, s
$T$	absolute temperature, K
$u$	velocity in x direction, m/s
$u_m$	mean velocity, m/s
$\tilde{u}$	diffusion velocity in x direction, m/s
$v$	velocity in y direction, m/s
$\tilde{v}$	diffusion velocity in y direction, m/s
$\tilde{V}$	diffusion velocity vector, m/s
$\dot{w}$	production rate of species, kg/(m <sup>3</sup> .s)
$x$	x-coordinate, m
$X$	mole fraction
$y$	y-coordinate, m
$y_b$	half height of cross sectional area of nozzle, m
Greek symbols	
$\beta$	line width to spacing ratio
$\gamma$	stoichiometric coefficient; also half-width of an absorption line, cm <sup>-1</sup>
$\delta$	equivalent line spacing, cm <sup>-1</sup>
$\theta$	polar angle
$\mu$	dynamic viscosity, kg/(m.s)
$\kappa_p$	Planck mean absorption coefficient
$\kappa_\omega$	spectral absorption coefficient
$\xi, \eta$	computational coordinates
$\rho$	density, kg/m <sup>3</sup>
$\sigma$	normal stress, N/m <sup>2</sup>
$\tau$	shear stress, N/m <sup>2</sup>
$\tau_\omega$	spectral transmittance
$\phi$	equivalence ratio

$\psi$	azimuthal angle
$\omega$	wavenumber, $\text{cm}^{-1}$
$\Omega$	solid angle

## LIST OF TABLES

Table	Page
3.1 Relation between confidence coefficient $\chi_\alpha$ and confidence probability $1-\alpha$	24
3.2 Comparison of net radiative wall heat fluxes with nonreflecting walls (kW/m <sup>2</sup> )	32
3.3 Comparison of net radiative wall heat fluxes with reflecting walls (kW/m <sup>2</sup> )	39
5.1 CPU time (minutes) required for different solutions	70
6.1 Hydrogen-Air Combustion Mechanism (7 species, 7 reactions)	87

## LIST OF FIGURES

Figure	Page
3.1 Planar medium between two parallel walls. . . . .	13
3.2 Temperature and concentration profiles. . . . .	25
3.3 Comparison of radiative source term for the uniform temperature profile with L=0.1 m. . . . .	27
3.4 Comparison of radiative source term for the uniform temperature profile with L=1.0 m. . . . .	28
3.5 Comparison of radiative source term for the boundary layer type temperature profile. . . . .	29
3.6 Comparison of radiative source term for the parabolic H <sub>2</sub> O concentration profile. . . . .	30
3.7 Comparison of radiative source term in pure H <sub>2</sub> O for $\rho=0.1$ , L=0.5 m. . . . .	33
3.8 Comparison of radiative source term in pure H <sub>2</sub> O for $\rho=0.5$ , L=0.5 m. . . . .	34
3.9 Comparison of radiative source term in pure H <sub>2</sub> O for $\rho=0.9$ , L=0.5 m. . . . .	35
3.10 Comparison of radiative source term in pure H <sub>2</sub> O for $\rho=0.9$ , L=0.1 m. . . . .	36
3.11 Comparison of radiative source term in pure H <sub>2</sub> O for $\rho=0.9$ , L=1.0 m. . . . .	37
3.12 Comparison of correlated and noncorrelated results in pure H <sub>2</sub> O for $\rho=0.0$ , L=0.1 m. . . . .	40
3.13 Comparison of correlated and noncorrelated results in pure H <sub>2</sub> O for $\rho=0.5$ , L=0.1 m. . . . .	41
4.1 Laminar flow between parallel plates with constant wall heat flux. . . . .	44
4.2 Comparison of gray solutions for CO <sub>2</sub> at p=1 atm. . . . .	50
4.3 Comparison of gray solutions for CO <sub>2</sub> at T <sub>w</sub> =1000 K. . . . .	51

4.4	Comparison of gray solutions for $H_2O$ at $p=1$ atm. . . . .	52
4.5	Comparison of gray solutions for $H_2O$ at $T_w=1000$ K. . . . .	53
4.6	Comparison of nongray solutions for $CO_2$ at $p=1$ atm. . . . .	54
4.7	Comparison of nongray solutions for $CO_2$ at $T_w=1000$ K. . . . .	55
4.8	Comparison of nongray solutions for $H_2O$ at $p=1$ atm. . . . .	56
4.9	Comparison of nongray solutions for $H_2O$ at $T_w=1000$ K. . . . .	57
5.1	Schematic of two finite parallel plates and grid configuration. . . . .	60
5.2	Schematic of a rectangular finite volume element ABCD . . . . .	62
5.3	Radiative source distribution at the location $x/L=0.225$ for isothermal and homogeneous $H_2O-N_2$ mixture. . . . .	72
5.4	Radiative source distribution at the location $x/L=0.5$ for isothermal and homogeneous $H_2O-N_2$ mixture. . . . .	73
5.5	Radiative wall flux distribution for isothermal and homogeneous $H_2O-N_2$ mixture. . . . .	74
5.6	Radiative source distribution at the location $x/L=0.275$ for nonisothermal and inhomogeneous $H_2O-O_2-N_2$ mixture. . . . .	75
5.7	Radiative source distribution at the location $x/L=0.5$ for nonisothermal and inhomogeneous $H_2O-O_2-N_2$ mixture. . . . .	76
5.8	Radiative source distribution at the location $x/L=0.825$ for nonisothermal and inhomogeneous $H_2O-O_2-N_2$ mixture. . . . .	77
5.9	Radiative wall flux distribution for nonisothermal and inhomogeneous $H_2O-O_2-N_2$ mixture. . . . .	78
6.1	Schematic diagram of nozzle. . . . .	82
6.2	Grid mesh for flowfield simulation. . . . .	92
6.3	Grid mesh for radiation simulation. . . . .	93
6.4	Physical model for validation calculation. . . . .	100
6.5	Comparison of frozen temperatures along the centerline. . . . .	101



6.6	Comparison of reacting temperatures along the centerline. . . . .	102
6.7	Temperature contours in the nozzle. . . . .	105
6.8	Pressure contours in the nozzle. . . . .	106
6.9	Density contours in the nozzle. . . . .	107
6.10	Velocity vectors in the nozzle. . . . .	108
6.11	H <sub>2</sub> O mass fraction contours in the nozzle. . . . .	109
6.12	OH mass fraction contours in the nozzle. . . . .	110
6.13	H <sub>2</sub> mass fraction contours in the nozzle. . . . .	111
6.14	O <sub>2</sub> mass fraction contours in the nozzle. . . . .	112
6.15	Radiative source distribution at three locations. . . . .	114
6.16	Comparison of radiative and conductive wall fluxes for three different equivalence ratios. . . . .	115
6.17	Comparison of radiative and conductive wall fluxes for three different wall temperatures. . . . .	117
6.18	Comparison of radiative and conductive wall fluxes for three different inlet temperatures. . . . .	118
6.19	Comparison of radiative and conductive wall fluxes for three different nozzle sizes. . . . .	120



## Chapter 1

### INTRODUCTION

Extensive research is underway at the NASA Langley Research Center to develop hydrogen-fueled supersonic combustion ramjet (scramjet) propulsion systems for National Aero-Space Plane (NASP). A critical element in the design of scramjets is the detailed understanding of the complex flowfield present in the different regions of the engine over a wide range of operating conditions. Numerical modeling of the flow in various sections has proven to be a valuable tool for gaining insight into the nature of these flows [1-4].

In a hypersonic propulsion system, combustion takes place at supersonic speeds to reduce deceleration energy losses. The products of hydrogen-air combustion are gases such as water vapor and hydroxyl radicals. These species are highly radiatively absorbing and emitting gases. Thus, numerical simulations must handle correctly radiation phenomena associated with supersonic flows.

Over the past 30 years the analysis of radiative heat transfer has received increasing attention. This was first due to the advent of the space age, which made it necessary to develop tools to predict heat transfer rates in such high-temperature applications as rocket nozzles and space vehicle reentry, and in vacuum applications for spacecraft in outer space. Following a lull during the 1970s and early 1980s, interest in radiative heat transfer has recently increased again because of the need to predict and measure heat transfer rates in ever higher temperature applications in furnaces, and MHD generators, as well as the scramjet mentioned earlier [5-7].

Among the three modes of heat transfer, radiative heat transfer is quite different from conductive and convective heat transfer. Under normal conditions, conduction and convection are short-range phenomena. Thus we are able to perform an energy balance

in an infinitesimal volume. The principle of conservation of energy then leads to a partial differential equation. This equation may have up to four independent variables (three space coordinates and time). Thermal radiation, on the other hand, is generally a long-range phenomena [6-8]. Thus, conservation of energy cannot be applied over an infinitesimal volume, but must be applied over the entire volume under consideration. This leads to an integral equation involving up to seven independent variables (the frequency of radiation, three space coordinates, two coordinates describing the direction of travel of photons, and time).

The analysis of thermal radiation is complicated further by the behavior of the radiative properties of materials. Properties relevant to conduction and convection are fairly easily measured and are generally well behaved. But radiative properties are usually difficult to measure and often display erratic behavior. For liquids and solids, the properties normally depend only on a very thin surface layer, which may vary strongly with surface preparation and often change from day to day. All radiative properties (in particular for gases) may vary strongly with wavenumber, adding another dimension to the governing equation. Rarely, if ever, can this equation be assumed to be linear.

Because of these difficulties inherent in the analysis of thermal radiation, accurate prediction of radiation in most realistic systems is currently still out of the question, although tremendous efforts have been made and significant progress has been achieved in the past decades. Prior to the 1970s, radiative transfer analyses were limited to one-dimensional formulations. Even for one-dimensional cases, nongray radiative heat transfer formulations were very complicated and their solutions required enormous amount of computational resources. Important works in nongray one-dimensional formulation have been reviewed in Refs. 5, 8-10. Since the 1970s, efforts have been directed toward formulating multi-dimensional equations for radiative transfer. Great achievements have been made for gray gaseous systems. However, studies on multi-dimensional nongray gaseous systems encounter tremendous difficulties and little progress has been made so

far. A survey of various methods for multi-dimensional radiative transfer analysis has been made by Howell [11, 12]. Discussions were made regarding the feasibility of incorporating spectral integration in the techniques using narrow band [13] and wide band models [14, 15]. Another review [16] has provided details of several methods that could possibly be applied to multi-dimensional radiative transfer in molecular participating media. Different review articles have indicated unanimously that one of the most promising methods to investigate nongray participating media in multi-dimensional systems is the Monte Carlo method (MCM).

The MCM is a statistical sampling technique which can simulate exactly all important physical processes. In this method, the numerical treatment of the mathematical formulation is easy and the usual difficulties encountered in complex geometries can be circumvented easily. It is because of these advantages that the MCM has been applied to solve many radiative transfer problems. The earliest application of this method for radiative transfer problems was made by Howell and Perlmutter [17]. Radiative problems of increasing complexity which have been investigated by this method have appeared in the literature [18–22]. Studies on reducing the computational time by using this method are also available [23, 24]. The gray gas assumption, however, is made in most of these analyses.

Like other numerical methods, the MCM also has some disadvantages. One of them is the large appetite for computer time, and another is the statistical fluctuation of the results. With the rapid development of computers, these two disadvantages are becoming of less concern and interest in the MCM is increasing. One of the recent applications of the MCM has been in the investigation of radiative interactions in nongray participating media using a narrow band model. For example, Taniguchi et al. [25] applied a simplified form of the Elsasser narrow band model to investigate the problem of radiative equilibrium in a parallel plate system. Farmer and Howell [26] obtained a Monte Carlo solution of radiative heat transfer in a three-dimensional enclosure with an anisotropically scattering,

spectrally dependent, inhomogeneous medium. Modest [27] discussed the effects of narrow band averaging on surface and media emissions. It was pointed out that the narrow band model may be applied successfully to the MCM after verification in an isothermal and homogeneous medium. However, all these studies have failed to reflect some fundamental mechanisms of the MCM in conjunction with a narrow band model, and the application of the MCM to nongray radiation problems is still uncertain.

The first objective of this study is to employ a general and accurate narrow band model to investigate radiative heat transfer using the MCM. The same nongray model has been applied to investigate radiation contributions using the discrete direction method [28] and the *S-N discrete ordinates method* [29]. The present investigation includes derivation of the Monte Carlo statistical relationships, discussion of the fundamental features that are different from other methods and demonstration of the capability of the MCM for nongray analyses. A one-dimensional problem is considered first, and the validation of the Monte Carlo analysis is conducted by comparing the Monte Carlo results with available solutions for the cases with and without other modes of heat transfer. Next, the Monte Carlo formulations suitable for multi-dimensional problems are developed and validated. From our knowledge, the present study is the first to provide accurate and general radiative transfer formulations which are applicable for any nongray and multi-dimensional system.

A literature survey indicates that a great deal of effort has been made towards an accurate formulation of radiative transfer equations. Most applications of these formulations have been restricted to non-reacting homogeneous systems. Only a limited number of studies are available to investigate the interaction of radiation heat transfer in chemically reacting, viscous, compressible flows such as those in scramjet propulsion systems. Mani and Tiwari [30] were the first to take into account the effect of radiation on chemically reacting supersonic flows. This work has been extended to include some relatively more advanced chemistry models by Tiwari et al. [31]. In both of these studies,

a tangent slab approximation for radiative transfer was employed. This approximation treats the gas layer as a one-dimensional slab in evaluation of radiative flux. Obviously, it is impossible to obtain reliable quantitative predictions of radiative heat transfer from this treatment. Therefore, the second objective of this study is to apply the Monte Carlo formulations developed during the course of present research efforts to investigate the radiative interaction in multi-dimensional chemically reacting flows. The specific problem considered is the supersonic flow of premixed hydrogen and air in an expanding two-dimensional nozzle. Two-dimensional radiative heat transfer in this problem is simulated using the MCM; the results of radiative flux are then incorporated in the two-dimensional Navier-Stokes equations. This procedure provides a more accurate prediction of radiative effects on flowfield and wall heat transfer than those available in previous studies. The physics of radiative interactions in chemically reacting compressible flows can be understood more clearly from this study.

Two different objectives divide the present study into two parts. The first part is to develop and validate the Monte Carlo formulations with a narrow band model. This work is included in Chaps. 2-5. Information on radiation absorption models is given in Chap. 2. Development and validation of the Monte Carlo formulations for one-dimensional problem is provided in Chap. 3. Further validation for the one-dimensional formulations is conducted in Chap. 4 by considering a simple problem of radiative interactions. Development and validation of Monte Carlo formulations for radiative transfer in multi-dimensional systems is presented in Chap. 5. The second part of the study is an investigation of radiative interactions in chemically reacting flows. This work is included in Chap. 6. Finally, the conclusions reached from this study are summarized in Chap. 7.





## Chapter 2

### RADIATION ABSORPTION MODELS

The study of radiative transmission in nonisothermal and inhomogeneous gaseous systems requires a detailed knowledge of the absorption, emission and scattering characteristics of the specific species under investigation. In absorbing and emitting media, an accurate model for the spectral absorption coefficient is of vital importance in the correct formulation of the radiative flux equations. A systematic representation of the absorption by a gas, in the infrared part of spectrum, requires the identification of the major infrared bands and the evaluation of the line parameters (line intensity, line half-width, and spacing between the lines) of these bands. The line parameters depend upon the temperature, pressure and concentration of the absorbing molecules and, in general, these quantities vary continuously along a nonisothermal and inhomogeneous path in the medium. In recent years, considerable efforts have been expended in obtaining the line parameters and absorption coefficients of important atomic and molecular species [32–34].

For an accurate evaluation of the transmittance ( or absorptance) of a molecular band, a convenient line model is used to represent the variation of the spectral absorption coefficient. The line models usually employed are Lorentz, Doppler, and Voight line profiles. A complete formulation ( and comparison) of the transmittance and absorption by these line profiles has been given [9, 10, 35–37]. In a particular band consisting of many lines, the absorption coefficient varies rapidly with frequency. Thus, it becomes a very difficult and time-consuming task to evaluate the total band absorption over the actual band contour, by employing an appropriate line profile model. Consequently, several approximate band models (narrow as well as wide) have been proposed which represent absorption from an actual band with reasonable accuracy [9, 10, 35–46]. Several

continuous correlations for total band absorption are available in the literature [9, 10, 35–37, 43–46]. These have been employed in many radiative transfer analyses with varying degree of success [9, 10, 35–37, 47]. A brief discussion is presented here on narrow band models, wide band models, and band absorptance correlations.

The absorption within a narrow spectral interval of a vibration-rotation band can be represented quite accurately by the so-called “narrow band models.” The most commonly employed narrow band models are the Elsasser, statistical, random-Elsasser and quasi-random narrow band models. Various narrow band models have been tested with the results of line-by-line calculations in the literature [37, 48, 49]. Accurate results for temperature and heat flux distributions were obtained with the statistical narrow band model, which assumes the absorption lines to be placed randomly and the intensities to obey an exponential-tailed-inverse distribution. The transmittance predicted by this model in a homogeneous and isothermal column of length  $l$  due to gas species  $j$ , averaged over  $[\omega - (\Delta\omega/2), \omega + (\Delta\omega/2)]$ , is expressed as [50]

$$\bar{\tau}_{\omega}^j = \exp \left[ -\frac{\bar{\beta}}{\pi} \left( \sqrt{1 + \frac{2\pi X_j p l \bar{k}}{\bar{\beta}}} - 1 \right) \right] \quad (2.1)$$

where  $X_j$  represents the mole fraction of the absorbing species  $j$  and  $p$  is total pressure;  $\bar{k}$  and  $\bar{\beta} = 2\pi\bar{\gamma}/\bar{\delta}$  are the band model parameters which account for the spectral structure of the gas. The overbar symbol indicates that the quantity is averaged over a finite wavenumber interval  $\Delta\omega$ . The narrow band width considered is usually  $25 \text{ cm}^{-1}$ . Parameters  $\bar{k}$  and  $1/\bar{\delta}$  generated from a line-by-line calculation have been published for  $\text{H}_2\text{O}$ ,  $\text{CO}_2$ ,  $\text{CO}$ ,  $\text{OH}$ ,  $\text{NO}$ , and other species [33, 48, 51]. The mean half-widths  $\bar{\gamma}$  for  $\text{H}_2\text{O}$  and  $\text{CO}_2$  are obtained by Soufiani et al. as [48]

$$\begin{aligned} \bar{\gamma}_{\text{H}_2\text{O}} = 0.066 \frac{p}{p_s} & \left\{ 7.0 X_{\text{H}_2\text{O}} \frac{T_s}{T} + [1.2(X_{\text{H}_2\text{O}} + X_{\text{N}_2}) \right. \\ & \left. + 0.8 X_{\text{O}_2} + 1.6 X_{\text{CO}_2}] \sqrt{\left( \frac{T_s}{T} \right)} \right\} \end{aligned} \quad (2.2)$$

and

$$\bar{\gamma}_{CO_2} = \frac{p}{p_s} \left( \frac{T_s}{T} \right)^{0.7} [0.07X_{CO_2} + 0.058(X_{N_2} + X_{O_2}) + 0.15X_{H_2O}] \quad (2.3)$$

where  $p_s$  and  $T_s$  designate standard pressure and temperature (1 atm, 296 K). Alternative formulations for evaluating the mean half-width  $\bar{\gamma}$  are also available in Ref. 33.

The absorption within the spectral range of the entire vibration-rotation band can be represented by the so-called "wide band models." The total band absorption of the wide band models is given by

$$A = \int_{-\infty}^{\infty} [1 - \exp(-\kappa_{\omega} l)] d(\omega - \omega_0) \quad (2.4)$$

where the limits of integration are over the entire band pass,  $\kappa_{\omega}$  is the spectral absorption coefficient, and  $\omega_0$  is the wave number at the center of the wide band.

Four commonly used wide band models are the box, modified box, exponential and axial wide band models. The exponential wide band model, first developed by Edwards and Menard [41], is by far the most successful of the wide band models. In this model, the line intensity is assumed to be an exponential decaying function of the wave number [9, 10, 35–37, 44–46], such that

$$\frac{S_j}{d} = \frac{S}{A_0} e^{-b_0 |\omega - \omega_0| / A_0} \quad (2.5)$$

where  $S$  is the band intensity,  $A_0$  the band width parameter and  $b_0=2$  for a symmetrical band or  $b_0=1$  for bands with upper and lower wave number heads at  $\omega_0$ .

The radiative flux term usually involves multiple integrals even for simple geometries. As a result, numerical calculation of radiative flux for energy transfer becomes very time consuming. Therefore it is desirable to replace the relation for the total band absorptance, given by Eq. (2.4), with a continuous correlation [5, 10, 52]. Numerous correlations are available in the literature for wide band absorptance. The first correlation to satisfy the linear, square-root, and logarithmic limits of the wide band absorptance was proposed by Edwards and Menard [41]. The most widely used correlation is the Tien and Lowder

continuous correlation because of its simplicity and relative accuracy. This correlation is expressed as [52]

$$A = A_0 \ln \left[ u f(t) \frac{(u+2)}{(u+2f(t))} + 1 \right] \quad (2.6)$$

where

$$f(t) = 2.94[1 - \exp(-2.6t)], \quad t = \frac{\beta^*}{2} \quad (2.7)$$

Here  $u = \text{Spl}/A_0$  is nondimensional path length and  $\beta^*$  is line structure parameter. Wide band model correlation parameters for various gases are available in the literature [6, 7, 10, 35].

Among the approximate band models discussed above, the wide band models and band absorptance correlations are simpler than the narrow band models, and they have been used extensively in the study of nongray radiative heat transfer for the past three decades. However, the spectral discretization used in the wide band models and band absorptance correlations is too wide and it does not take into account the low resolution correlations between intensities and transmissivities. This leads to significant temperature and heat flux discrepancies [49]. Also, the case of partially reflecting walls cannot be modelled correctly with these models [10]. Recently, the narrow band models have begun to receive attention due to the rapid development of computers and strong requirements for accurate analyses of radiation [25–29]. Some narrow band models compare favorably to the line-by-line calculations; However, they are much simpler than the line-by-line models. In addition, use of the narrow band models can avoid some notorious disadvantages occurring with the wide band models and band absorptance correlations. In this study, the narrow band model expressed in Eq. (2.1) is employed to investigate nongray radiative heat transfer.

For a nonisothermal and inhomogeneous column, the Curtis-Godson approximation [53] leads to accurate results if pressure gradients are not too large. Basically, this approach consists of transformation of such a column into an equivalent isothermal and

homogeneous one. For the narrow band model expressed in Eq. (2.1), effective band model parameters  $\bar{k}_e$  and  $\bar{\beta}_e$  are introduced by averaging  $\bar{k}$  and  $\bar{\beta}$  over the optical path  $U$  of the column as

$$U(l) = \int_0^l p(y) X_j(y) dy \quad (2.8)$$

$$\bar{k}_e = \frac{1}{U(l)} \int_0^l p(y) X_j(y) \bar{k}(y) dy \quad (2.9)$$

$$\bar{\beta}_e = \frac{1}{\bar{k}_e U(l)} \int_0^l p(y) X_j(y) \bar{k}(y) \bar{\beta}(y) dy \quad (2.10)$$

The transmittance of this equivalent column is then calculated from Eq. (2.1).

A distinguishing characteristic for the band models discussed above is the dependence of the wavenumber. If it is assumed that the absorption coefficient is independent of the wavenumber, the radiation absorption is then represented by the so-called “gray model”. The gray model is rarely a physically realistic approximation, but it serves as an initial step for studying the effect of radiative heat transfer. For a nonuniform temperature field, the gray model used for optically thin radiation is the modified Planck mean absorption coefficient which, for black bounding surfaces, is defined as [8, 35]

$$\kappa_m(T, T_w) = \kappa_p(T_w)(T_w/T) \quad (2.11)$$

where  $\kappa_p(T)$  represents the Planck mean absorption coefficient. For a multiband system of a homogeneous gas,  $\kappa_p(T)$  is expressed as

$$\kappa_p(T) = p \sum_{i=1}^n [e_b(\omega_i, T) S_i(T)] / (\sigma T^4) \quad (2.12)$$

where  $n$  represents the number of vibration-rotation bands,  $e_b(\omega_i, T)$  is the Planck function evaluated at the  $i$ th band center,  $S_i(T)$  is the integrated band intensity of the  $i$ th band, and  $\sigma$  is the Stefan-Boltzmann constant. Equation (2.12) is modified to apply to a mixture

of different gases as

$$\kappa_p(T) = \sum_j p_j \left\{ \sum_{i=1}^n [e_b(\omega_i, T) S_i(T)] \right\}_j / (\sigma T^4) \quad (2.13)$$

where  $j$  denotes the number of species in the mixture and  $p_j$  is the partial pressure of  $j$ th species. The band model parameters for various gases are available in the literature [6, 7, 10, 35].

## Chapter 3

### MONTE CARLO SIMULATION USING A NARROW BAND MODEL

In this chapter, the radiative heat transfer for a one-dimensional problem is investigated using a narrow band model and Monte Carlo simulation. The physical model is established in Sec. 3.1. Monte Carlo formulations are developed in Sec. 3.2. Discussion of special features of the method for nongray analyses is made in Sec. 3.3. Estimation of statistical error is presented in Sec. 3.4 and validation of Monte Carlo formulation is conducted in Sec. 3.5.

#### 3.1 Physical Model

To investigate radiative heat transfer using the MCM and a narrow band model, a simple problem is considered at first. Figure 3.1 shows an absorbing and emitting molecular gas between two infinite parallel plates with slab thickness of  $L$ . Temperature, concentration and pressure in the medium are assumed known. The walls are assumed to be diffuse but not necessarily gray. The wall temperature is also assumed known. Usually, the radiative transfer quantities of interest are the radiative source term  $-\nabla \cdot q_r$  inside the medium and the net radiative wall flux  $q_{rw}$ . In order to calculate these quantities, the medium considered is divided into  $(M-2)$  volume elements. The grid 1 and  $M$  are numbered on the lower and upper walls, respectively. Temperature, concentration and pressure are assumed to be constant in each volume element. The typical method for handling radiative exchange between surface and/or volume elements is to evaluate the multiple integral, which describes the exchange, by some type of numerical integration technique. This usually is a good approach for simple problems, but an alternate method is used here. Radiative transfer in the computational domain is simulated using the MCM.

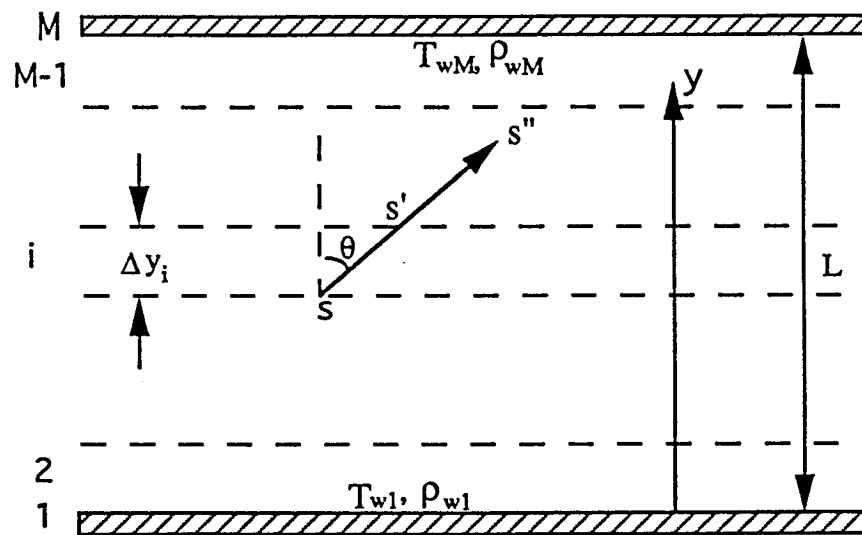


Fig. 3.1 Planar medium between two parallel walls.



For an arbitrarily chosen volume element with a volume,  $\delta V$ , and an arbitrarily chosen surface element with an area  $\delta A$ , the relations for  $-\nabla \cdot q_r$  and  $q_{rw}$  are expressed as

$$-\nabla \cdot q_r = \frac{Q_{V-\delta V} + Q_{A-\delta V} - Q_{\delta V}}{\delta V} \quad (3.1)$$

$$q_{rw} = \frac{Q_{V-\delta A} + Q_{A-\delta A} - Q_{\delta A}}{\delta A} \quad (3.2)$$

Here,  $Q_{V-\delta V}$  and  $Q_{V-\delta A}$  are the total radiant energy from the entire gas that is absorbed by the volume element  $\delta V$  and surface element  $\delta A$ , respectively;  $Q_{A-\delta V}$  and  $Q_{A-\delta A}$  are the total radiant energy from the bounding walls that is absorbed by  $\delta V$  and  $\delta A$ , respectively;  $Q_{\delta V}$  and  $Q_{\delta A}$  are the radiant energy emitted by  $\delta V$  and  $\delta A$ , respectively.

To evaluate the terms  $Q_{V-\delta V}$ ,  $Q_{A-\delta V}$ ,  $Q_{\delta V}$  and  $Q_{V-\delta A}$  in Eqs. (3.1) and (3.2), the MCM uses a large number of bundles of energy (statistical samples) to simulate the actual physical processes of radiant emission and absorption of the energy occurring in the medium. These energy bundles are similar to photons in their behavior. The histories of these energy bundles are traced from their point of emission to their point of absorption. What happens to each of these bundles depends on the emissive, scattering and absorptive behavior within the medium which is described by a set of statistical relationships. The total number of energy bundles absorbed by each element multiplied by the energy per bundle gives the interchange of radiation among the volume and /or surface elements. The values of  $-\nabla \cdot q_r$  and  $q_{rw}$  can then be obtained from Eqs. (3.1) and (3.2), respectively.

The use of a narrow band model in the MCM presents new features in the analysis of radiative heat transfer. The statistical relationships currently in use need to be modified. The following Monte Carlo analysis is based on an arbitrarily chosen finite volume element. The statistical relationships for an energy bundle emitted from a surface element can be derived by following the same procedure.

### 3.2 Monte Carlo Formulations

Let us consider the Planck spectral blackbody intensity  $I_{b\omega}$  that enters the  $i$ th volume element at the point  $s$  on the lower side and intersects the upper side at the point  $s'$  as shown in Fig. 3.1. A spherical coordinate system is established and centered at the point  $s$ . From Ref. 6, the amount of energy emitted for a wavenumber range  $d\omega$  and along a pencil of column  $s \rightarrow s'$  with a solid angle increment  $d\Omega$  is expressed as

$$dQ_i = I_{b\omega} [1 - \tau_\omega(s \rightarrow s')] \cos \theta d\Omega d\omega \quad (3.3)$$

where  $\tau_\omega(s \rightarrow s')$  is the spectral transmittance over the path  $s \rightarrow s'$ ,  $\theta$  is the polar angle between the  $y$  axis and the direction of the column  $s \rightarrow s'$ , and  $d\Omega = \sin \theta d\theta d\psi$  where  $\psi$  is the azimuthal angle. The total emitted energy per unit volume is obtained by integrating Eq. (3.3) over all wavenumbers, and polar and azimuthal angles as [6, 54, 55]

$$\begin{aligned} Q_i &= \int_0^\infty \int_0^\pi \int_0^{2\pi} I_{b\omega} [1 - \tau_\omega(s \rightarrow s')] \cos \theta \sin \theta d\psi d\theta d\omega \\ &= 2\pi \int_0^\infty \int_0^\pi I_{b\omega} [1 - \tau_\omega(s \rightarrow s')] \cos \theta \sin \theta d\theta d\omega \\ &= 2\pi \int_0^\infty \int_{-1}^1 I_{b\omega} [1 - \tau_\omega(\Delta y_i / \mu)] \mu d\mu d\omega; \quad \mu = \cos \theta \end{aligned} \quad (3.4)$$

where  $\Delta y_i$  is the thickness of  $i$ th volume element. It should be noted that the sign of  $\Delta y_i$  is different when  $\mu$  varies from positive to negative.

The simulation of an energy bundle includes the determination of wavenumber and direction of emission of this energy bundle in the finite volume element. The statistical relationships for determining these parameters are readily obtained from Eq. (3.4) as

$$R_\omega = \frac{2\pi \int_0^\infty \int_{-1}^1 I_{b\omega} [1 - \tau_\omega(\Delta y_i / \mu)] \mu d\mu d\omega}{Q_i} \quad (3.5)$$

$$R_\mu = \frac{2\pi \int_{-1}^1 \int_0^\infty I_{b\omega} [1 - \tau_\omega(\Delta y_i / \mu)] \mu d\omega d\mu}{Q_i} \quad (3.6)$$

where  $R_\omega$  and  $R_\mu$  are random numbers which are distributed uniformly between zero and one. In Eqs. (3.4)-(3.6),  $\tau_\omega$  is a real spectral transmittance. Before solving these equations to obtain  $\omega$  and  $\mu$  from a set of given values of  $R_\omega$  and  $R_\mu$ , the narrow band model should be applied to approximate the real spectral transmittance.

For the narrow band model, the absorption bands of the gas are divided into spectral ranges  $\Delta\omega$  wide; each is centered at  $\omega^k$  and characterized by the superscript  $k$ ; the band parameters obtained are the averaged quantities over a narrow band. So, the spectral quantities in Eqs. (3.4)-(3.6) should be transformed into the averaged quantities over a narrow band for practical applications. Taking the spectral average over all narrow bands, Eqs. (3.4)-(3.6) are expressed as

$$Q_i = 2\pi \sum_{k=1}^{m_\omega} \left\{ \int_{-1}^1 \overline{I_{b\omega^k}} [1 - \overline{\tau_{\omega^k}}(\Delta y_i/\mu)] \mu d\mu \right\} \Delta\omega^k \quad (3.7)$$

$$R_\omega = \frac{2\pi \sum_{k=1}^n \left\{ \int_{-1}^1 \overline{I_{b\omega^k}} [1 - \overline{\tau_{\omega^k}}(\Delta y_i/\mu)] \mu d\mu \right\} \Delta\omega^k}{Q_i}, \quad (\omega^{n-1} < \omega \leq \omega^n) \quad (3.8)$$

$$R_\mu = \frac{2\pi \sum_{k=1}^{m_\omega} \left\{ \int_{\mu}^1 \overline{I_{b\omega^k}} [1 - \overline{\tau_{\omega^k}}(\Delta y_i/\mu)] \mu d\mu \right\} \Delta\omega^k}{Q_i} \quad (3.9)$$

where  $m_\omega$  is the total number of narrow bands. The following narrow band approximation has been used in obtaining Eqs. (3.7)-(3.9)

$$\begin{aligned} \overline{I_{b\omega^k} \tau_{\omega^k}} &= \frac{1}{\Delta\omega^k} \int_{\Delta\omega^k} I_{b\omega} \tau_{\omega} d\omega \\ &\approx \overline{I_{b\omega^k}} \left( \frac{1}{\Delta\omega^k} \int_{\Delta\omega^k} \tau_{\omega} d\omega \right) \\ &= \overline{I_{b\omega^k}} \overline{\tau_{\omega^k}} \end{aligned} \quad (3.10)$$

This is because  $I_{b\omega}$  is essentially constant over a narrow band and may be taken out of the spectral integral. Otherwise, the average product  $\overline{I_{b\omega^k} \tau_{\omega^k}}$  is not equal to the product of  $\overline{I_{b\omega^k}}$  and  $\overline{\tau_{\omega^k}}$ .

Equations (3.8) and (3.9) are solved for  $\omega$  and  $\mu$  each time a set of values of  $R_\omega$  and  $R_\mu$  are chosen. The computing time becomes too large for practical calculations since the integrands in these equations are very complex functions of integration variables and the number of energy bundles usually is very large. To circumvent this problem, interpolation and approximation methods are employed. For example, to obtain the value of  $\omega$  for a given value of  $R_\omega$ , we first choose different values of  $\omega$  and obtain the corresponding values of  $R_\omega$  from Eq. (3.8). Then, a smooth curve is constructed to match these data points, and  $\omega$  values are obtained easily from this curve for selected values of  $R_\omega$ . The procedures for determining  $\mu$  are similar to those for  $\omega$ .

Following the determination of wavenumber and direction of an energy bundle, it is essential to find the location of absorption of the energy bundle in the participating medium. Let us still consider the emitted radiant energy along a pencil of column  $s \rightarrow s'$  (Fig. 3.1). After this amount of energy is transmitted over a column  $s' \rightarrow s''$ , the remaining radiant energy is given by

$$dQ'_i = I_{b\omega} [1 - \tau_\omega(s \rightarrow s')] \tau_\omega(s' \rightarrow s'') \cos \theta d\Omega d\omega \quad (3.11)$$

where  $\tau_\omega(s' \rightarrow s'')$  is the spectral transmittance over the path  $s' \rightarrow s''$ . Taking a narrow band average over Eqs. (3.3) and (3.11) and dividing the latter one with the first one, the statistical relationship for determining the location of absorption can be expressed as

$$\begin{aligned} R_l &= \frac{[1 - \tau_\omega(s \rightarrow s')] \tau_\omega(s' \rightarrow s'')}{1 - \overline{\tau_\omega(s \rightarrow s')}} \\ &= \frac{\overline{\tau_\omega(s' \rightarrow s'')} - \overline{\tau_\omega(s \rightarrow s')} \overline{\tau_\omega(s' \rightarrow s'')}}{1 - \overline{\tau_\omega(s \rightarrow s')}} \end{aligned} \quad (3.12)$$

where  $R_l$  is a random number. The averaged product  $\overline{\tau_\omega(s \rightarrow s') \tau_\omega(s' \rightarrow s'')}$  is not equal to the product of  $\overline{\tau_\omega(s \rightarrow s')}$  and  $\overline{\tau_\omega(s' \rightarrow s'')}$  because the  $\tau_\omega(s \rightarrow s')$  and  $\tau_\omega(s' \rightarrow s'')$  have a strong wavenumber dependence due to the high resolution structure in a very small range of an absorption band (hundreds of major absorption lines in a  $25 \text{ cm}^{-1}$  spectral interval), and must be treated in a spectrally correlated way. Equation (3.12)

can be simplified as

$$R_l = \frac{\overline{\tau_\omega}(s' \rightarrow s'') - \overline{\tau_\omega}(s \rightarrow s'')}{1 - \overline{\tau_\omega}(s \rightarrow s')} \quad (3.13)$$

If the spectral correlation between  $\tau_\omega(s \rightarrow s')$  and  $\tau_\omega(s' \rightarrow s'')$  is not taken into account, then Eq. (3.12) becomes

$$R_l = \overline{\tau_\omega}(s' \rightarrow s'') \quad (3.14)$$

Equation (3.14) is the statistical relationship usually employed for determining the location of absorption in the Monte Carlo simulation and is quite different from Eq. (3.13). For an isothermal and homogeneous medium, the travelling distance of an energy bundle can be obtained directly by solving Eq. (3.13) for a given random number. But this procedure turns out to be somewhat complicated for a nonisothermal and inhomogeneous medium. It becomes necessary to try each volume element starting from the adjacent element of the location where an energy bundle emits until a finite volume element is found in which Eq. (3.13) can be satisfied.

### 3.3 Special Features of MCM for Nongray Analysis

The MCM is quite different from other numerical techniques for the analysis of radiative heat transfer. Its characteristics have been discussed in detail by Siegel and Howell [6]. Use of a nongray model in the radiative transfer analysis requires significant changes. Two special features of incorporating the nongray model in the MCM will be discussed.

Most of the existing analyses in radiative heat transfer start with the transfer equation of the type given by Siegel and Howell [6]. In order to apply a narrow band model, this equation has to be spectrally averaged over a narrow band. This averaging treatment results in two types of spectral correlations [56]. One is the spectral correlation between the intensity and the transmittance within the medium. Another is the spectral correlation between the reflected component of the wall radiosity and the transmittance. In order

to investigate the first type of spectral correlation, all the intermediate transmittances in each finite volume element of medium along the path the radiative energy travels must be calculated and stored to make a correlated calculation. In order to investigate the second type of spectral correlation, a series expansion of the wall radiosity is required [57, 58]. Essentially, this series expansion is utilized along with a technique for closure of the series.

The simulation of radiative heat transfer in the MCM is not based directly on the radiative transfer equation. This results in the MCM having features different from the other methods for nongray analysis. When radiative energy is transmitted in a medium, the spectral correlation does occur in the MCM, but it occurs between the transmittances of two different segments of the same path which is different from other methods. This is the first noteworthy feature of the MCM for nongray analysis.

The MCM procedures are based on the direct simulation of the path of an energy bundle. For the case with reflecting walls, the mechanism of the reflections simulation in the MCM is the same as a series expansion of the wall radiosity. However, this simulation process becomes much simpler because of its probabilistic treatment. Also, there are no spectrally correlated quantities involved. This is the second distinctive feature of the MCM for nongray analysis. Exact treatment of the reflections in the MCM in nongray gases is the same as that in gray gases and may be found in the literature [6, 54, 55].

The second feature of the MCM allows one to obtain results for a reflecting wall with very little increase in the computation time compared to that for a nonreflecting wall. But in other methods, the consideration of the history of a finite number of reflections and approximating the remaining reflections by a closure method in the radiative transfer equation complicates the mathematical formulation and increases the computer time considerably. As the geometry considered becomes more complicated, exact simulation of the radiative heat transfer in cases with reflecting walls will be very difficult for most existing methods, while it is not a big problem for the MCM. So, it seems that the MCM

is able to retain the feature of simplicity in dealing with complicated problems while a narrow band model is employed.

### 3.4 Estimation of Statistical Error

In the Monte Carlo simulation, the computational error consists of the statistical error and the computer truncation error. The statistical error is the major error source and the truncation error is usually neglected. From probability theory [59–63], the convergent speed of the Monte Carlo solution is proportional to the  $1/\sqrt{N}$  for a statistical process with a sample size of  $N$ . Such a speed is very slow among all kinds of numerical computation methods. In practical applications, sample size cannot be an infinitely large number due to limitations on computer resources. Therefore, the Monte Carlo calculation must be supplemented with an estimate of the statistical error.

To analyze the statistical error, the radiation simulation between two elements is considered first. For the sake of simplicity, the element from which the radiant energy is emitted is represented by  $\delta V_i$  and the element from which the radiant energy is absorbed is represented by  $\delta V_j$ ; it does not matter whether the element considered is a volume element or a surface element.

In the computational domain, the travel state of an energy bundle emitted from  $\delta V_i$  can be described by the spatial position  $\vec{r}$  and moving direction  $\vec{\Omega}$ . Thus, the travel state is expressed as

$$S = (\vec{r}, \vec{\Omega}) \quad (3.15)$$

After travelling the  $i$ -th step, the state becomes

$$S = (\vec{r}_i, \vec{\Omega}_i) \quad (3.16)$$

An energy bundle travels in the medium surrounded by the surfaces and is absorbed by an element  $\delta V_j$  at the  $\tau$ -th step. Such a random travelling process  $X$  can be described

Thus, the statistical simulation error in the radiative term is expressed as

$$\varepsilon = |\varphi_{V-\delta V_j} - Q_{V-\delta V_j}| < \chi_\alpha \cdot \sigma_{V-\delta V_j} \quad (3.29)$$

where  $\chi_\alpha$  is the confidence coefficient and  $\alpha$  is the confidence level. Table 3.1 is the standard normal distribution table which provides the relation between the confidence coefficient  $\chi_\alpha$  and confidence probability  $1-\alpha$ . For example, when  $1-\alpha=0.95$ ,  $\chi_\alpha$  is taken to be 1.96. In practical applications, the relative statistical error is usually employed and it is expressed as

$$\delta = \frac{\varepsilon}{Q_{V-\delta V_j}} < \frac{\chi_\alpha \cdot \sigma_{V-\delta V_j}}{Q_{V-\delta V_j}} = \delta_0 \quad (3.30)$$

where  $\delta_0$  is the maximum relative statistical error.

### 3.5 Results and Discussion

In order to validate the Monte Carlo simulation, along with a narrow band model, results for a radiative source inside the medium and the net radiative wall heat flux have been obtained for different temperature and concentration profiles with nonreflecting and reflecting walls. Appendix A provides the computer code for the Monte Carlo simulation. In the present study, the reflectivities of two parallel diffuse walls are assumed to be identical and are denoted by the symbol  $\rho$ . Three different temperature profiles were used here: uniform, boundary layer type and parabolic profiles (Fig. 3.2). They were obtained from Kim et al. [29] and Menart et al. [56]. For the uniform temperature profile, the gas temperature was chosen to be 1000 K, while the walls were held at 0 K. Also shown in the figure is a parabolic  $H_2O$  concentration profile for a mixture of  $H_2O$  and  $N_2$  at 1 atm, and it was also taken from the above cited references. A uniform composition of pure  $H_2O$  vapor at 1 atm is another  $H_2O$  concentration profile that was used. Several cases with the selected temperature and  $H_2O$  concentration profiles have been considered previously using the S-N discrete ordinates method by including all important bands



Table 3.1 Relation between confidence coefficient  $\chi_\alpha$  and confidence probability  $1-\alpha$ 

$\chi_\alpha$	$1-\alpha$	$\chi_\alpha$	$1-\alpha$	$\chi_\alpha$	$1-\alpha$	$\chi_\alpha$	$1-\alpha$
0.0	0.00000	1.0	0.68269	2.0	0.95450	3.0	0.99730
0.1	0.07966	1.1	0.72867	2.1	0.96427	3.1	0.99806
0.2	0.15852	1.2	0.76986	2.2	0.97219	3.2	0.99863
0.3	0.23582	1.3	0.80640	2.3	0.97855	3.3	0.99904
0.4	0.31084	1.4	0.83849	2.4	0.98360	3.4	0.99933
0.5	0.38292	1.5	0.86639	2.5	0.98758	3.5	0.99953
0.6	0.45149	1.6	0.89040	2.6	0.99068	3.6	0.99968
0.7	0.51607	1.7	0.91087	2.7	0.99307	3.7	0.99978
0.8	0.57629	1.8	0.92814	2.8	0.99489	3.8	0.99986
0.9	0.63188	1.9	0.94257	2.9	0.99627	$\infty$	1.00000

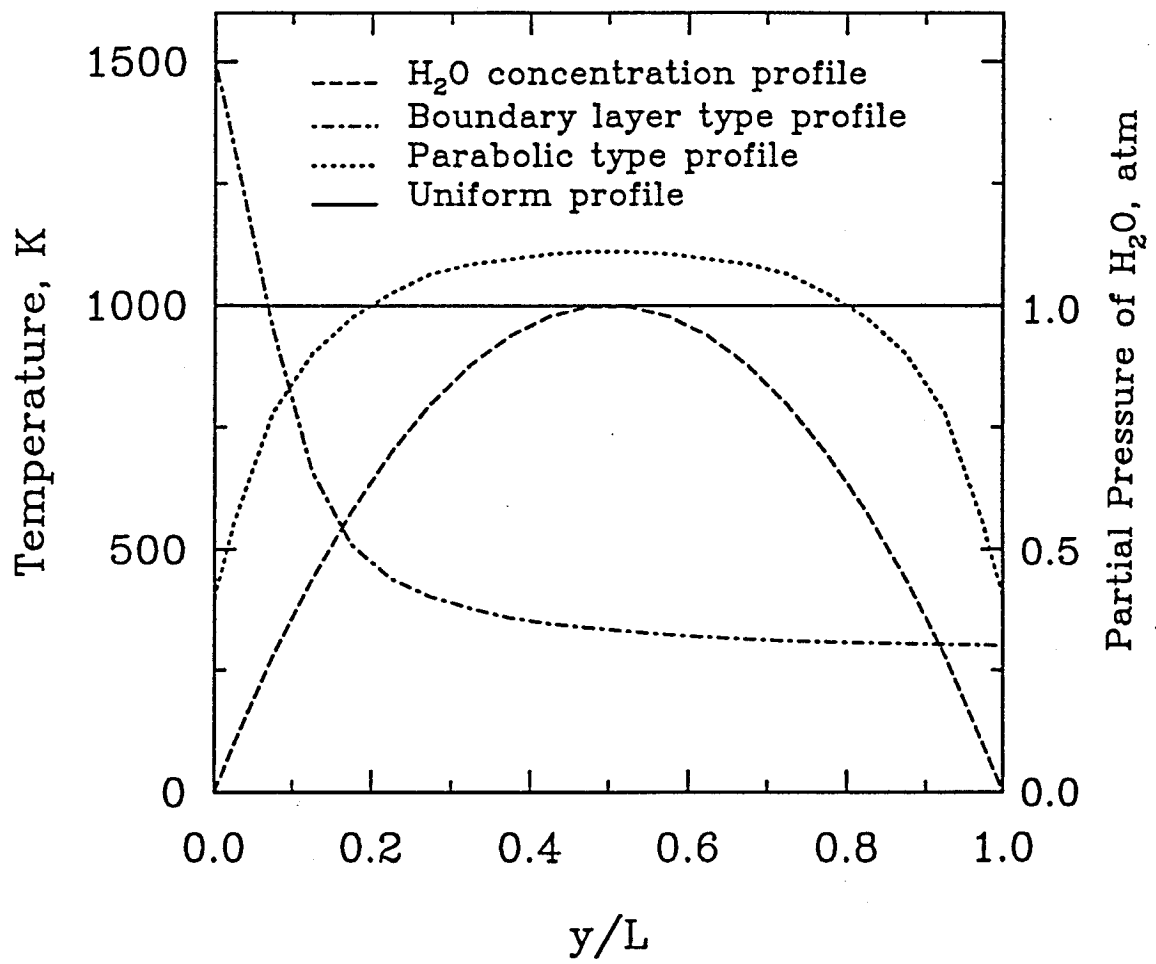


Fig. 3.2 Temperature and concentration profiles.

[29, 56]. The Monte Carlo solutions have been compared with published solutions for identical conditions.

In the Monte Carlo simulation, the entire slab of the physical problem is divided into 20 sublayers for all calculations. Further subdivision of the computational domain was found to yield little change in the results. The computations were performed on a Sun Sparc workstation. The number of total energy bundles for each case was chosen to be 50,000. This choice represents a compromise between accuracy and economy of computation time. When the relative statistical errors of the results were chosen to be less than  $\pm 3\%$ , the probability of the results lying within these limits was greater than 95%. The computing times for the correlated and noncorrelated formulations were essentially the same. For an isothermal and homogeneous medium, the required CPU time was about 1–2 minutes for each case. For a nonisothermal and inhomogeneous medium, the CPU time increased to 5–7 minutes, and was nearly 10 minutes for the case with strongly reflecting walls ( $\rho=0.9$ ) with large optical length ( $L=0.5$  m).

The situation with nonreflecting walls is considered first. Figures 3.3-3.6 show the comparisons between the Monte Carlo solutions and S-N discrete ordinates solutions. Four different S-N discrete ordinates solutions are available in the literature [29] which employ different band models. For our comparison, we selected the solution — S-20 nongray narrow band solution because it employs the same narrow band model as used in this study.

Figures 3.3 and 3.4 show the radiative source results obtained for the uniform temperature and uniform pure H<sub>2</sub>O vapor distributions with slab thicknesses of 0.1 m and 1.0 m, respectively. The Monte Carlo results essentially match the S-N discrete ordinates results. Figure 3.5 presents the results for the boundary layer type temperature profile and for the same concentration distribution as in Figs. 3.3 and 3.4. The Monte Carlo results predict the same changes in gas behavior (from a net emitter near the hot wall to a net absorber away from the hot wall) as the S-N discrete ordinates results. The results

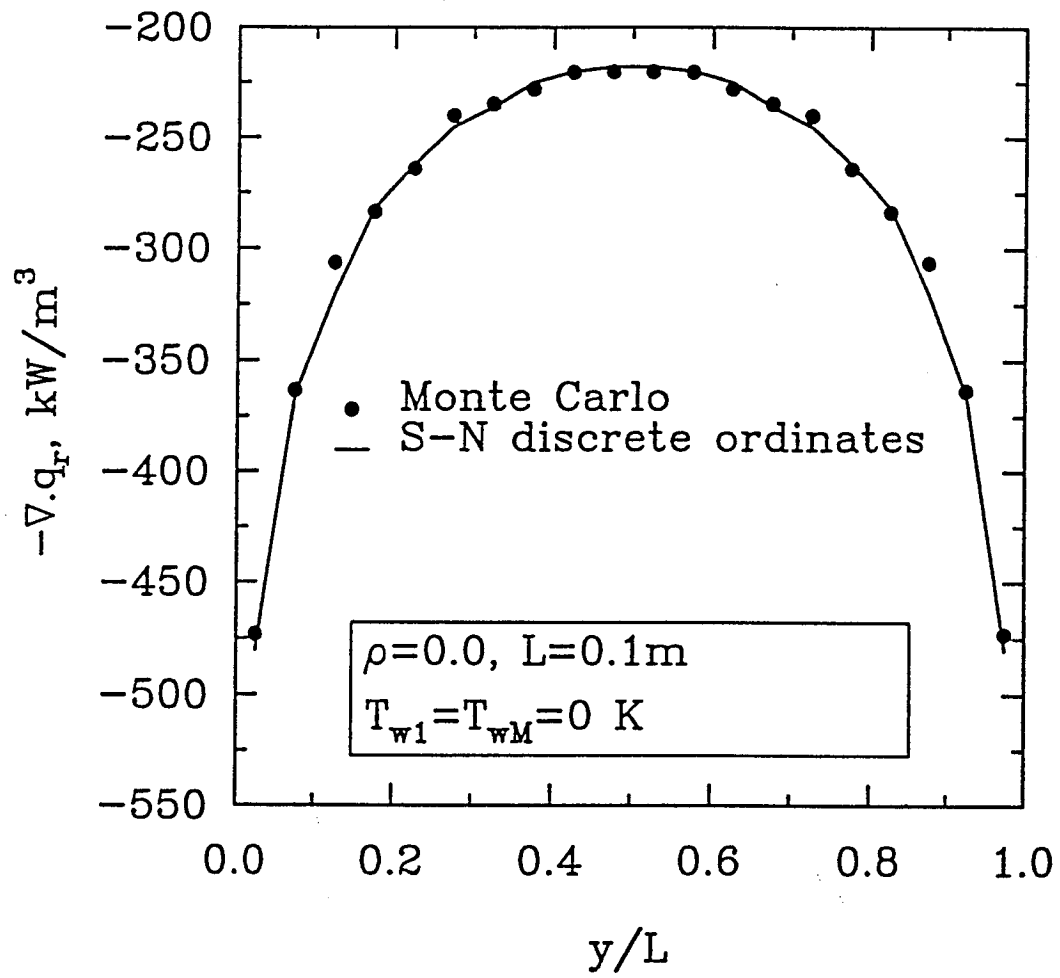


Fig. 3.3 Comparison of radiative source term for the uniform temperature profile with  $L=0.1 \text{ m}$ .

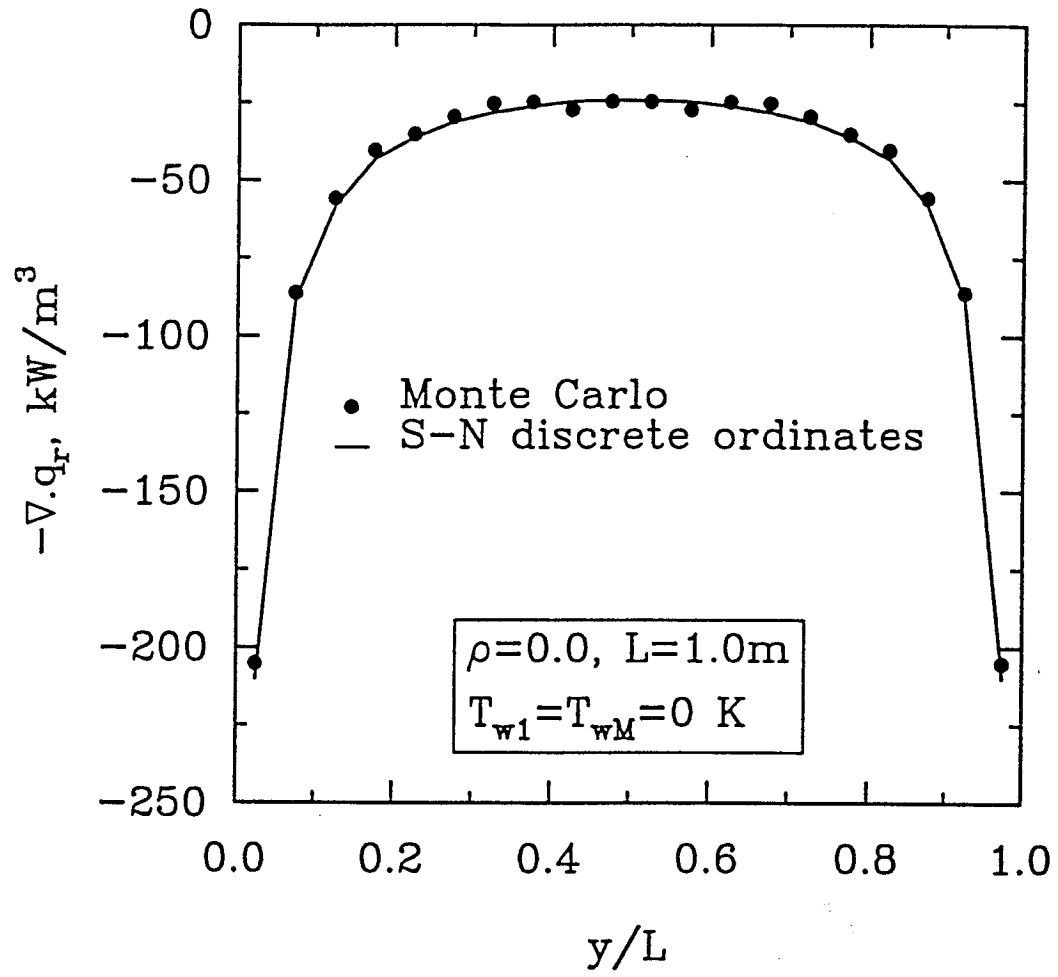


Fig. 3.4 Comparison of radiative source term for the uniform temperature profile with  $L=1.0 \text{ m}$ .

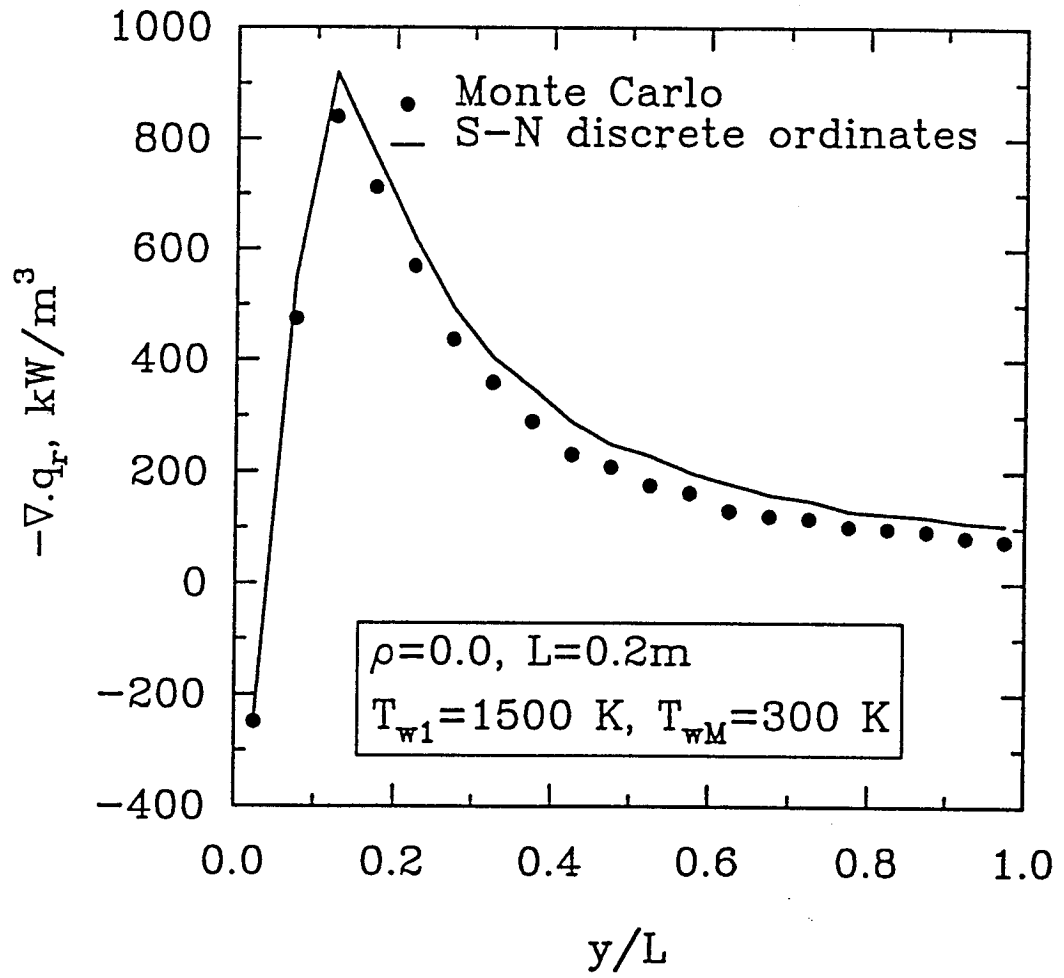


Fig. 3.5 Comparison of radiative source term for the boundary layer type temperature profile.

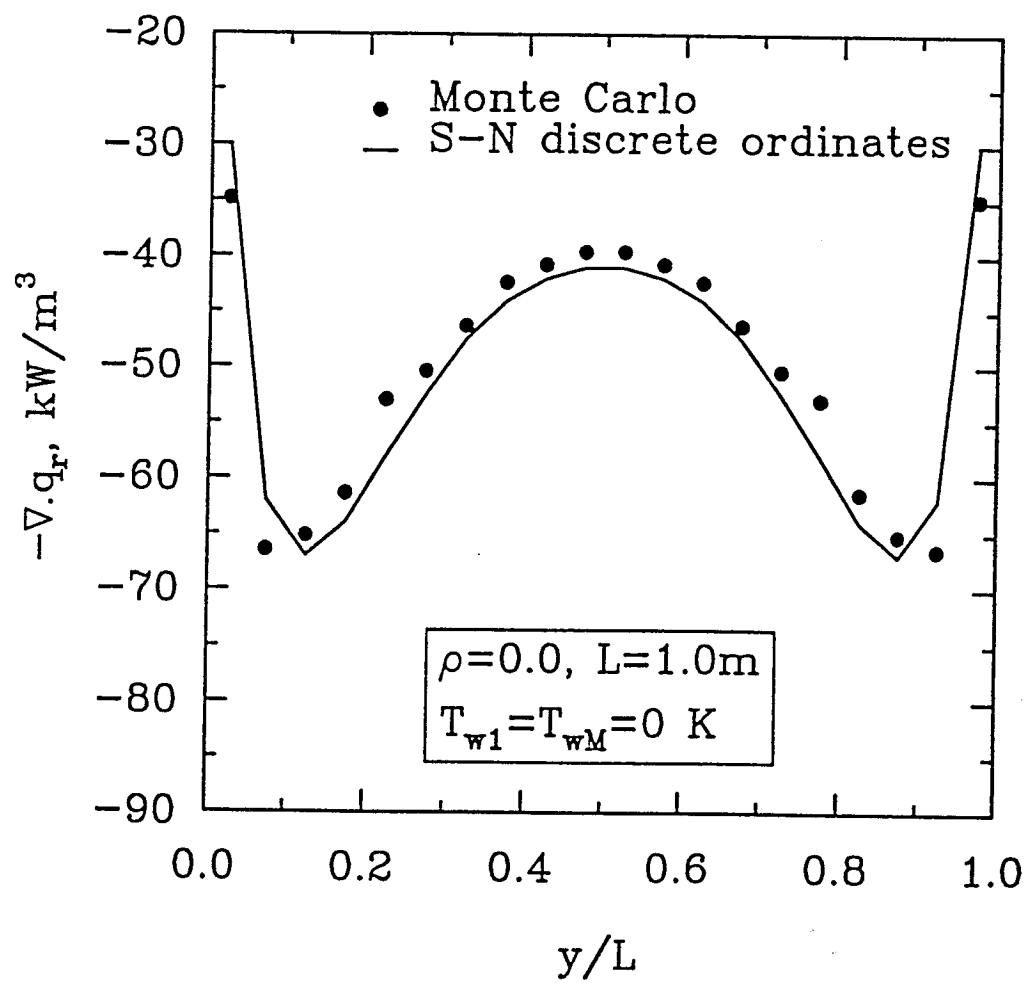


Fig. 3.6 Comparison of radiative source term for the parabolic  $\text{H}_2\text{O}$  concentration profile.

for the parabolic  $H_2O$  concentration distribution (with a uniform temperature profile) are shown in Fig. 3.6. The Monte Carlo method also predicts the interesting W type shape distribution of  $-\nabla \cdot q_r$  as in the S-N discrete ordinates method. Here the Monte Carlo solutions appear to be a little higher than the S-N discrete ordinates solutions, especially in the central region.

The results for the net radiative wall heat flux obtained for the cases presented in Figs. 3.3-3.6 are given in Table 3.2. The differences in results between the different solutions for the three cases are less than 3.5%. This shows agreement similar to that for the radiative source results.

The situation with reflecting walls is considered next. Figures 3.7-3.11 show the comparisons between the Monte Carlo solutions and the S-N discrete ordinates solutions for different wall reflectivities and slab thicknesses. For these results, the parabolic type temperature profile and the uniform composition of pure  $H_2O$  vapor at 1 atm were assumed. The S-N discrete ordinates solutions were based on the second-degree closure results [56]. The second-degree closure means that the history of two reflections is considered in the radiative flux equation and the remaining reflections are approximated by a closure method. Based on the study by Kim et al. [64], the second-degree discrete ordinates solutions for typical cases required about 160 minutes on a Cray-2 supercomputer. This is significantly higher than the CPU time required for the MCM, which is not more than 10 minutes on a Sun Sparc workstation.

Figures 3.7-3.9 present the results of  $-\nabla \cdot q_r$  for the wall reflectivities of  $\rho = 0.1$ , 0.5 and 0.9 respectively, with a slab thickness of  $L=0.5m$ . Excellent agreement between different solutions is seen in the figures. In the central region, the values of  $-\nabla \cdot q_r$  are approximately constant. The Monte Carlo results appear to oscillate in that region. The reason is that the total number of energy bundles is a finite number and the Monte Carlo results are of a statistical nature. The oscillation decreases and the results of  $-\nabla \cdot q_r$  become smoother as the total number of energy bundles is increased. These oscillations



Table 3.2 Comparison of net radiative wall heat fluxes with nonreflecting walls (kW/m<sup>2</sup>)

	Monte Carlo	S-N Discrete Ordinates
Uniform T; L=0.1 m	-14.2	-14.3
Uniform T; L=1.0 m	-27.6	-28.2
Boundary layer T	280.4	277.4
Uniform T with concentration profile	-24.5	-25.4

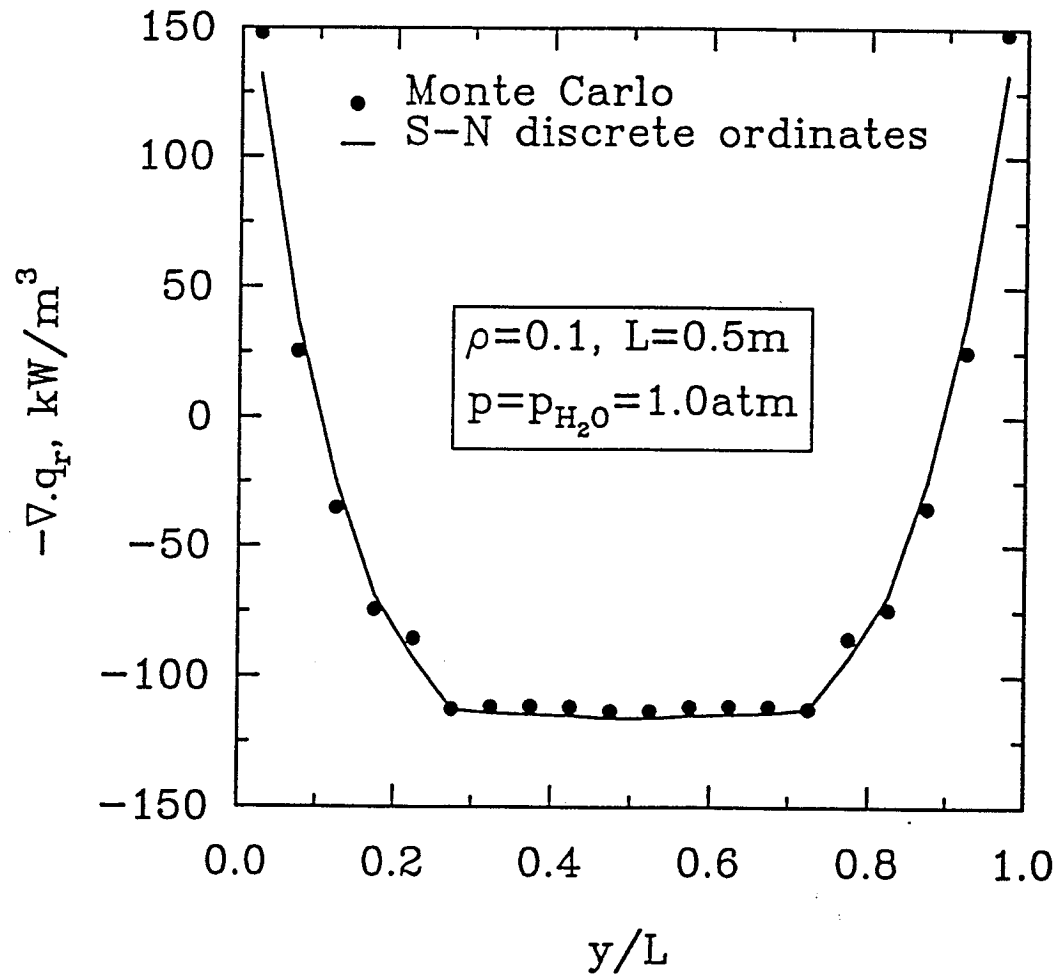


Fig. 3.7 Comparison of radiative source term in pure  $\text{H}_2\text{O}$  for  $\rho=0.1, L=0.5 \text{ m}$ .

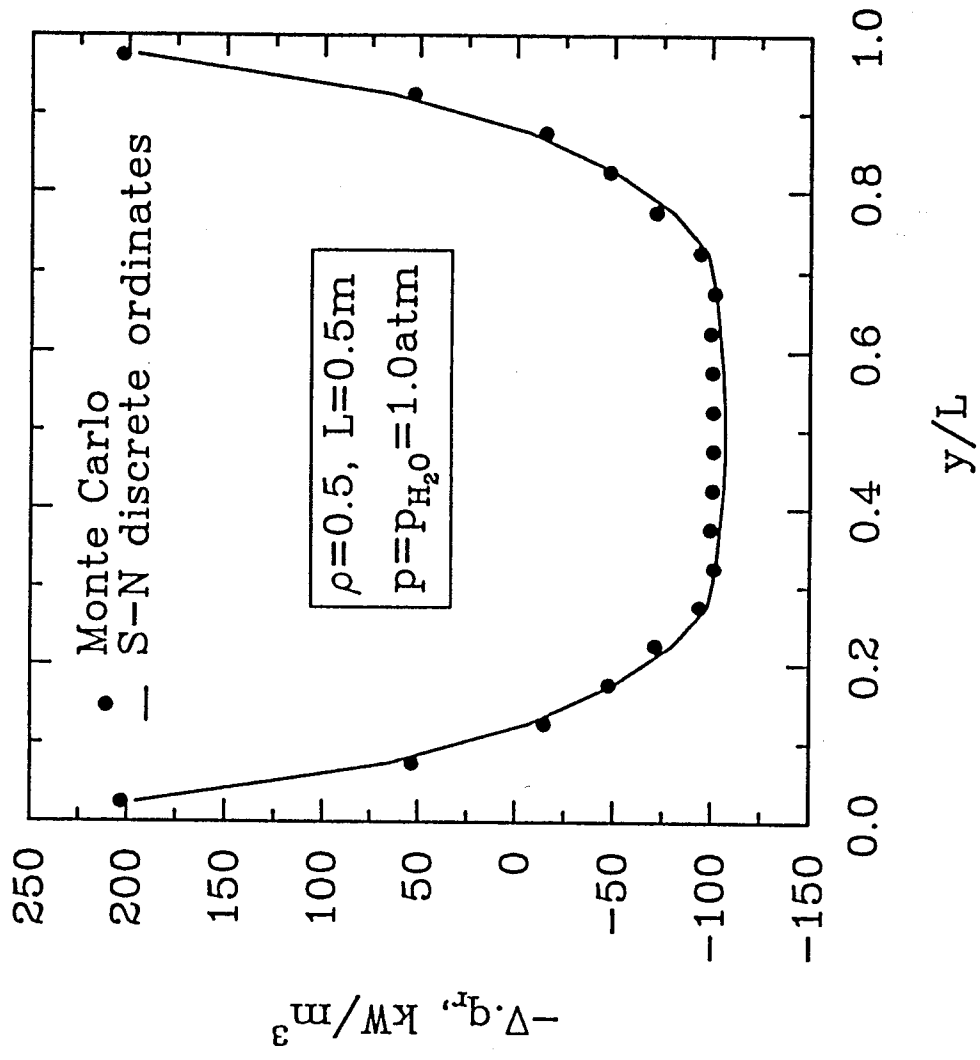


Fig. 3.8 Comparison of radiative source term in pure  $\text{H}_2\text{O}$  for  $\rho=0.5$ ,  $L=0.5$  m.

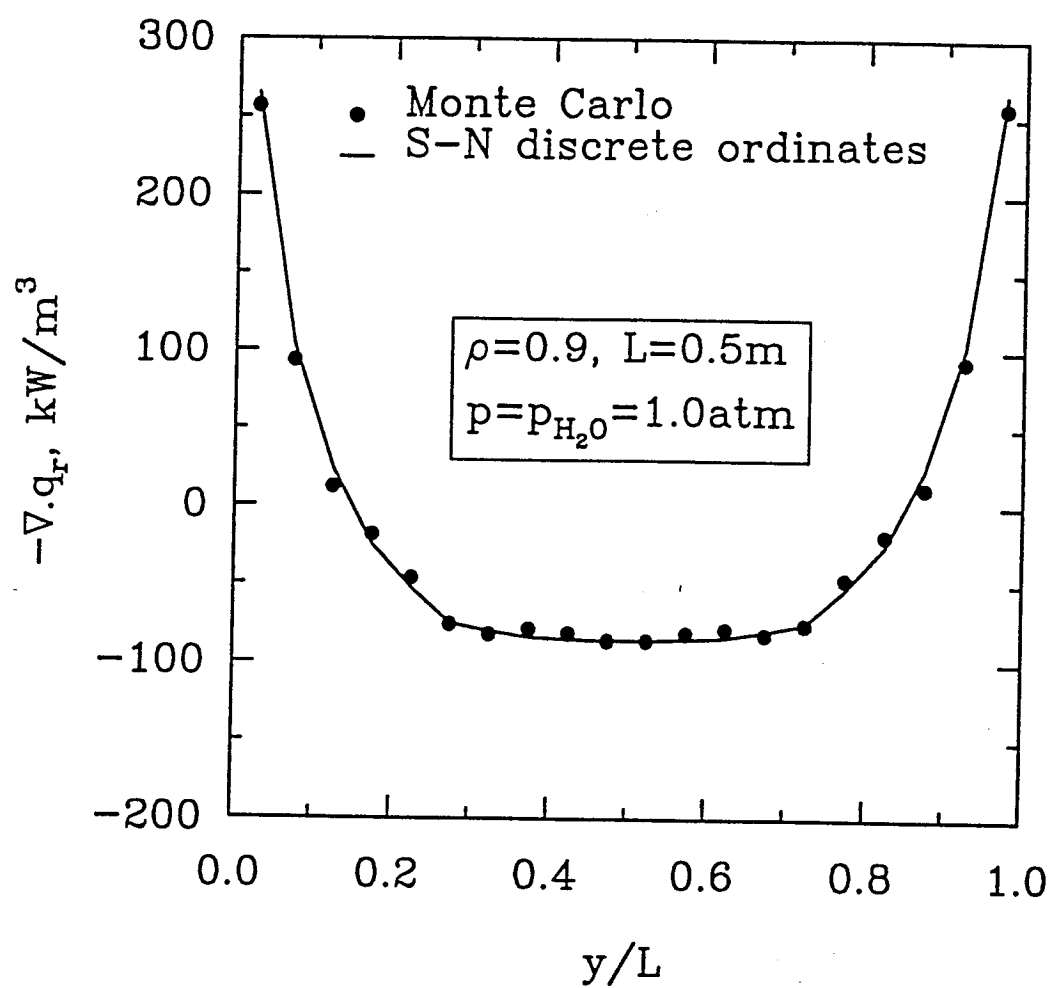


Fig. 3.9 Comparison of radiative source term in pure  $\text{H}_2\text{O}$  for  $\rho=0.9$ ,  $L=0.5$  m.

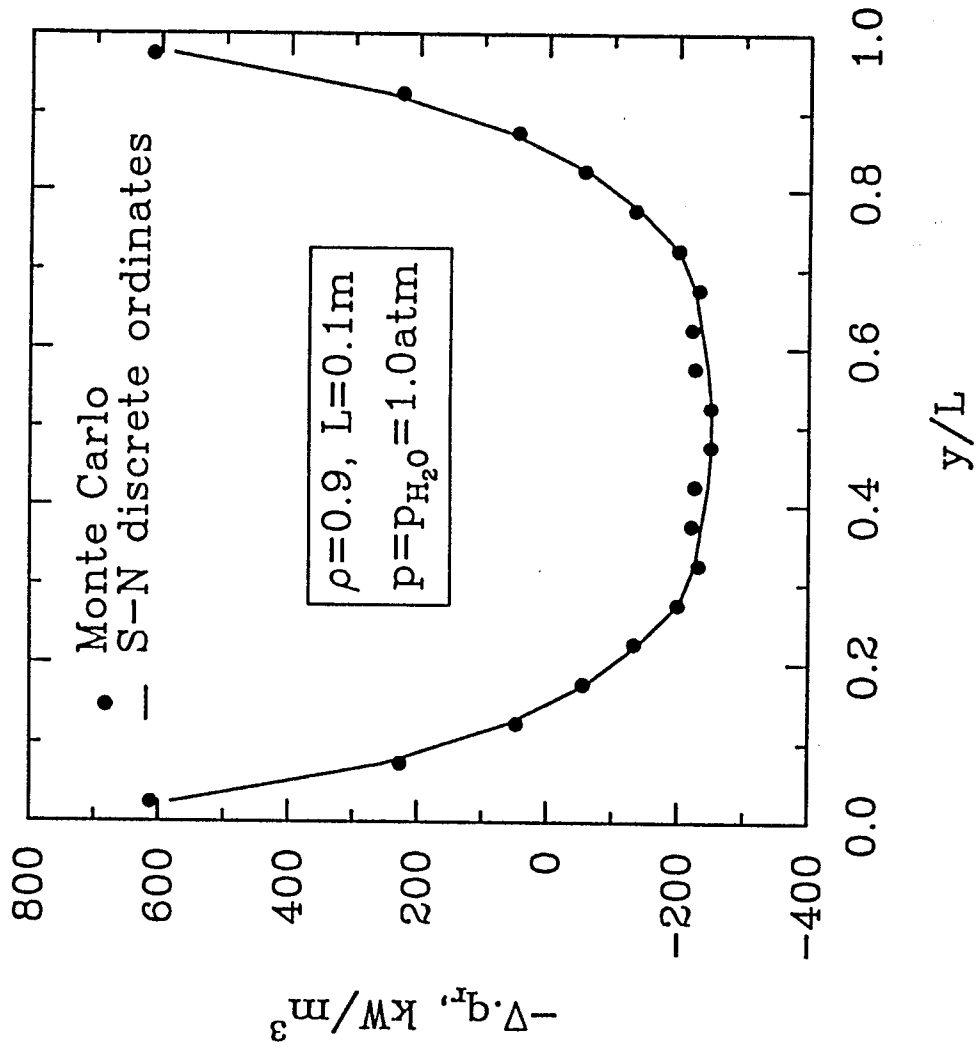


Fig. 3.10 Comparison of radiative source term in pure  $\text{H}_2\text{O}$  for  $\rho=0.9$ ,  $L=0.1\text{ m}$ .

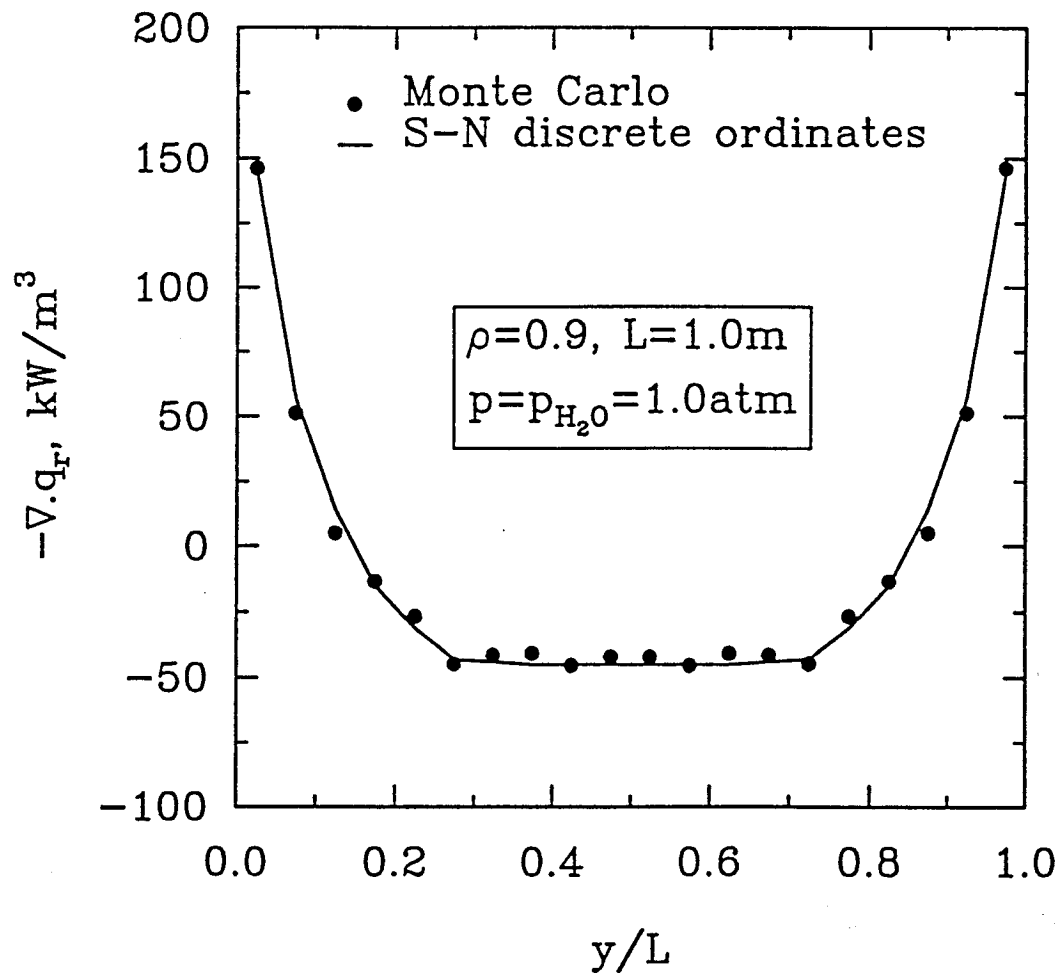


Fig. 3.11 Comparison of radiative source term in pure  $\text{H}_2\text{O}$  for  $\rho=0.9$ ,  $L=1.0\text{ m}$ .

are also exhibited in other figures. Figures 3.10 and 3.11 show the results for the strongly reflecting walls where  $\rho=0.9$ , with slab thicknesses of  $L=0.1$  m and  $L=1.0$  m, respectively. Again, the Monte Carlo solutions are in good agreement with the S-N discrete ordinates solutions.

Table 3.3 shows the net radiative wall heat fluxes for the cases presented in Figs. 3.7–3.11. The Monte Carlo results are slightly lower than the S-N discrete ordinates results. But the differences are within 6%. There are physical justifications for such discrepancies. In the S-N discrete ordinates method, the history of two reflections is taken into account and the remaining reflections are approximated as travelling in a medium without any attenuation. This approximation overpredicts the radiative energy absorbed on the walls. In the MCM, the history of the reflections is simulated in an exact manner. The Monte Carlo solutions are also subject to small statistical errors.

The spectrally correlated results are compared with the noncorrelated results in Figs. 3.12 and 3.13. A spectral correlation has been considered in all the results presented in previous figures. In a spectrally noncorrelated formulation, the correlation between spectrally dependent quantities is neglected. By using Eq. (3.14), the Monte Carlo noncorrelated results can be obtained. The temperature and  $H_2O$  concentration distributions considered here are the same as those in Figs. 3.7–3.11. The wall reflectivities are  $\rho=0.0$  for Fig. 3.12 and  $\rho=0.5$  for Fig. 3.13, and slab thickness  $L$  is 0.1 m for both cases. The figures show clearly that the noncorrelated results overestimate the gas emission in the central region, and differ by about 30–35% from the correlated results. The reason for these discrepancies is in the derivation of the statistical relationship for determining the location of absorption of an energy bundle. The term  $\overline{\tau_\omega(s \rightarrow s')\tau_\omega(s' \rightarrow s'')}$  in Eq. (3.12) can be treated in two different ways, that is,  $\overline{\tau_\omega(s \rightarrow s')\tau_\omega(s' \rightarrow s'')} = \overline{\tau_\omega(s \rightarrow s'')} \cdot \overline{\tau_\omega(s' \rightarrow s')}$ , respectively. The first choice results in the correlated formulation given by Eq. (3.13) and the second choice results in the noncorrelated formulation given by Eq. (3.14). Since the value of

Table 3.3 Comparison of net radiative wall heat fluxes with reflecting walls (kW/m<sup>2</sup>)

	L (m)	Monte Carlo	S-N Discrete Ordinates
$\rho=0.1$	0.5	14.42	15.12
$\rho=0.5$	0.5	9.47	9.66
$\rho=0.9$	0.1	2.22	2.34
	0.5	2.55	2.70
	1.0	2.58	2.67



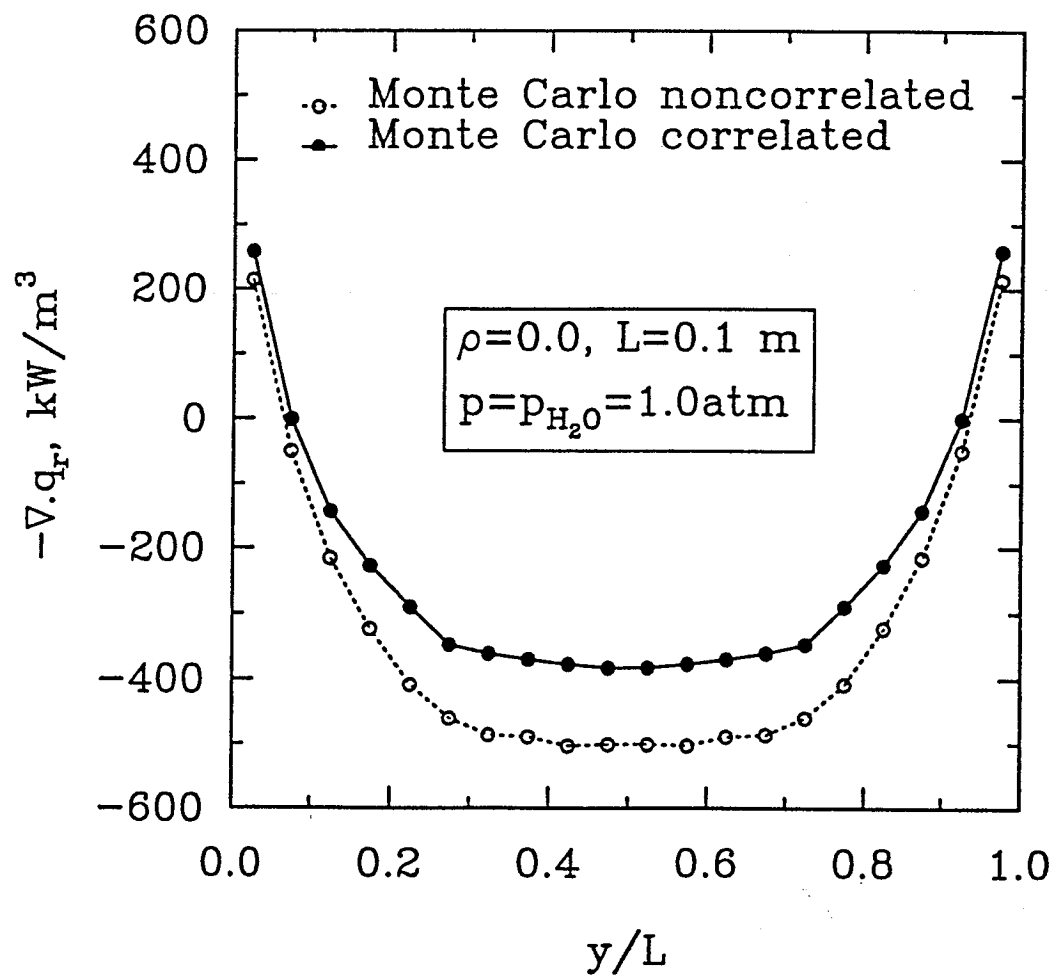


Fig. 3.12 Comparison of correlated and noncorrelated results in pure  $\text{H}_2\text{O}$  for  $\rho=0.0, L=0.1 \text{ m}$ .



## Chapter 4

### RADIATIVE INTERACTIONS IN LAMINAR FLOWS USING MONTE CARLO SIMULATION

In order to further establish validity of the MCM, a relatively simple problem of radiative interactions is considered. The physical problem considered is that of steady-state energy transfer in laminar, incompressible, fully developed flow with constant properties in an absorbing-emitting gas between two parallel plates (Fig. 4.1). The condition of uniform surface heat flux is assumed such that the surface temperature varies in the axial direction. This problem is selected because gray as well as nongray solutions for this case are available in the literature [5, 65].

#### 4.1 Basic Theoretical Formulation

The energy equation for the presical physical system can be expressed as [8]

$$\rho C_p \left( u \frac{\partial T}{\partial x} + v \frac{\partial T}{\partial y} \right) = k \frac{\partial^2 T}{\partial y^2} + \beta T u \frac{dp}{dx} + \mu \left( \frac{\partial u}{\partial y} \right)^2 - \nabla \cdot q_r \quad (4.1)$$

where  $u$  and  $v$  denote the  $x$  and  $y$  components of velocity, respectively. In deriving Eq. (4.1), it has been assumed that the net conductive heat transfer and radiative heat transfer in the  $x$  direction (parallel to the plates) can be neglected in comparison to the flux variations in the  $y$  direction (normal to the plates). If, in addition, it is assumed that the Eckert number of the flow is small, then Eq. (4.1) reduces to

$$\rho C_p \left( u \frac{\partial T}{\partial x} + v \frac{\partial T}{\partial y} \right) = k \frac{\partial^2 T}{\partial y^2} - \frac{\partial q_r}{\partial y} \quad (4.2)$$

The neglect of axial conduction and radiation in Eq. (4.2) is consistent with the formulation used in Ref. 9.

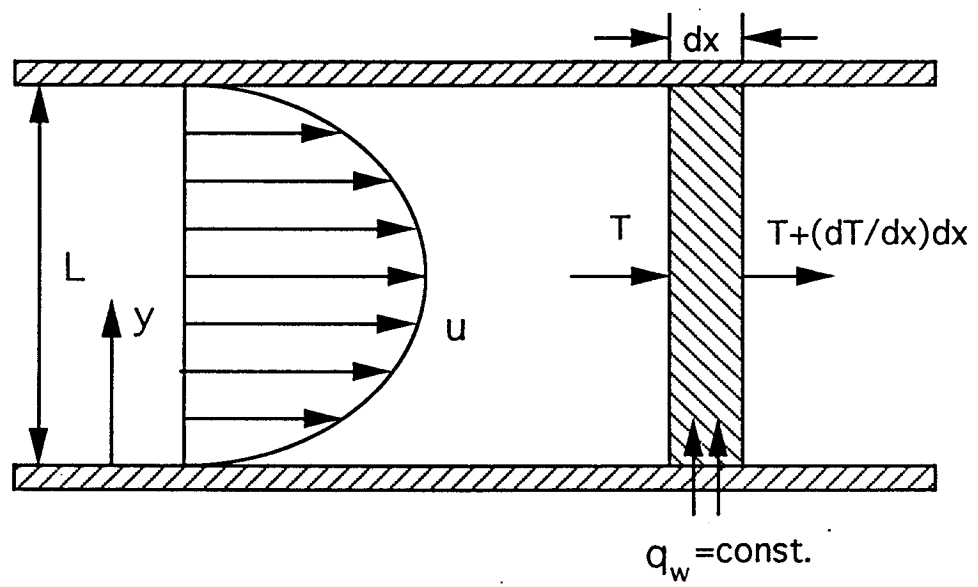


Fig. 4.1 Laminar flow between parallel plates with constant wall heat flux.

For a fully-developed flow,  $v=0$ , and  $u$  is given by the well-known parabolic profile as

$$u = 6u_m(\xi - \xi^2); \quad \xi = y/L \quad (4.3)$$

where  $u_m$  represents the mean fluid velocity. Also, for the flow of a perfect gas with uniform heat flux,  $\partial T/\partial x$  is constant and is given by

$$\partial T/\partial x = (2\alpha q_w)/(u_m L k) \quad (4.4)$$

A combination of Eqs. (4.2)-(4.4), therefore, results in

$$k \frac{\partial^2 T}{\partial y^2} - \frac{\partial q_r}{\partial y} - \frac{12q_w}{L}(\xi - \xi^2) = 0 \quad (4.5)$$

Equation (4.5) is the governing energy equation for the parallel plates geometry. The boundary conditions for this problem can be expressed as

$$T(0) = T(L) = T_w; \quad \frac{\partial T}{\partial y}(y = L/2) = 0 \quad (4.6)$$

It should be noted that all boundary conditions given in Eq. (4.6) are not independent; any two convenient conditions can be used to obtain specific solutions.

The radiative transfer term in the energy equation makes computation difficult because it turns the differential equation into an integro-differential equation. One exception is for the case of a gray medium. In this case, the equation for radiative transfer is expressed as [8]

$$\frac{1}{\kappa_p^2} \frac{d^2 q_r(y)}{dy^2} - \frac{9}{4} q_r(y) = \frac{3}{2} \sigma \frac{dT^4}{dy} \quad (4.7)$$

Equation (4.7) is a second order differential equation and, therefore, requires two boundary conditions. For black walls and  $T_{w1}=T_{w2}$ , the boundary conditions for Eq. (4.7) become

$$q_r(L/2) = 0; \quad \frac{3}{2} q_r(0) = \frac{1}{\kappa_p} (dq_r/dy)_{y=0} \quad (4.8)$$

In the present study, attention is directed on the MCM in solving the radiative transfer term for a gray as well as a nongray medium. Before going into a detailed numerical analysis of the energy equation including the radiative transfer term, it is essential to define the quantity of primary interest.

For heat transfer in simple flow problems, the quantity of primary interest is the bulk temperature of the gas. For a fully-developed flow between parallel plates, this is expressed as

$$\theta_b = (T_b - T_w)/(q_w L/k) = 6 \int_0^1 \theta(\xi)(\xi - \xi^2) d\xi \quad (4.9)$$

where  $q_w = \bar{h}(T_w - T_b)$ , and  $\bar{h}$  represent the equivalent heat transfer coefficient ( $\text{W}/\text{cm}^2\text{-K}$ ).

## 4.2 Solution Procedure

There are two levels to the numerical method proposed here. The first is concerned with the discretization and solution of the energy equation, while the second is due to the numerical evaluation of the radiative flux term that is included in the energy equation.

The energy equation, Eq. (4.5), is discretized by a finite volume technique. The domain between two parallel plates is divided equally into  $N$  finite volume elements. For the  $i$ th finite volume elements,  $\delta V_i$ , a combination of Eqs. (4.5) and (3.1) results in the discretized energy equation as

$$k \frac{T_{i+1} - 2T_i + T_{i-1}}{\Delta y} - \frac{12q_w \Delta y}{L} (\xi_i - \xi_i^2) + Q_{V-\delta V_i} + Q_{A-\delta V_i} - Q_{\delta V_i} = 0 \quad (4.10)$$

where the conductive heat transfer is discretized by a central difference scheme and the radiative heat transfer consists of  $Q_{V-\delta V_i}$ ,  $Q_{A-\delta V_i}$  and  $Q_{\delta V_i}$  terms. The energy balance in each volume element results in a set of simultaneous equations equal to the total number

of finite volume elements. Each equation contains an unknown temperature which cannot be calculated independently and an iterative solution is necessary.

Before solving the energy equation, the radiative energy interchange in each equation must be evaluated. In this study, the radiative terms  $Q_{V-\delta V_i}$ ,  $Q_{A-\delta V_i}$  and  $Q_{\delta V_i}$  are simulated by the MCM. For the gray medium, the Monte Carlo formulations employed are from Refs. 6 and 7. For the nongray medium, the one-dimensional Monte Carlo formulations, as presented in Eqs. (3.7)-(3.9) and (3.14), have been applied.

In the Monte Carlo simulation,  $Q_{V-\delta V_i}$  and  $Q_{A-\delta V_i}$  are obtained based on the assumed temperature distribution; a new temperature distribution can be calculated by solving the set of simultaneous equations given by Eq. (4.10). Two typical methods have been developed to solve the energy equation with the Monte Carlo simulation. In one of these methods [66, 67], convective and conductive heat transfer, as well as  $Q_{V-\delta V_i}$  and  $Q_{A-\delta V_i}$ , are calculated based on the assumed temperature distribution, a new temperature distribution is obtained from the term  $Q_{\delta V_i}$  in the energy equation. The numerical experiments conducted in this study indicate that this method has a high probability of producing divergent simulation and, therefore, it is not suitable for problems with large variations in optical length. In the other method [20], only  $Q_{V-\delta V_i}$  and  $Q_{A-\delta V_i}$  are calculated based on the assumed temperature distribution, a new temperature distribution which is included in the convective and conductive heat transfer terms, as well as  $Q_{\delta V_i}$ , is obtained by solving a set of non-linear equations. This latter method was employed in the present study and the solution was obtained by using the NEQNF routine, which solves a system of non-linear equations in IMSL Library Package [68]. The change in local temperature in each iteration of the calculation is determined and when the maximum change is less than  $10^{-4}$ , the solution is considered to have converged.

The radiative heat transfer can be calculated easily by the MCM, but the accuracy of the results obtained is affected by the number of the radiative energy bundles used in a calculation. If high accuracy is needed, it will be necessary to take longer computational

time even if a simple model is analyzed. Several methods are available to reduce the computing time and obtain higher accuracy. One of these methods, applied to the gray gas, is the differential emissive power emission (DPE) method [66, 67]. In the DPE method, not only positive radiative energy bundles but also negative bundles are used, and the number of energy bundles emitted from a gas element is proportional to the difference between emissive powers from two consecutive iterations. This treatment does not change the physical processes of the Monte Carlo simulation. The proof of the equivalence of the DPE and regular methods is given in the cited references.

### 4.3 Results and Discussion

Based on the theoretical and numerical analyses described in the previous sections, a computer code, which is given in Appendix B, has been developed to investigate gray as well as nongray radiation interactions in incompressible flows between two parallel plates. For the case of black walls, gray analytical solutions and nongray approximate solutions (based on the method of variation of parameters) are available in the literature [5, 65]. In this study, the Monte Carlo solutions have been compared with these results for identical conditions. The absorbing-emitting media considered were pure  $H_2O$  and  $CO_2$ . The results are expressed in terms of the non-dimensional bulk temperature. The plate spacings considered range from 0.01 cm to 100.0 cm. The calculation was carried out on a Sun Workstation. The domain was divided into 40 finite volume elements with equal thicknesses. The total number of energy bundles selected was 50,000 for nongray and 200,000 for gray simulations. The amount of energy per bundle depends on the temperature. One of the important parameters related to the temperature distribution is the heat flux from the plates; care should be taken to choose this heat flux. In the solutions from the literature [5, 65], the assumption of linearized radiation was made and the radiative properties were considered to be independent of temperature. In order to facilitate comparisons between the Monte Carlo solution and the approximate solution,



different values of heat flux at the wall were chosen when the plate spacings were changed. The CPU time requirement for a converged solution with a specific plate spacing was on the order of ten seconds for the gray case if the DPE method was applied and on the order 1000 seconds for the nongray case. The numerical experiments conducted in this study indicate that the DPE method can reduce the CPU time about an order of magnitude compared to the regular method without loss in the accuracy of results.

Figures 4.2–4.5 show comparisons between the gray analytical solutions and the gray Monte Carlo solutions for different media, temperatures, and pressures. The medium considered is  $\text{CO}_2$  in Figs. 4.2 and 4.3. In Fig. 4.2, the pressure of  $\text{CO}_2$  was kept at 1.0 atm but the plate temperatures were 500 and 1000 K. In Fig. 4.3, the wall temperature was kept at 1000 K but the pressures was changed from 1.0 to 5.0 atm. The figures show that the predictions by the MCM are very close to the analytical solutions at different temperatures and pressures. Figures 4.4 and 4.5 show the results for  $\text{H}_2\text{O}$ . Similar to the case for  $\text{CO}_2$ , the Monte Carlo solutions were found to be in good agreement with the analytical solutions in the  $\text{H}_2\text{O}$  medium at different temperatures and pressures. The results demonstrate that radiative interactions are enhanced and the temperature distribution becomes more uniform between the parallel plates with increases in temperature and pressure.

Figures 4.6–4.9 show comparisons between the nongray approximate solutions based on the method of variation of parameters and the nongray Monte Carlo solutions for different media, temperatures, and pressures. The medium considered is  $\text{CO}_2$  for the results presented in Figs. 4.6 and 4.7. In Fig. 4.6, the pressure of  $\text{CO}_2$  was kept at 1.0 atm but plate temperature was changed from 500 to 1000 K. In Fig. 4.7, the wall temperature was kept at 1000 K but the pressure was varied from 1.0 to 5.0 atm. The figures show that the Monte Carlo solutions compare favorably with the approximate solutions at different temperatures and pressures. Figures 4.8 and 4.9 show the results for  $\text{H}_2\text{O}$ . Similar to the case of  $\text{CO}_2$ , the Monte Carlo solutions essentially match the

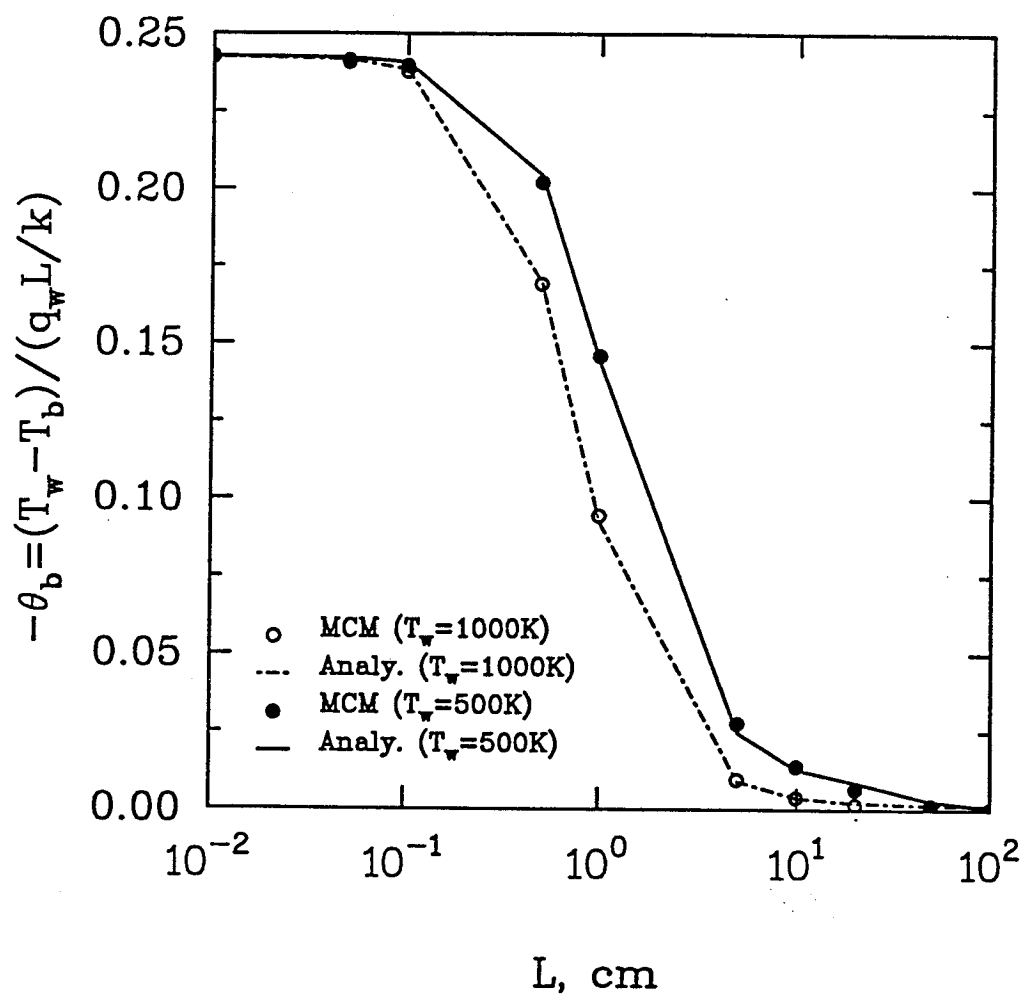


Fig. 4.2 Comparison of gray solutions for  $\text{CO}_2$  at  $p=1 \text{ atm}$ .

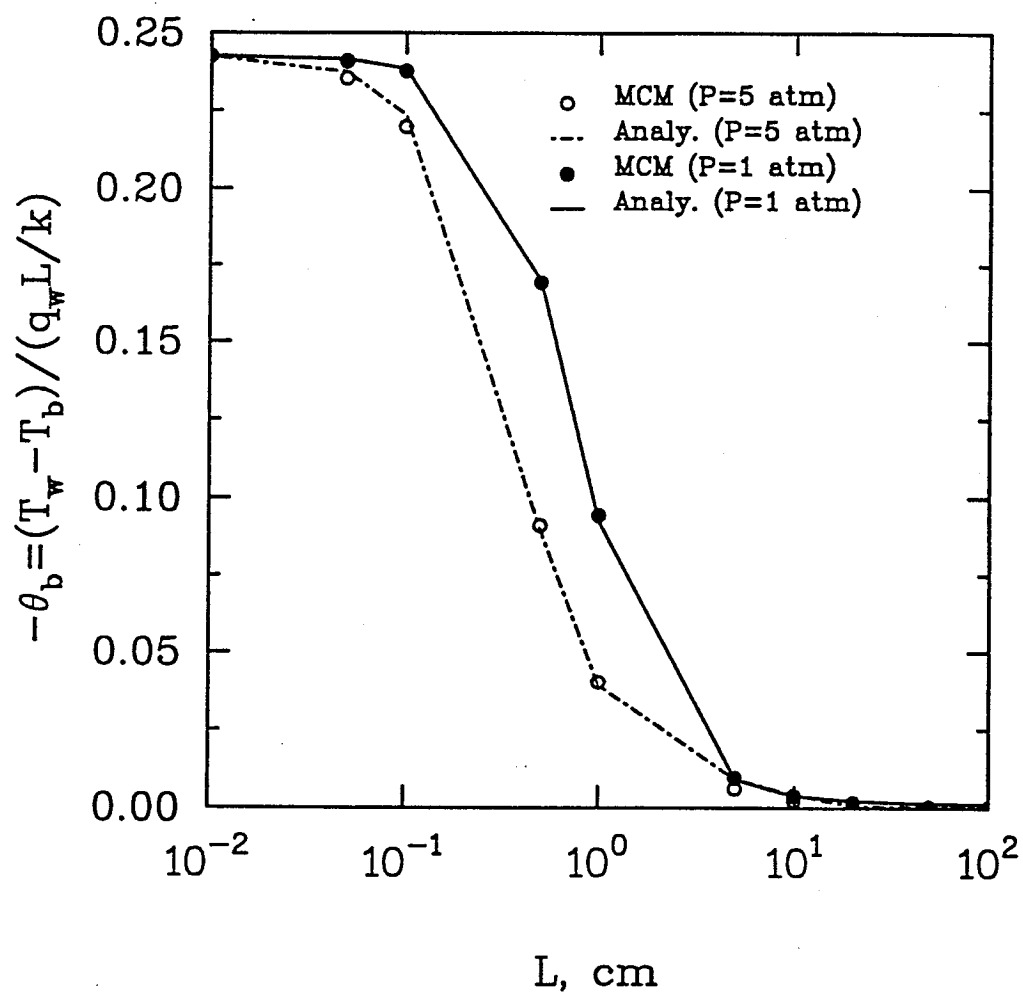


Fig. 4.3 Comparison of gray solutions for CO<sub>2</sub> at  $T_w=1000$  K.

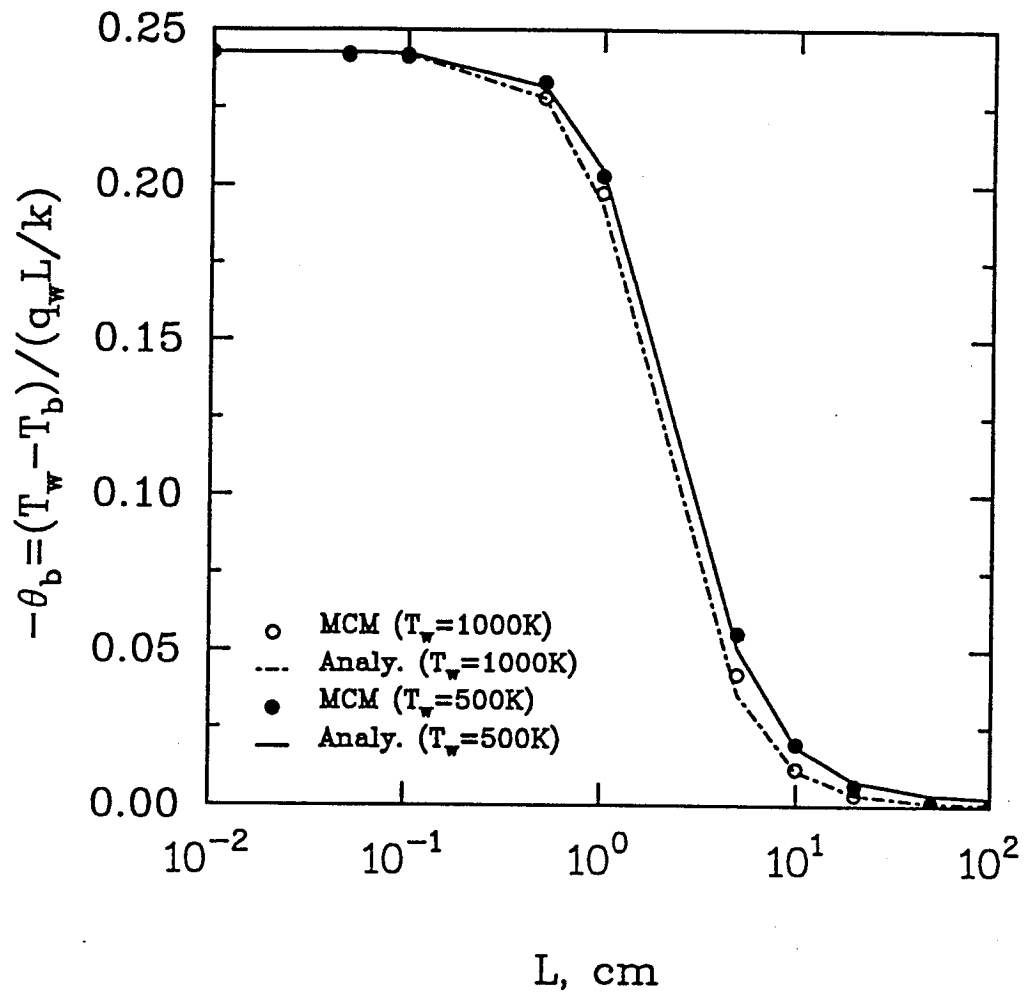


Fig. 4.4 Comparison of gray solutions for  $\text{H}_2\text{O}$  at  $p=1 \text{ atm}$ .

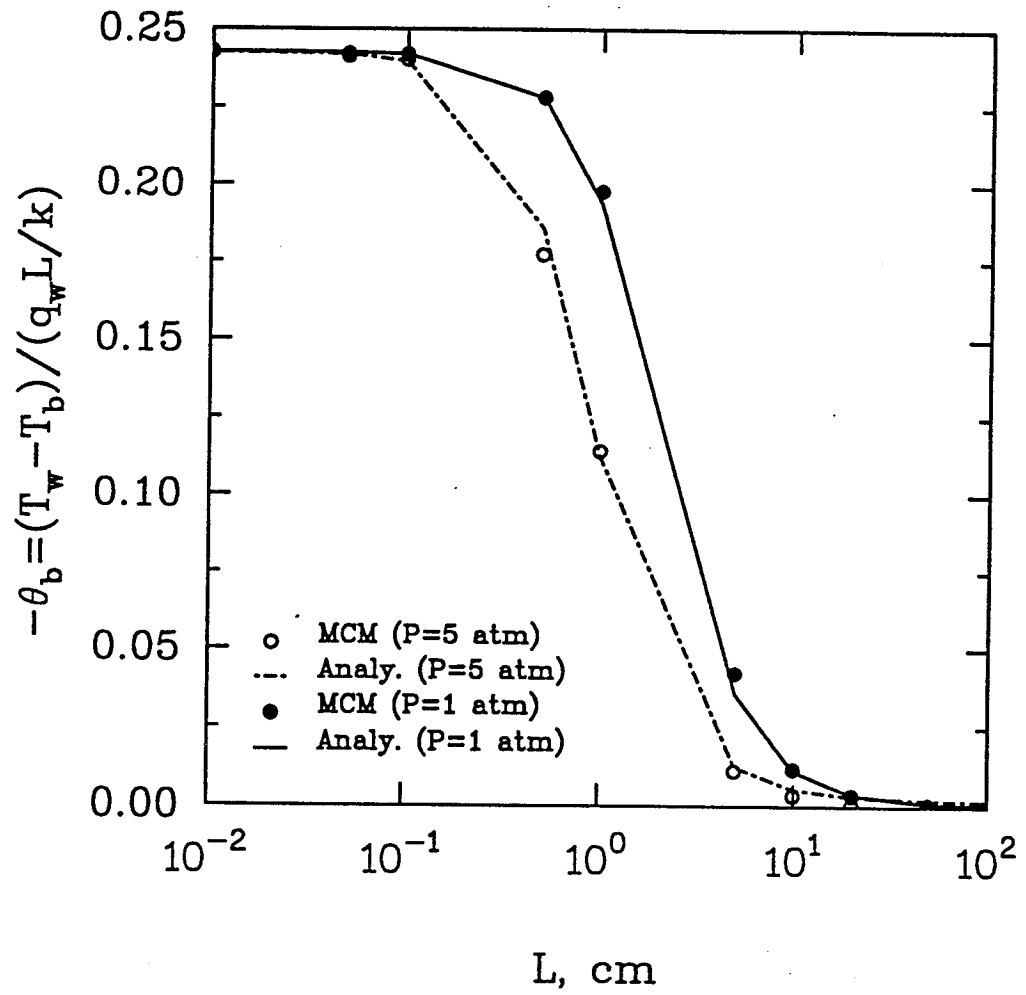


Fig. 4.5 Comparison of gray solutions for H<sub>2</sub>O at T<sub>w</sub>=1000 K.

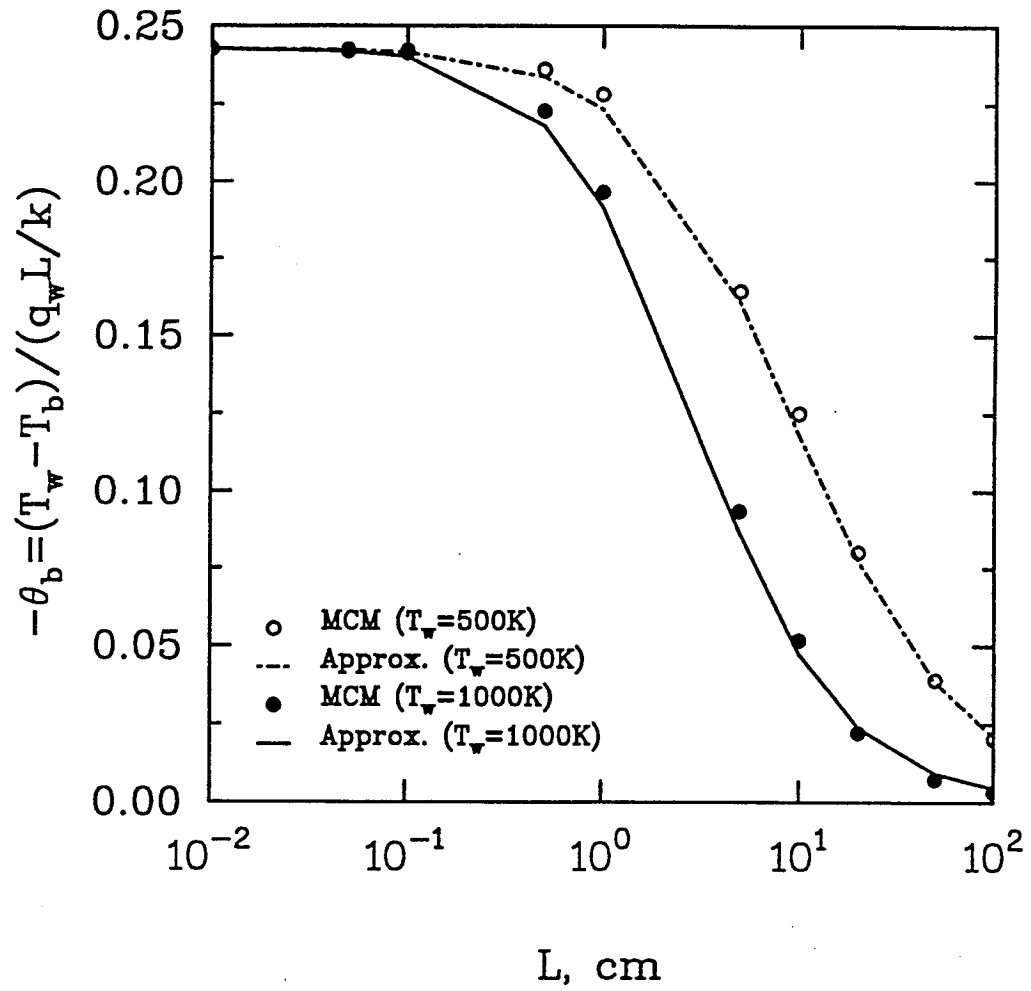


Fig. 4.6 Comparison of nongray solutions for  $\text{CO}_2$  at  $p=1 \text{ atm}$ .

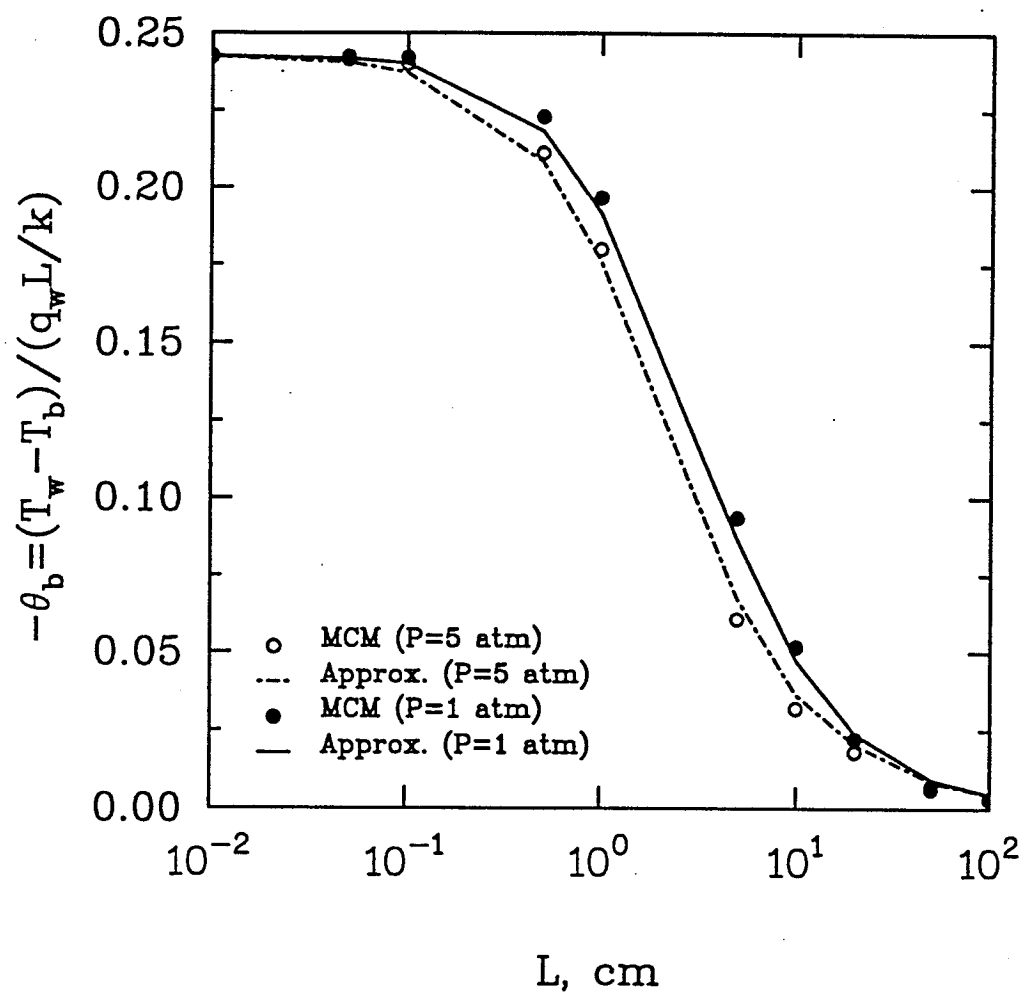


Fig. 4.7 Comparison of nongray solutions for  $\text{CO}_2$  at  $T_w=1000 \text{ K}$ .

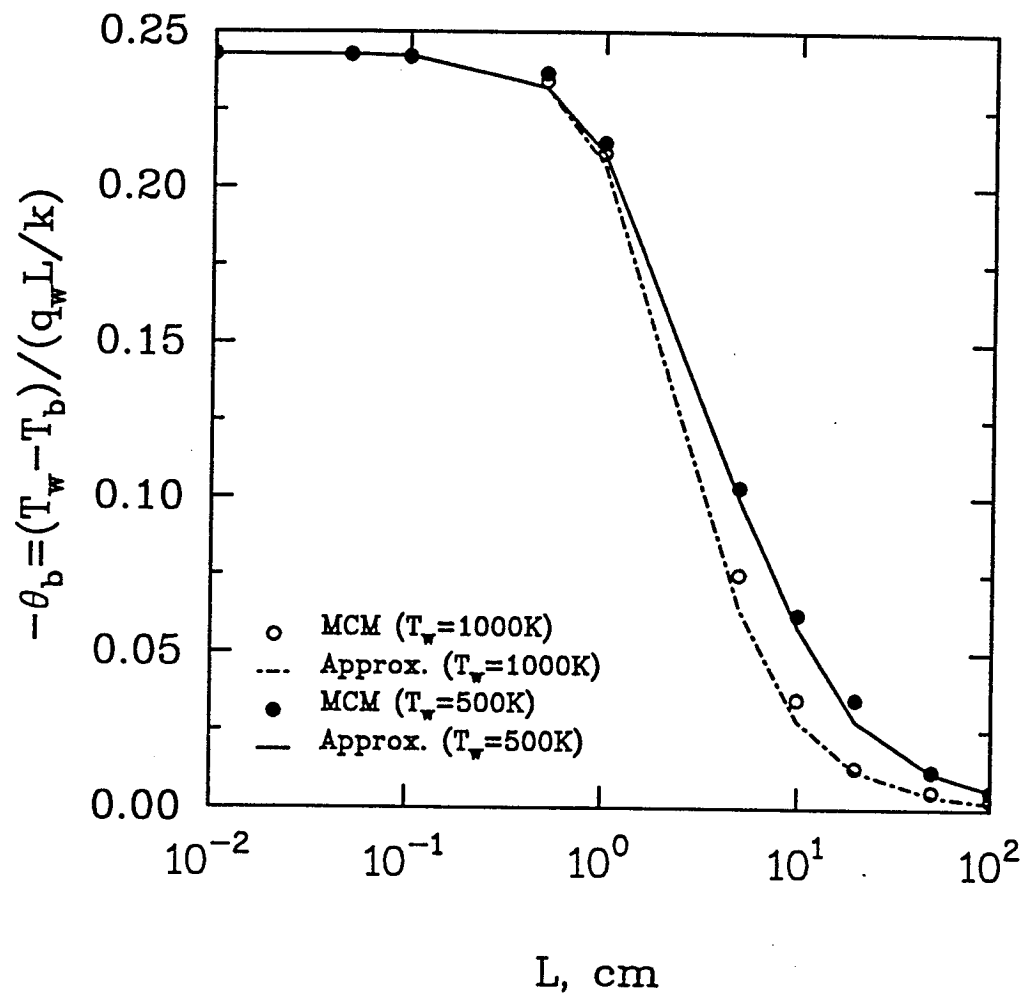


Fig. 4.8 Comparison of nongray solutions for  $\text{H}_2\text{O}$  at  $p=1 \text{ atm}$ .



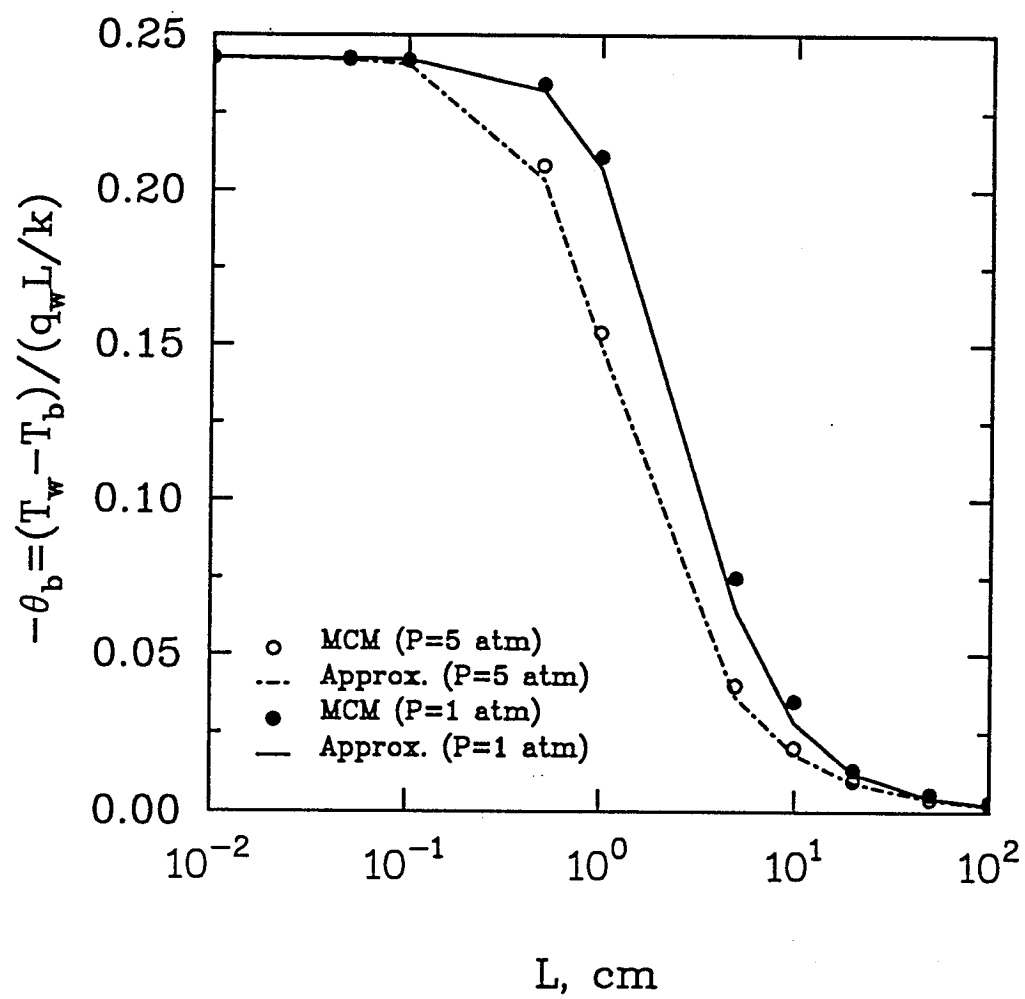


Fig. 4.9 Comparison of nongray solutions for H<sub>2</sub>O at T<sub>w</sub>=1000 K.

analytical solutions for  $H_2O$  at different temperatures and pressures. The effects of an increase in temperature and pressure on the radiative interactions and the temperature distributions between the parallel plates in the nongray cases are also found to be similar to those in the gray cases.

The results presented in this chapter demonstrate clearly that the one-dimensional nongray Monte Carlo formulations developed in the previous chapter are very reliable and accurate. These formulations have been also applied to investigate the radiative interactions in entry region turbulent flows, and detailed information is available in Ref. 69.

## Chapter 5

### MONTE CARLO SIMULATION FOR RADIATIVE TRANSFER IN MULTI-DIMENSIONAL SYSTEMS

In Chap. 3, radiative heat transfer between two infinite parallel plates was simulated in an exact manner. However, application of this exact treatment to multi-dimensional problems can be extremely complicated and numerical solutions to these formulations can be very difficult. However, by introducing an appropriate assumption, the complicated Monte Carlo formulations in multi-dimensional problems can be simplified significantly. In this chapter, attention is directed to a two-dimensional problem. The physical problem is described in Sec. 5.1. The exact Monte Carlo formulations are developed in Sec. 5.2. The approximate Monte Carlo formulations are developed in Sec. 5.3. Comparisons between exact and approximate Monte Carlo solutions are made in Sec. 5.4.

#### 5.1 Physical Problem

Consider an absorbing and emitting molecular gas between two parallel plates of finite length  $L$  and height  $H$  and infinite width, as shown in Fig. 5.1. The inlet and outlet of the gas are at  $x=0$  and  $x=L$ , respectively, and both ends are treated as pseudoblack walls with prescribed temperatures. Temperature, concentration and pressure in the medium are assumed to be known. The walls are assumed to be diffuse but not necessarily gray. The wall temperature distribution is also specified. In order to calculate the radiative source term  $-\nabla \cdot q_r$  inside the medium and the net radiative wall flux  $q_{rw}$ , the medium considered is divided into an  $MX \times MY$  array of rectangular volume elements (Fig. 5.1). Similarly, the two real walls are each divided into  $MX$  surface elements, and the inlet and outlet

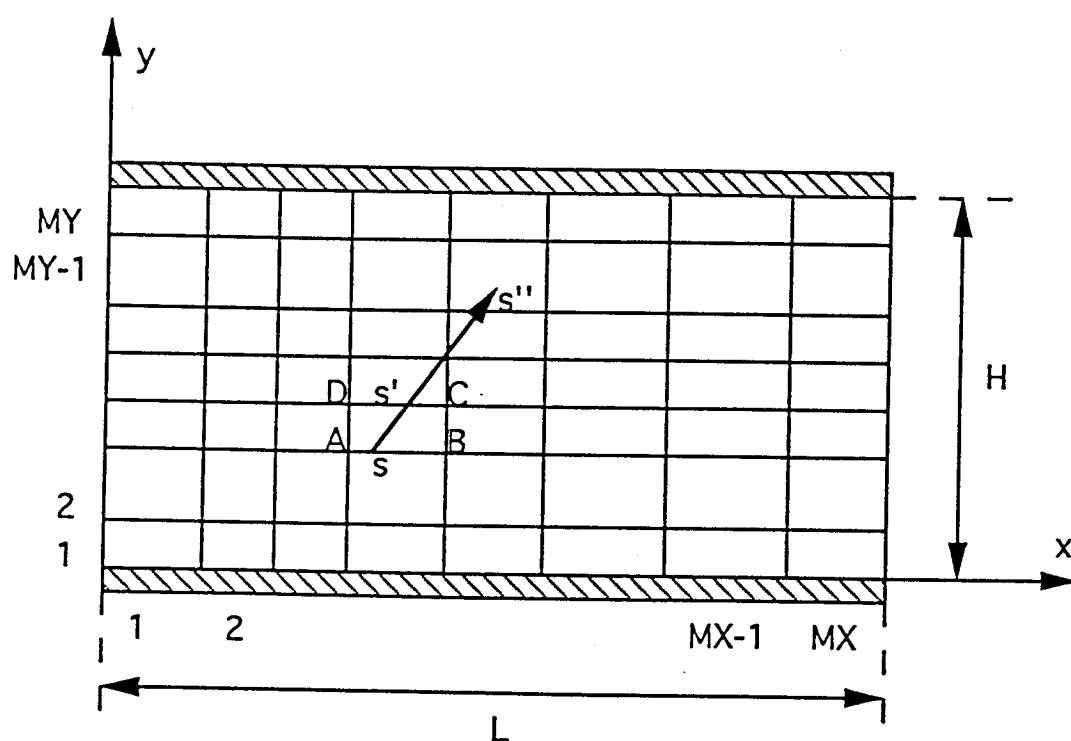


Fig. 5.1 Schematic of two finite parallel plates and grid configuration.

pseudo walls are each divided into MY surface elements. Temperature, concentration and pressure are assumed to be constant in each element.

The following Monte Carlo analysis is based on an arbitrarily chosen finite volume element ABCD (Fig. 5.2) with the length and height equal to  $b$  and  $c$ , respectively. Exact correlated and non-correlated formulations are derived first; then approximate correlated and non-correlated formulations are developed. The statistical relationships for an energy bundle emitted from a surface element in each case can be derived by following the same procedure.

## 5.2. Exact Correlated and Non-correlated Monte Carlo Formulations

In this case, an energy bundle is simulated in an exact manner in terms of the narrow band model without approximation. Let us consider the Planck spectral blackbody intensity  $I_{b\omega}$  that enters the element ABCD at some point  $s$  on side AB and intersects one of the other three sides of the element at the point  $s'$ , as shown in Fig. 5.2. It should be understood that each side of the element is a surface. A spherical coordinate system is established and centered at the point  $s$ . The distance between the points  $s$  and  $A$  is  $x^*$ . From Ref. 6, the amount of energy emitted in the wavenumber interval  $d\omega$ , along a pencil of column  $s \rightarrow s'$  with a solid angle increment  $d\Omega$  and an area increment  $dx^*$  is

$$dQ = I_{b\omega} [1 - \tau_\omega(s \rightarrow s')] \cos \theta d\Omega dx^* d\omega \quad (5.1)$$

The total emitted energy, calculated in terms of the intensity entering from the sides of AB ( $0 < \theta \leq \pi$ ) and DC ( $\pi < \theta \leq 2\pi$ ), is obtained by integrating Eq. (5.1) over the wavenumber, polar angle, azimuthal angle and area as

$$Q = \int_0^\infty \int_0^b \int_0^\pi \int_0^{2\pi} I_{b\omega} [1 - \tau_\omega(s \rightarrow s')] \cos \theta \sin \theta d\psi d\theta dx^* d\omega \quad (5.2)$$

Referring to Fig. 5.2, the distance  $ss'$  is expressed as

$$ss' = \begin{cases} \min \{c / \cos \theta, (b - x^*) / (\cos \psi \sin \theta)\}, & -\pi/2 < \psi \leq \pi/2 \\ \min \{c / \cos \theta, -x^* / (\cos \psi \sin \theta)\}, & \pi/2 < \psi \leq 3\pi/2 \end{cases} \quad (5.3)$$

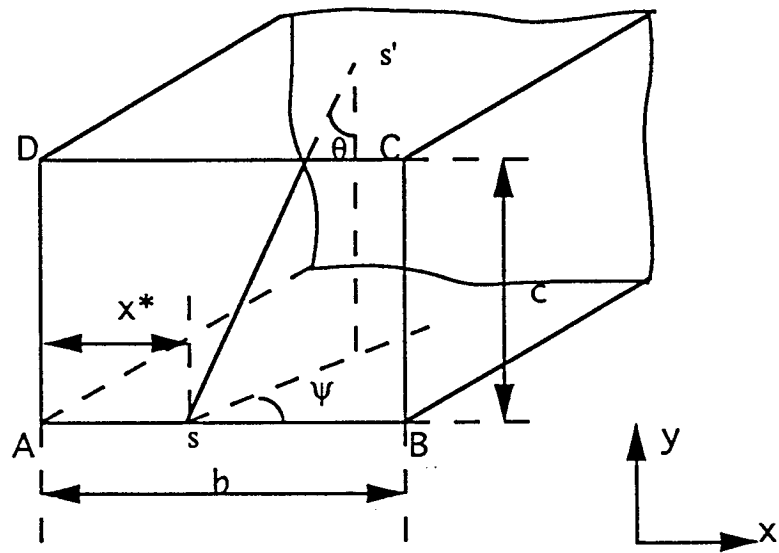


Fig. 5.2 Schematic of a rectangular finite volume element ABCD

The value of  $ss'$  cannot be calculated from just one expression because the point  $s'$  may be located on different sides of the element ABCD. All the possible travelling paths of the intensity in the element ABCD should be considered to evaluate the value of  $Q$ .

Similar procedures can be used to obtain expressions for the emitted radiative energy calculated in terms of the intensity entering from the sides of AD and BC. Thus, the total emitted radiative energy from the finite volume element ABCD consists of two terms. They represent the emitted energy calculated in terms of the intensities entering from sides AB, DC and from sides AD, BC, respectively, and cannot be manipulated algebraically into one term. Usually, the statistical relationships for simulating an energy bundle emitted from a volume element in the MCM are developed from the formulation for the total emitted radiative energy from this volume element. However, this can complicate the analysis since there exists two independent terms in the formulation of total emitted radiative energy. In this study, the two independent terms are treated separately, and the Monte Carlo analysis is based on a single term. This means that the Monte Carlo analysis is based on Eq. (5.2) if an energy bundle in element ABCD starts from either side AB or DC. Otherwise, the Monte Carlo analysis is from another term.

The Monte Carlo formulations presented here are developed on the basis of Eq. (5.2). The simulation of an energy bundle includes the determination of wavenumber, and starting point and direction of emission of this energy bundle in the finite volume element. The statistical relationships for determining these parameters are obtained readily from Eq. (5.2) as [6, 54, 55]

$$R_{\omega} = \frac{\int_0^{\omega} \int_0^b \int_0^{\pi} \int_0^{2\pi} I_{b\omega} [1 - \tau_{\omega}(s \rightarrow s')] \cos \theta \sin \theta d\psi d\theta dx^* d\omega}{Q} \quad (5.4)$$

$$R_{x^*} = \frac{\int_0^{x^*} \int_0^{\infty} \int_0^{\pi} \int_0^{2\pi} I_{b\omega} [1 - \tau_{\omega}(s \rightarrow s')] \cos \theta \sin \theta d\psi d\theta d\omega dx^*}{Q} \quad (5.5)$$

$$R_\theta = \frac{\int_0^\theta \int_0^\infty \int_0^b \int_0^{2\pi} I_{b\omega} [1 - \tau_\omega(s \rightarrow s')] \cos \theta \sin \theta d\psi dx^* d\omega d\theta}{Q} \quad (5.6)$$

$$R_\psi = \frac{\int_0^\psi \int_0^\infty \int_0^b \int_0^\pi I_{b\omega} [1 - \tau_\omega(s \rightarrow s')] \cos \theta \sin \theta d\theta dx^* d\omega d\psi}{Q} \quad (5.7)$$

In Eqs. (5.2) and (5.4)-(5.7),  $\tau_\omega$  is a real spectral transmittance. Before solving these equations to obtain  $\omega$ ,  $x^*$ ,  $\theta$  and  $\psi$  from a set of given values of  $R_\omega, R_{x^*}, R_\theta, R_\psi$ , the narrow band model should be applied to approximate the real spectral transmittance.

Taking the spectral average over all narrow bands and using the narrow band approximation as in Eq. (3.10), Eqs. (5.2) and (5.4)-(5.7), are expressed as

$$Q = \sum_{k=1}^{m_\omega} \left\{ \int_0^b \int_0^\pi \int_0^{2\pi} \overline{I_{b\omega^k}} [1 - \overline{\tau_{\omega^k}}(s \rightarrow s')] \cos \theta \sin \theta d\psi d\theta dx^* \right\} \Delta\omega^k \quad (5.8)$$

$$R_\omega = \frac{\sum_{k=1}^n \left\{ \int_0^b \int_0^\pi \int_0^{2\pi} \overline{I_{b\omega^k}} [1 - \overline{\tau_{\omega^k}}(s \rightarrow s')] \cos \theta \sin \theta d\psi d\theta dx^* \right\} \Delta\omega^k}{Q}, \quad (\omega^{n-1} < \omega \leq \omega^n) \quad (5.9)$$

$$R_{x^*} = \frac{\sum_{k=1}^{m_\omega} \left\{ \int_0^{x^*} \int_0^\pi \int_0^{2\pi} \overline{I_{b\omega^k}} [1 - \overline{\tau_{\omega^k}}(s \rightarrow s')] \cos \theta \sin \theta d\psi d\theta dx^* \right\} \Delta\omega^k}{Q} \quad (5.10)$$

$$R_\theta = \frac{\sum_{k=1}^{m_\omega} \left\{ \int_0^\theta \int_0^b \int_0^{2\pi} \overline{I_{b\omega^k}} [1 - \overline{\tau_{\omega^k}}(s \rightarrow s')] \cos \theta \sin \theta d\psi dx^* d\theta \right\} \Delta\omega^k}{Q} \quad (5.11)$$

$$R_\psi = \frac{\sum_{k=1}^{m_\omega} \left\{ \int_0^\psi \int_0^b \int_0^\pi \overline{I_{b\omega^k}} [1 - \overline{\tau_{\omega^k}}(s \rightarrow s')] \cos \theta \sin \theta d\theta dx^* d\psi \right\} \Delta\omega^k}{Q} \quad (5.12)$$

Similar to the one-dimensional problem analyzed in Chap. 3, in order to solve Eqs. (5.8)-(5.12) for a set of given values of  $R_\omega, R_{x^*}, R_\theta$  and  $R_\psi$ , interpolation and approximation methods must be employed.



Knowing wavenumber, emission point and travelling direction of an energy bundle, the next question is where the energy bundle is absorbed. Let us still consider the emitted radiant energy along a pencil of column  $s \rightarrow s'$  (Fig. 5.1). After this amount of energy is transmitted over a column  $s' \rightarrow s''$ , the remaining radiant energy is given by

$$dQ' = I_{b\omega} [1 - \tau_\omega(s \rightarrow s')] \tau_\omega(s' \rightarrow s'') \cos \theta d\Omega dx^* d\omega \quad (5.13)$$

where  $\tau_\omega(s' \rightarrow s'')$  is the spectral transmittance over the path  $s' \rightarrow s''$ . Taking a narrow band average of Eqs. (5.1) and (5.13) and dividing the latter by the first, the statistical relationship for determining the location of absorption can be expressed as

$$\begin{aligned} R_l &= \frac{[1 - \tau_\omega(s \rightarrow s')] \tau_\omega(s' \rightarrow s'')}{1 - \overline{\tau_\omega}(s \rightarrow s')} \\ &= \frac{\overline{\tau_\omega}(s' \rightarrow s'') - \tau_\omega(s \rightarrow s') \tau_\omega(s' \rightarrow s'')}{1 - \overline{\tau_\omega}(s \rightarrow s')} \end{aligned} \quad (5.14)$$

Similar to Chap. 3, the averaged product  $\overline{\tau_\omega(s \rightarrow s') \tau_\omega(s' \rightarrow s'')}$  can be treated in a spectrally correlated or non-correlated manner. The first choice results in the spectrally correlated formulation as

$$R_l = \frac{\overline{\tau_\omega}(s' \rightarrow s'') - \overline{\tau_\omega}(s \rightarrow s'')}{1 - \overline{\tau_\omega}(s \rightarrow s')} \quad (5.15)$$

and the latter choice results in the spectrally non-correlated formulation as

$$R_l = \overline{\tau_\omega}(s' \rightarrow s'') \quad (5.16)$$

Therefore, it is seen that exact correlated and non-correlated Monte Carlo formulations differ only in the relation for  $R_l$  as given in Eqs. (5.15) and (5.16).

Comparing each formulation in this chapter with the corresponding one-dimensional formulations developed in Chap. 3, it is found that the exact correlated and non-correlated statistical relationships for  $R_l$  are the same but statistical relationships for  $R_\omega$ ,  $R_{x^*}$ ,  $R_\theta$ ,  $R_\psi$  are different. This phenomenon is true for any two different problems.

### 5.3 Approximate Correlated and Non-correlated Monte Carlo Formulations

In the exact analysis, the Monte Carlo formulations need to be developed from each independent term in the expressions for the total emitted radiant energy of a volume element. Numerical evaluations of Eqs. (5.8)-(5.12) for  $Q, R_\omega, R_{x^*}, R_\theta, R_\psi$  involve four-dimensional integrations and the integrands in these equations are complex functions of integration variables. Obviously, the Monte Carlo simulation is already complicated although the problem considered is a simple two-dimensional problem. The difficulty may continue to increase considerably if the complexity of the problem increases. To simplify complicated Monte Carlo formulations, it is assumed that the volume  $dV$  of a volume element is very small so that the energy emitted within  $dV$  escapes before reabsorption. This assumption has been used widely in many studies to simplify radiation analysis. The total emitted radiative energy and the statistical relationships for determining the wavenumber and emission direction of an energy bundle from a finite volume  $dV$  are given by [6, 54, 55]

$$Q_{dV} = 4\pi \int_0^\infty \kappa_\omega I_{b\omega} dV d\omega \quad (5.17)$$

$$R_\omega = \frac{\int_0^\omega \kappa_\omega I_{b\omega} d\omega}{\int_0^\infty \kappa_\omega I_{b\omega} d\omega} \quad (5.18)$$

$$R_\theta = \frac{1 - \cos \theta}{2} \quad (5.19)$$

$$R_\psi = \frac{\psi}{2\pi} \quad (5.20)$$

The emission point of an energy bundle from a volume element is assumed to be the center point of the element. This assumption is justifiable in an infinitesimal volume element. Introducing the narrow band approximation, Eqs. (5.17) and (5.18) become

$$Q_{dV} = 4\pi \sum_{k=1}^{m_\omega} \left( \overline{\kappa_{\omega^k}} \overline{I_{b\omega^k}} \Delta\omega^k \right) dV \quad (5.21)$$

$$R_\omega = \frac{4\pi \sum_{k=1}^n (\overline{\kappa_{\omega^k}} \overline{I_{b\omega^k}} \Delta\omega^k) dV}{Q_{dV}}, \quad (\omega^{n-1} < \omega \leq \omega^n) \quad (5.22)$$

Here,  $\overline{\kappa_{\omega^k}}$  is the mean absorption coefficient over a narrow band and is obtained as [29]

$$\overline{\kappa_{\omega^k}} \approx -\frac{\ln \overline{\tau_{\omega^k}}(L_m)}{L_m} \quad (5.23)$$

where  $L_m$  is the mean beam length of the volume element. It is evident that Eqs. (5.19)-(5.22) are much simpler than the corresponding equations for the exact treatment of the Monte Carlo simulation. These simple formulations do not change with the complexity of the problem.

The statistical relationship presented here for determining the location of absorption of an energy bundle emitted from the volume element  $dV$  is different from that available in literature [6, 54, 55]. This is because a narrow band model is incorporated in the present formulation. Equation (5.15) is the general formulation to calculate  $R_l$  with consideration of the spectral correlation. Substituting the mean transmittance with the mean absorption coefficients in the denominator of Eq. (5.15), yields

$$R_l = \frac{\overline{\tau_\omega}(s' \rightarrow s'') - \overline{\tau_\omega}(s \rightarrow s'')}{1 - \exp\left(-\int_s^{s'} \overline{\kappa_\omega} ds^*\right)} \quad (5.24)$$

Since  $dV$  is very small, the following approximation can be invoked

$$1 - \exp\left(-\int_s^{s'} \overline{\kappa_\omega} ds^*\right) \approx \overline{\kappa_\omega} ss' \quad (5.25)$$

This approximation is also applied in deriving Eqs. (5.17)-(5.20). Consequently, Eq. (5.24) is simplified as

$$\begin{aligned} R_l &\approx \frac{\overline{\tau_\omega}(s' \rightarrow s'') - \overline{\tau_\omega}(s \rightarrow s'')}{\overline{\kappa_\omega} ss'} \\ &\approx \frac{1}{\overline{\kappa_\omega}} \lim_{ss' \rightarrow 0} \frac{\overline{\tau_\omega}(s' \rightarrow s'') - \overline{\tau_\omega}(s \rightarrow s'')}{ss'} \\ &\approx -\frac{1}{\overline{\kappa_\omega}} \left( \frac{\partial \overline{\tau_\omega}(s \rightarrow s'')}{\partial s} \right) \\ &\approx \frac{L_m}{\ln \overline{\tau_\omega}(L_m)} \left( \frac{\partial \overline{\tau_\omega}(s \rightarrow s'')}{\partial s} \right) \end{aligned} \quad (5.26)$$

Equation (5.26) is the approximate correlated statistical relationship for determining the location of absorption and it is different from the corresponding exact correlated formulation as given in Eq. (5.15). The approximate non-correlated statistical relationship for determining the location of absorption cannot be simplified further and it is the same as given by Eq. (5.16). Therefore, similar to the exact correlated and non-correlated formulations, the approximate correlated and non-correlated formulations differ only in the expression for  $R_1$ .

#### 5.4 Results and Discussion

In order to validate the approximate Monte Carlo analyses and to investigate the effects of spectral correlation, two problems have been selected by referring to the work of Zhang et al. [28]. The results for the net radiative wall flux and the radiative source term have been obtained for four different formulations which correspond to the exact correlated solution, approximate correlated solution, exact non-correlated solution and approximate non-correlated solution. In the problems considered, the length and height of two parallel plates are  $L=1.2$  m and  $H=0.6$  m, respectively. The two wall emissivities are chosen to be the same and equal to 0.8. The total pressure of the gas is taken to be 1 atm. One of the problems considered is an isothermal and homogeneous  $H_2O-N_2$  mixture in which the mole fractions are:  $X_{H_2O}=0.6$  and  $X_{N_2}=0.4$ ; the gas temperature is 1500 K; and the real and pseudo walls are held at 300 K. The other problem considered is a nonisothermal and inhomogeneous  $H_2O-O_2-N_2$  mixture in which the mole fraction distributions are given by

$$\begin{aligned} X_{H_2O} &= 0.3 \left[ 1 - 2 \left( \frac{x}{L} - 0.5 \right)^2 \right] \left[ 2 - \frac{|2y - H|}{H} \right] \\ X_{O_2} &= 0.1 \left[ 1 - 3 \left( \frac{x}{L} - 0.5 \right)^2 \right] \left[ 2.5 - \frac{|2y - H|}{H} \right] \end{aligned} \quad (5.27)$$

$$X_{N_2} = 1 - x_{H_2O} - x_{O_2}$$

and the gas temperature distribution is assumed to be

$$T(x, y) = 1000 + 1200 \left[ 1 - \frac{|2y - H|}{H} \right] \frac{x}{L} \quad (5.28)$$

The two real walls and the inlet pseudo wall are kept at a temperature of 1000 K. The outlet of the gas is open to a 300 K atmosphere, so the temperature of the outlet pseudo wall is 300 K. For both problems, only  $\text{H}_2\text{O}$  is considered to be a radiatively participating species. There are five important absorption bands for  $\text{H}_2\text{O}$ . All of these bands have been taken into account in this study and they consist of  $m_\omega=295$  narrow bands in the range from  $150 \text{ cm}^{-1}$  to  $7500 \text{ cm}^{-1}$ .

To assure that the statistical results make sense in the Monte Carlo simulation, two requirements must be met. One is the accuracy of the statistical results for a given grid. The other is the independence of the results from the grid. In this study, the designated statistical accuracy of the results is defined in such a way that when the relative statistical errors are less than  $\pm 5\%$ , the probability of the results lying within these limits is greater than 95%. Independence of the results on a grid is considered to have been achieved when the medium is divided into  $20 \times 20$  uniform finite volume elements for the problems considered. For this grid, the total number of energy bundles had to be 2,000,000 in order to meet the designated statistical accuracy requirement. All calculations have been carried out on a Sun Sparc Workstation. The CPU times required for different solutions for two different problems are listed in Table 5.1. It should be noted that the present computer code was written for problems involving nonisothermal and inhomogeneous mixtures. No efforts have been made to simplify the problem for an isothermal and homogeneous mixture specifically. For integrations and interpolations in the exact Monte Carlo formulations, Eqs. (5.8)-(5.12), the divisions of the side length, polar angle and azimuthal angle (within half of their ranges in a rectangular volume element) were chosen to be  $m_x=10$ ,  $m_\theta=10$  and  $m_\psi=10$ , respectively. The emitted radiative energy from each of the  $m_\omega \times m_x \times m_\theta \times m_\psi = 295 \times 10 \times 10 \times 10$  medium columns was then calculated and stored. The required integrations and interpolations were implemented from the summation of the values of radiative energy in different columns. These computations were done for each volume element. Obviously, this procedure is

Table 5.1 CPU time (minutes) required for different solutions

	Exact correlated	Approximate correlated	Exact non-correlated	Approximate non-correlated
Isothermal and homogeneous mixture	265	112	325	170
Nonisothermal and inhomogeneous mixture	269	167	378	225

very time consuming. This is the major reason why the CPU time for exact solutions is much larger than that for approximate solutions in Table 5.1. It should also be noted that determination of the absorption location of an energy bundle, by using Eq. (5.15) and Eq. (5.26), takes about the same amount of time.

The problem with an isothermal and homogeneous mixture is considered first. The behavior of four different solutions is illustrated in Figs. 5.3–5.5. Figures 5.3 and 5.4 show radiative source distributions at locations equal to  $x/L=0.225$  and  $x/L=0.5$  on the plates, respectively. The approximate correlated results agree with the exact correlated results and the approximate non-correlated results agree with the exact non-correlated results. As the distance from the walls increases, all four solutions predict the same trend in the radiative source results. The two non-correlated solutions are far below the two correlated solutions.

The distribution of radiative wall heat flux along the plates is presented in Fig. 5.5. The approximate correlated solution is found to be almost the same as the exact correlated solution and the approximate non-correlated solution is seen to be slightly higher than the exact non-correlated solution. The difference between the correlated and non-correlated results is seen to be significant. For the most part, the two non-correlated solutions are approximately two times higher than the two correlated solutions.

The results for a nonisothermal and inhomogeneous mixture are illustrated in Figs. 5.6–5.9. The  $H_2O$  mole fraction calculated from Eq. (5.27) has a maximum value at the mid plane of the geometry considered, and decreases gradually away from the center point. The temperature in the medium, calculated from Eq. (5.28), increases away from the walls and the inlet. Figures 5.6–5.8 show the radiative source distributions at locations equal to  $x/L=0.275$ ,  $0.5$ , and  $0.825$  along the plates, respectively. As the distance from the inlet location increases, the temperature change becomes more steep and temperatures in the central region are high. Thus, the change in radiative source results is becoming abruptly as seen from Figs. 5.6–5.8. In all three figures, it is

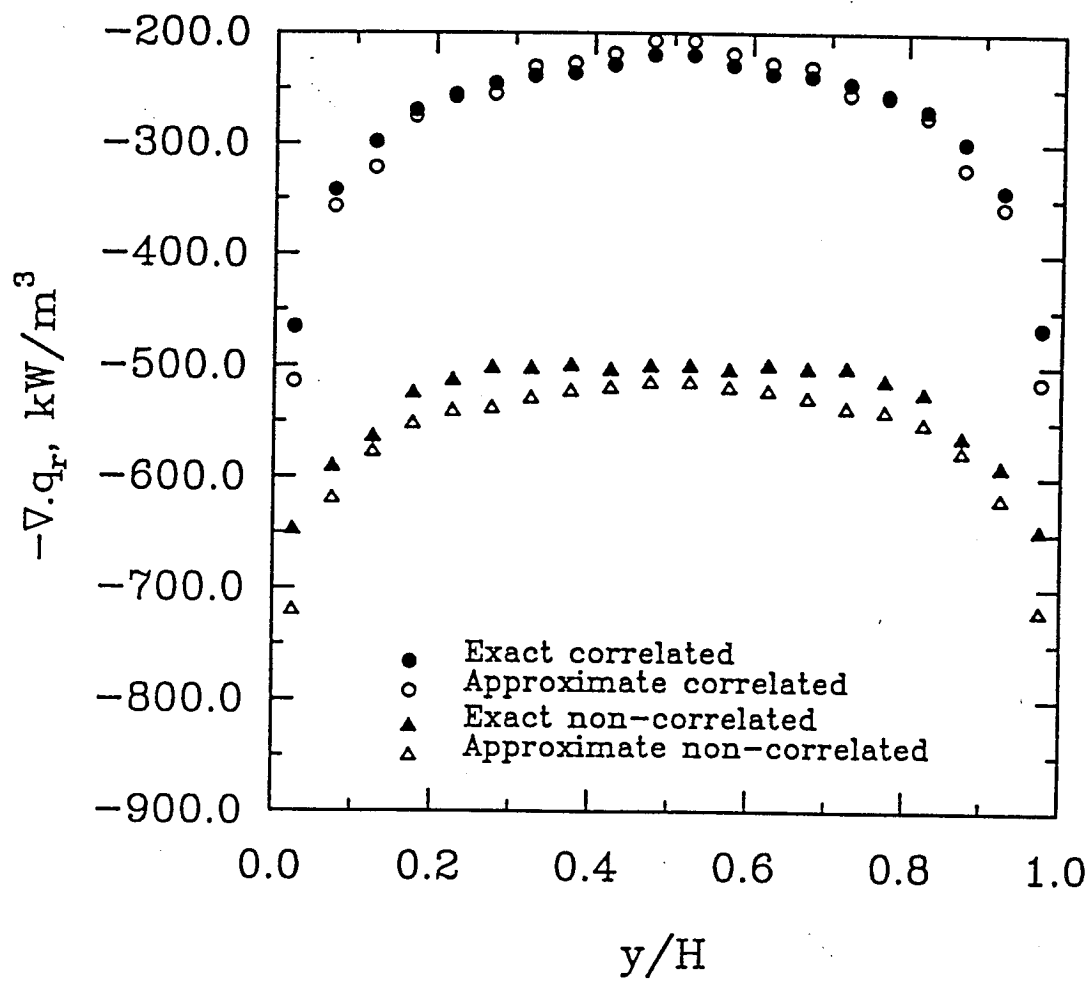


Fig. 5.3 Radiative source distribution at the location  $x/L=0.225$  for isothermal and homogeneous  $\text{H}_2\text{O}-\text{N}_2$  mixture.



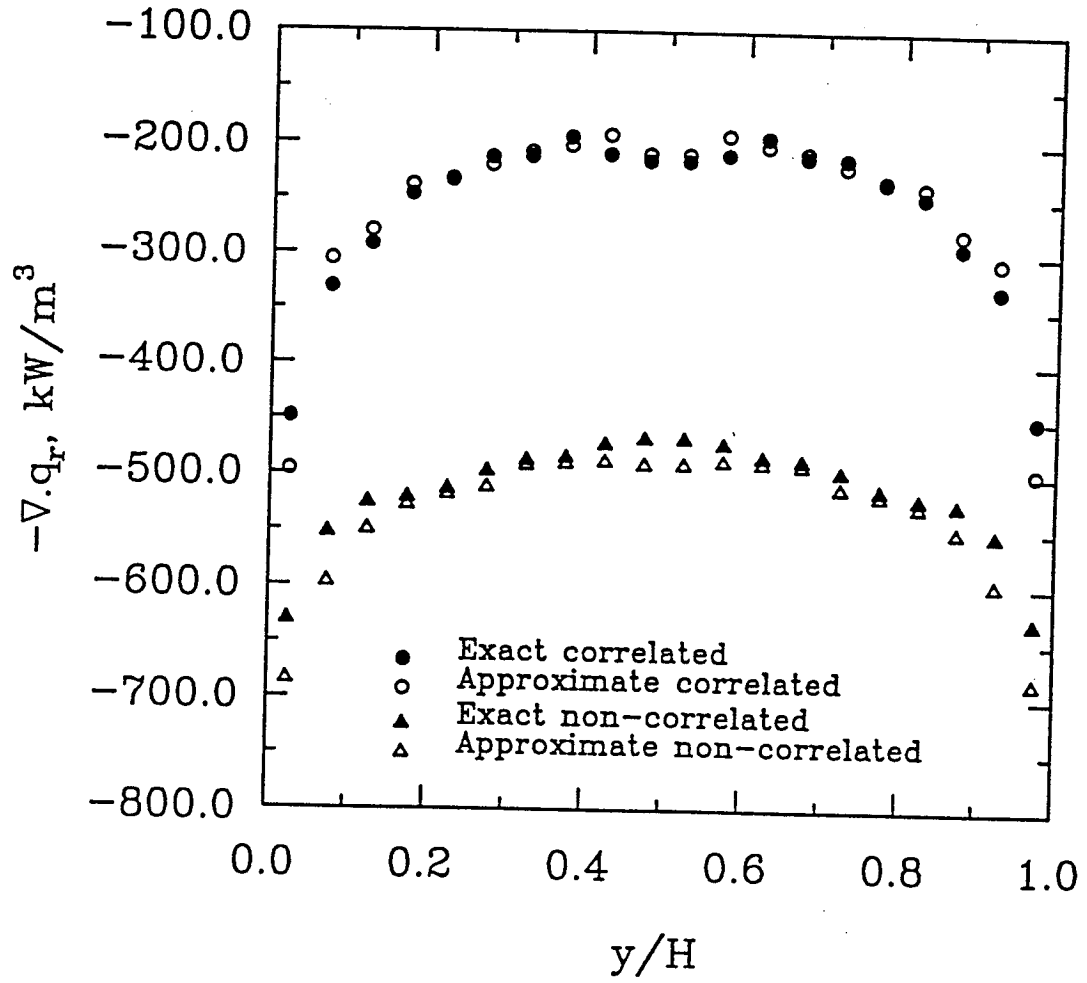


Fig. 5.4 Radiative source distribution at the location  $x/L=0.5$  for isothermal and homogeneous  $\text{H}_2\text{O}-\text{N}_2$  mixture.

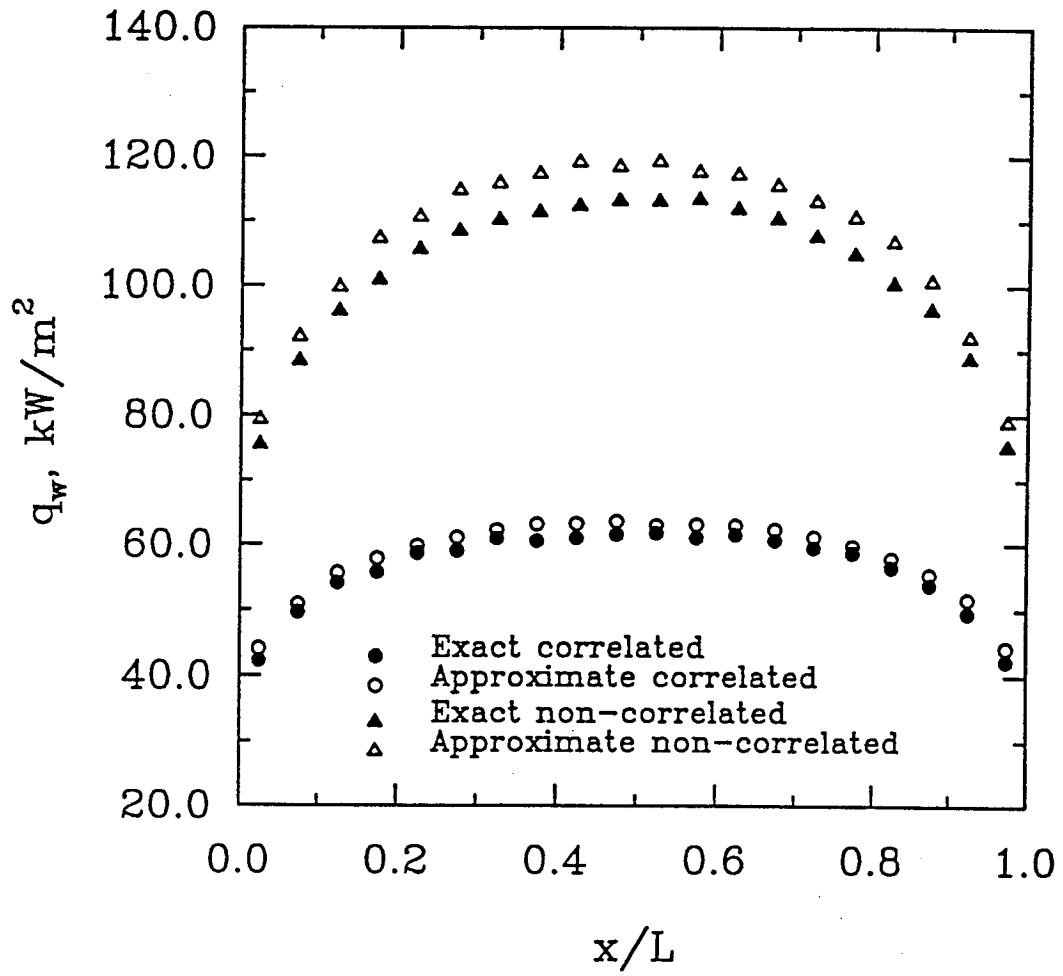


Fig. 5.5 Radiative wall flux distribution for isothermal and homogeneous  $\text{H}_2\text{O-N}_2$  mixture.

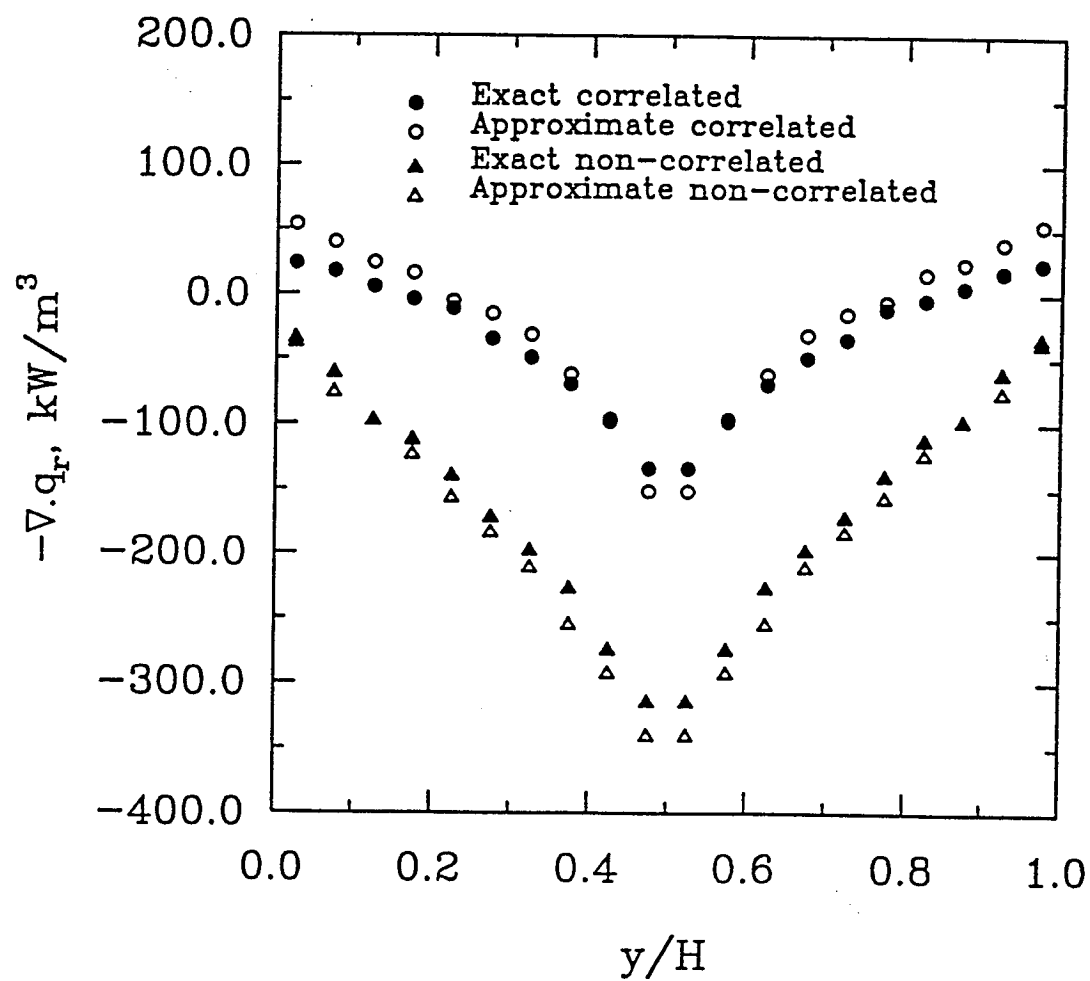


Fig. 5.6 Radiative source distribution at the location  $x/L=0.275$  for nonisothermal and inhomogeneous  $\text{H}_2\text{O}-\text{O}_2-\text{N}_2$  mixture.

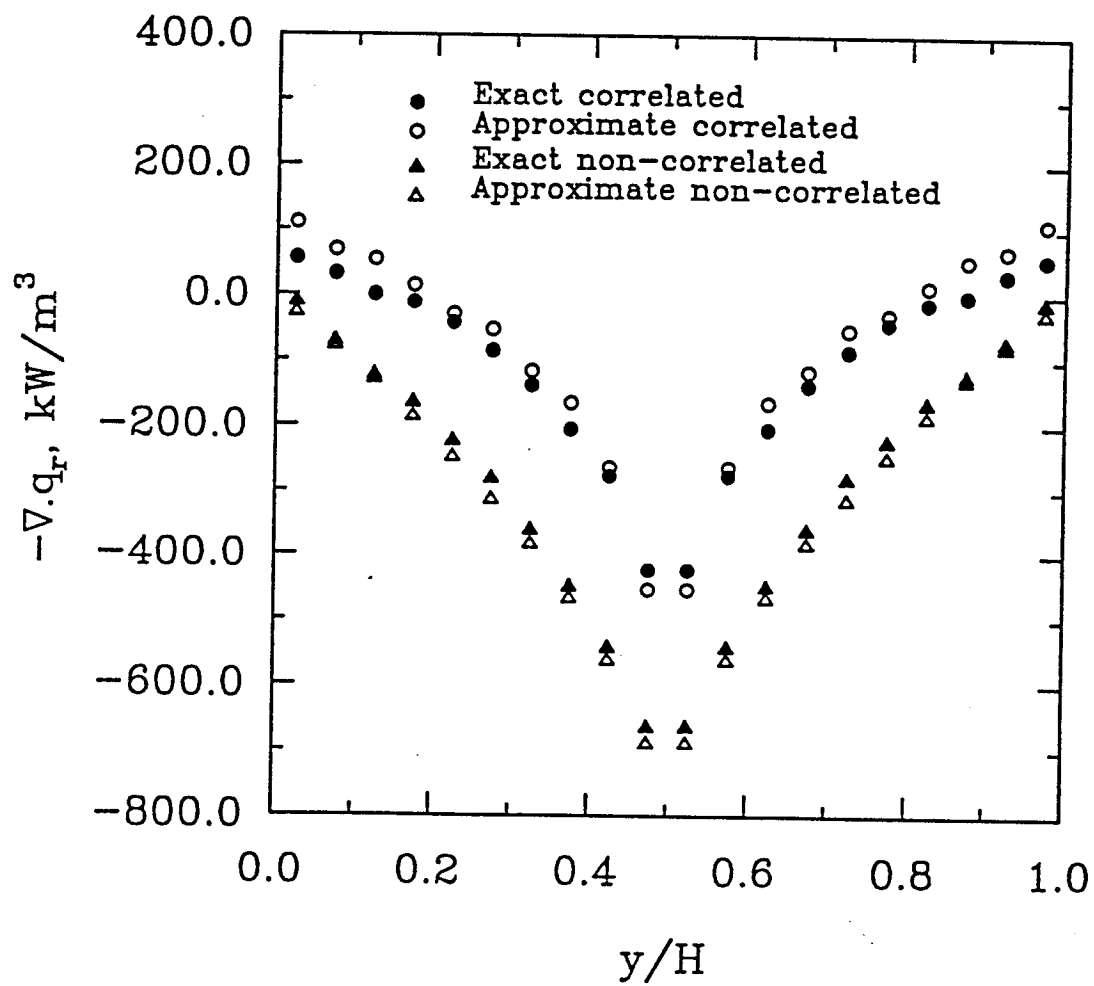


Fig. 5.7 Radiative source distribution at the location  $x/L=0.5$  for nonisothermal and inhomogeneous  $\text{H}_2\text{O}-\text{O}_2-\text{N}_2$  mixture.

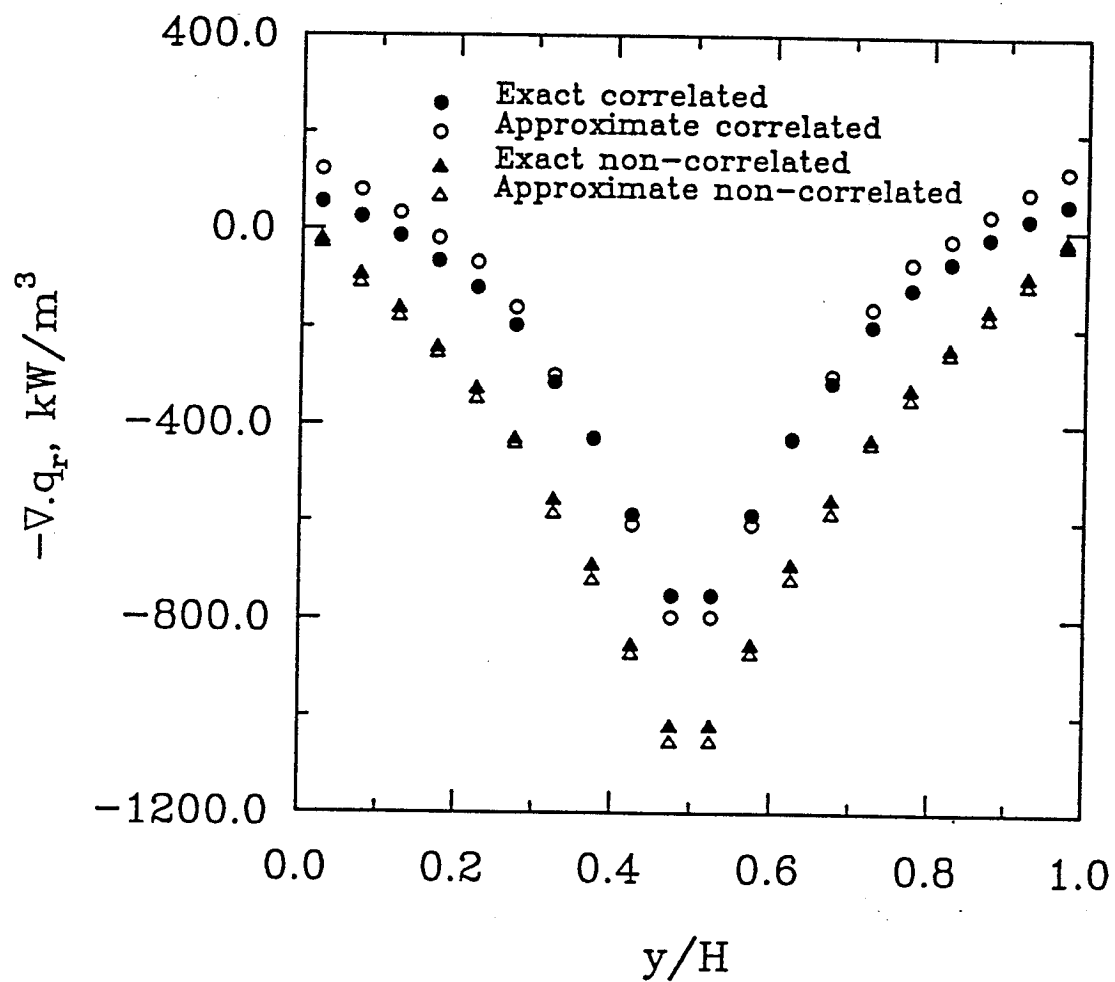


Fig. 5.8 Radiative source distribution at the location  $x/L=0.825$   
for nonisothermal and inhomogeneous  $\text{H}_2\text{O}-\text{O}_2-\text{N}_2$  mixture.

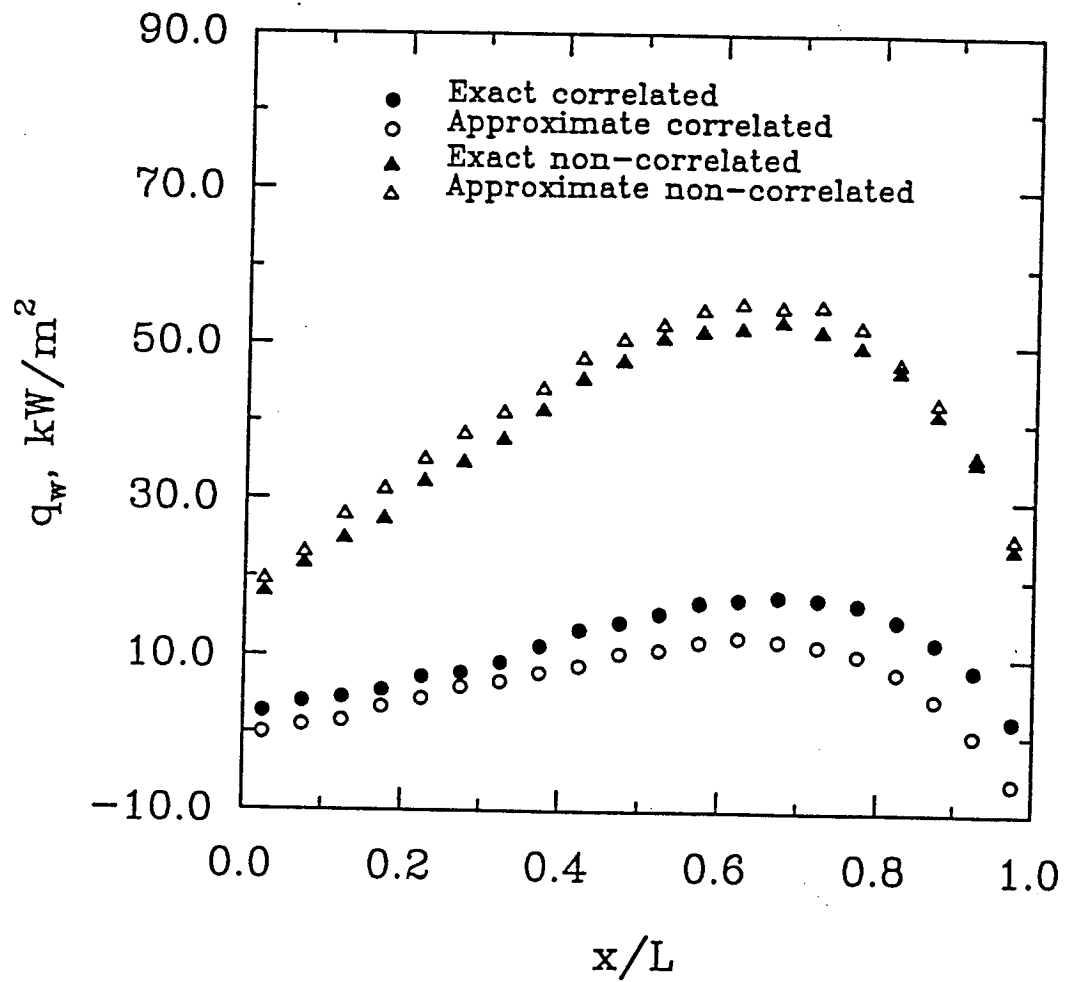


Fig. 5.9 Radiative wall flux distribution for nonisothermal and inhomogeneous  $\text{H}_2\text{O}-\text{O}_2-\text{N}_2$  mixture.

evident that the approximate correlated solution is in good agreement with the exact correlated solution and the approximate non-correlated solution approximates the exact non-correlated solution. The approximate correlated solution appears to be slightly higher in the wall region and lower in the central region than the exact correlated solution. The difference between the correlated and non-correlated solutions is significant as in the first problem. From the correlated solutions, it is evident that the gas goes from a net absorber near the walls to a net emitter away from the walls. On the other hand, the non-correlated solutions predict that the gas is a net emitter in nearly all regions.

Figure 5.9 illustrates the distribution of radiative wall flux along the plates. The radiative wall flux is seen to increase at first, reach a peak value near the outlet, and then decrease. Such behavior is due to the fact that, for the problem considered, the outlet region is equivalent to a cold sink. This cold sink has a strong effect on the radiative heat transfer in the adjacent region. Among the four different solutions, the approximate correlated solution is slightly lower than the exact correlated solution and the approximate non-correlated solution is slightly higher than the exact non-correlated solution. A comparison of different solutions reveals that the non-correlated formulations predict much higher radiative energy absorption on the walls than the correlated formulations. The difference in results can be reach as high as one order of magnitude at some locations.

From the results presented, it is evident that approximate formulations can provide results very close to those from the corresponding exact formulations. The non-correlated formulations, however, predict much lower radiative source distributions in the medium and much higher radiative wall fluxes along the plates than the correlated formulations. The reason for this difference is the same as that for one-dimensional problem. That is, the  $R_1$  calculated from the non-correlated formulation, Eq. (5.16), is greater than that from the correlated formulations, Eqs. (5.15) and (5.26). Therefore, for the non-correlated formulation, an energy bundle travels a long distance and is likely to be absorbed on the wall. This also explains why the CPU time required for the non-correlated solution is

larger than that required for the corresponding correlated solution (Table 5.1). Because of significant differences between the correlated and non-correlated solutions, the same conclusion as that in Chap. 3 is drawn that the non-correlated formulations are not useful.



## Chapter 6

### RADIATIVE INTERACTIONS IN CHEMICALLY REACTING COMPRESSIBLE FLOWS

In Chap. 5, an accurate radiation transport model using the approximate Monte Carlo correlated formulations, has been developed and validated. The formulations in this model are simple and can be applied easily in nongray and multi-dimensional systems. The objective of this chapter is to apply the approximate Monte Carlo correlated formulations to investigate the radiative interactions in multi-dimensional chemically reacting flows. The basic formulations are provided in Sec. 6.1. The method of solution is presented in Sec. 6.2, and the results and discussion are contained in Sec. 6.3.

#### 6.1 Basic Formulations

##### 6.1.1 Physical Model

As mentioned in the introduction, there has been extensive research directed toward the development of scramjet propulsion systems. To investigate the radiative effects on these systems, a specific physical model will be considered in this study which is a supersonic flow of premixed hydrogen and air in an expanding nozzle (Fig. 6.1). The nozzle wall is modeled, as noted, by a shifted sinusoidal curve. The inlet temperatures of hydrogen and air are considerably high so that chemical reactions take place in the entire flowfield. The products of hydrogen-air combustion include water vapor and hydroxyl radicals. These species are highly absorbing and emitting. To simulate the flowfield accurately, all important phenomena such as chemistry, radiation and turbulence should be taken into account and the fully elliptic form of the governing equations must be used.

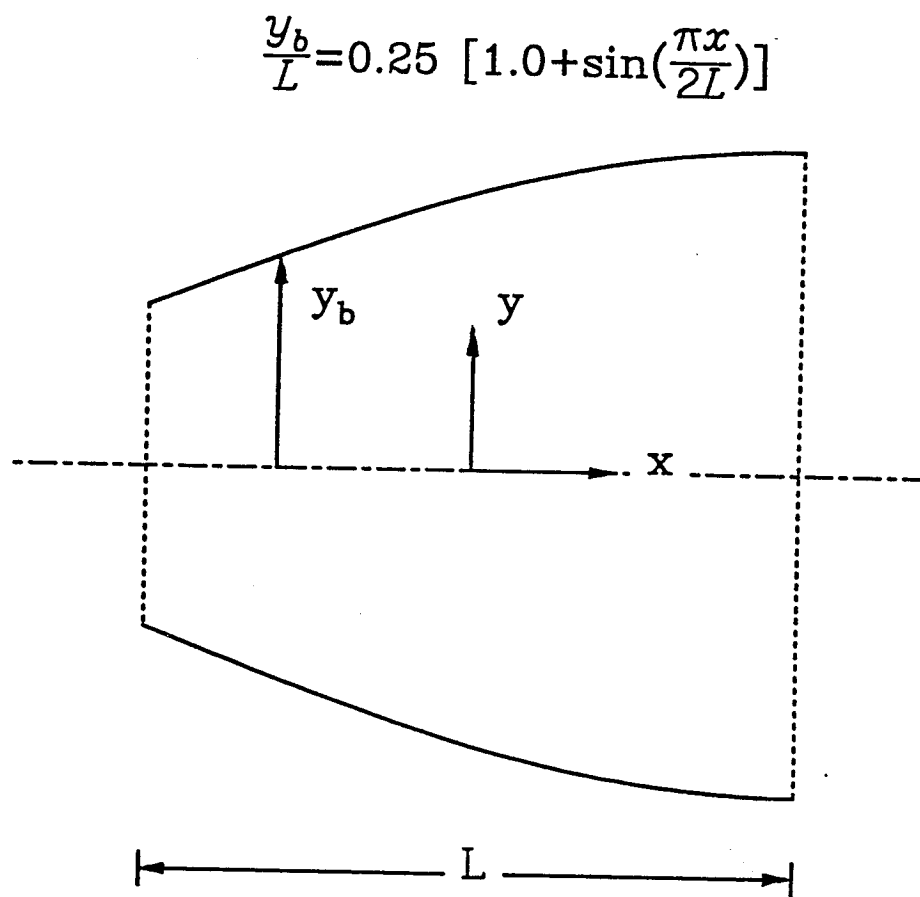


Fig. 6.1 Schematic diagram of nozzle.

### 6.1.2 Governing Equations

In this study, the two-dimensional nozzle flow considered is described by the Navier-Stokes and species continuity equations which can be represented in the physical coordinates as

$$\frac{\partial U}{\partial t} + \frac{\partial F}{\partial x} + \frac{\partial G}{\partial y} = H \quad (6.1)$$

where vectors U, F, G and H are given by

$$U = \begin{bmatrix} \rho \\ \rho u \\ \rho v \\ \rho E \\ \rho f_j \end{bmatrix} \quad (6.2)$$

$$F = \begin{bmatrix} \rho u \\ \rho u^2 - \sigma_x \\ \rho uv - \tau_{yx} \\ (\rho E - \sigma_x)u - \tau_{xy}v + q_x \\ \rho f_i(u + \tilde{u}_i) \end{bmatrix} \quad (6.3)$$

$$G = \begin{bmatrix} \rho v \\ \rho uv - \tau_{xy} \\ \rho v^2 - \sigma_y \\ (\rho E - \sigma_y)v - \tau_{yx}u + q_y \\ \rho f_i(v + \tilde{v}_i) \end{bmatrix} \quad (6.4)$$

$$H = \begin{bmatrix} 0 \\ 0 \\ 0 \\ -\nabla \cdot q_r \\ \dot{w}_i \end{bmatrix} \quad (6.5)$$

The other terms appearing in vectors F, G, and H are defined as

$$\sigma_x = -p + \lambda \left( \frac{\partial u}{\partial x} + \frac{\partial v}{\partial y} \right) + 2\mu \frac{\partial u}{\partial x} \quad (6.6)$$

$$\sigma_y = -p + \lambda \left( \frac{\partial u}{\partial x} + \frac{\partial v}{\partial y} \right) + 2\mu \frac{\partial v}{\partial y} \quad (6.7)$$

$$\tau_{xy} = \tau_{yx} = \mu \left( \frac{\partial u}{\partial x} + \frac{\partial v}{\partial y} \right) \quad (6.8)$$

$$q_x = -k \frac{\partial T}{\partial x} + \rho \sum_{i=1}^{N_s} h_i f_i \tilde{u}_i \quad (6.9)$$

$$q_y = -k \frac{\partial T}{\partial y} + \rho \sum_{i=1}^{N_s} h_i f_i \tilde{v}_i \quad (6.10)$$

$$E = -\frac{p}{\rho} + \frac{u^2 + v^2}{2} + \sum_{i=1}^{N_s} h_i f_i \quad (6.11)$$

$$h_i = h_i^R + \int_{T_R}^T C_{p,i} dT \quad (6.12)$$

$$p = \rho R_u T \sum_{i=1}^{N_s} \frac{f_i}{M_i} \quad (6.13)$$

where  $\lambda = -\frac{2}{3}\mu$ .

In Eqs. (6.1), only  $(N_s-1)$  species equations need to be considered since the mass fraction of the species is prescribed by satisfying the constraint equation

$$\sum_{i=1}^{N_s} f_i = 1 \quad (6.14)$$

The diffusion velocity of the  $i$ th species is obtained by solving the Stefan-Maxwell equation [70], neglecting the body force and thermal diffusion effects, as

$$\nabla X_i = \sum_{j=1}^{N_s} \left( \frac{X_i X_j}{D_{ij}} \right) (\tilde{V}_j - \tilde{V}_i) + (f_i - X_i) \left( \frac{\nabla p}{p} \right) \quad (6.15)$$

The preceding equation is also applied only to  $(N_s-1)$  species. The diffusion velocity for the remaining species is prescribed by satisfying the constraint equation  $\sum_{i=1}^{N_s} f_i \tilde{V}_i = 0$ , which ensures the consistency.

### 6.1.3 Thermodynamic Model

To calculate the required thermodynamic quantities, the specific heat for each species  $C_{p_i}$  is first defined by a fourth-order polynomial in temperature,

$$\frac{C_{p_i}}{R} = A_i + B_i T + C_i T^2 + D_i T^3 + E_i T^4 \quad (6.16)$$

The values of the coefficients appearing in the equation are found in Ref. 71. Knowing the specific heat of each species, the enthalpy of each species can be found from Eq. (6.12) and the total internal energy is computed from Eq. (6.11).

### 6.1.4 Chemistry Model

Chemical reaction rate expressions are usually determined by summing the contributions from each relevant reaction path to obtain the total rate of change of each species. Each path is governed by a law of mass action expression in which the rate constants can be determined from a temperature dependent Arrhenius expression. In vector  $H$ , the term  $\dot{w}_i = M_i C_i$  represents the net rate of production of species  $i$  in all chemical reactions and is modelled as:

$$\sum_{i=1}^{N_s} \gamma'_{ij} C_j \xrightleftharpoons[k_{b_j}]{k_{f_j}} \sum_{i=1}^{N_s} \gamma''_{ij} C_j; \quad j = 1, \dots, N_r \quad (6.17)$$

$$\dot{w}_i = M_i C_i = M_i \sum_{j=1}^{N_r} (\gamma''_{ij} - \gamma'_{ij}) \left[ k_{f_j} \prod_{m=1}^{N_s} C_m^{\gamma'_{jm}} - k_{b_j} \prod_{m=1}^{N_s} C_m^{\gamma''_{jm}} \right] \quad (6.18)$$

Equation (6.17) represents an  $N_r$  step chemical reaction and Eq. (6.18) is the production rate for the  $i$ th species. The reaction constants  $k_{f_j}$  and  $k_{b_j}$  are calculated from the following equations:

$$k_{f_j} = A_j T^{N_j} \exp\left(-\frac{E_j}{R_u T}\right); \quad j = 1, \dots, N_r \quad (6.19)$$

$$k_{b,j} = k_{f,j}/k_{eq,j}; \quad j = 1, \dots, N_r \quad (6.20)$$

The equilibrium constants appearing in Eq. (6.20) are given by

$$k_{eq,j} = \left( \frac{1}{R_u T} \right)^{\Delta n_j} \exp \left( \frac{-\Delta G_{R_j}}{R_u T} \right); \quad j = 1, \dots, N_r \quad (6.21)$$

where

$$\Delta n_j = \sum_{i=1}^{N_s} \gamma''_{ij} - \sum_{i=1}^{N_s} \gamma'_{ij}; \quad j = 1, \dots, N_r \quad (6.22)$$

$$\Delta G_{R_j} = \sum_{i=1}^{N_s} \gamma''_{ij} g_i - \sum_{i=1}^{N_s} \gamma'_{ij} g_i; \quad j = 1, \dots, N_r \quad (6.23)$$

$$\begin{aligned} \frac{g_i}{R_i} = & A_i(T - \ln T) - \frac{B_i}{2}T^2 - \frac{C_i}{6}T^3 - \frac{D_i}{12}T^4 \\ & - \frac{E_i}{20}T^5 + F_i - G_i T; \quad i = 1, \dots, N_r \end{aligned} \quad (6.24)$$

The forward rate for each reaction is determined from Eq. (6.19). The hydrogen-air combustion mechanism used in this work is from Ref. 3, but only seven species and seven reactions were selected for this study. The constants  $A_j$ ,  $N_j$  and  $E_j$  for these reactions are listed in Table 6.1. The species Gibb's free energy expression Eq. (6.24) is obtained from the integrations of the specific heat  $C_{p,i}$  and the coefficients in Eq. (6.24) are obtained in the same way as in Eq. (6.16).

### 6.1.5 Diffusion Models

The viscosity, thermal conductivity, and diffusion coefficient consist of the contributions from both fluid molecules and turbulent flow and they are expressed as

$$\begin{aligned} \mu &= \mu_l + \mu_t \\ k &= k_l + k_t \\ D_{ij} &= D_{ij}^l + D_{ij}^t \end{aligned} \quad (6.25)$$

Table 6.1 Hydrogen-Air Combustion Mechanism (7 species, 7 reactions)

No.	Reaction	A	N	E
1	$\text{H}_2 + \text{O}_2 \rightarrow \text{OH} + \text{OH}$	1.70E+13	0.0	24233
2	$\text{H} + \text{O}_2 \rightarrow \text{OH} + \text{O}$	1.42E+14	0.0	8250
3	$\text{OH} + \text{H}_2 \rightarrow \text{H}_2\text{O} + \text{H}$	3.16E+07	1.8	1525
4	$\text{O} + \text{H}_2 \rightarrow \text{OH} + \text{H}$	2.07E+14	0.0	6920
5	$\text{OH} + \text{OH} \rightarrow \text{H}_2\text{O} + \text{O}$	5.50E+13	0.0	3523
6	$\text{H} + \text{OH} + \text{M} \rightarrow \text{H}_2\text{O} + \text{M}$	2.21E+22	-2.0	0
7	$\text{H} + \text{H} + \text{M} \rightarrow \text{H}_2 + \text{M}$	6.53E+17	-1.0	0

where  $\mu_l$ ,  $k_l$ ,  $D_{ij}^l$  represent the molecular mixture viscosity, thermal conductivity, and diffusion coefficient, respectively;  $\mu_t$ ,  $k_t$ ,  $D_{ij}^t$  represent the turbulent viscosity, thermal conductivity, and diffusion coefficient, respectively.

The individual species molecular viscosities are computed from Sutherland's law

$$\frac{\mu_i}{\mu_{0i}} = \left( \frac{T}{T_{0i}} \right)^{3/2} \frac{T_{0i} + S_i}{T + S_i} \quad (6.26)$$

where  $\mu_{0i}$  and  $T_{0i}$  are reference values and  $S_0$  is the Sutherland constant. All three values are tabulated for the species in Refs. 72 and 73. Once the molecular viscosity of each species has been determined, the molecular mixture viscosity is determined from Wilke's law [74]

$$\mu_l = \sum_{i=1}^{N_s} \frac{\mu_i}{1 + \frac{1}{X_i} \sum_{j=1(j \neq i)}^{N_s} X_j \phi_{ij}} \quad (6.27)$$

where

$$\phi_{ij} = \frac{\left\{ 1 + [(\mu_i/\mu_j)(\rho_j/\rho_i)]^{1/2} (M_j/M_i)^{1/4} \right\}^2}{4\sqrt{2}[1 + (M_i/M_j)]^{1/2}} \quad (6.28)$$

The individual species thermal conductivities are also computed from Sutherland's law

$$\frac{k_i}{k_{0i}} = \left( \frac{T}{T'_{0i}} \right)^{3/2} \frac{T'_{0i} + S'_i}{T + S'_i} \quad (6.29)$$

but with different values of the reference values  $k_{0i}$  and  $T'_{0i}$  and the Sutherland's constant  $S'_i$ . These values are also taken from Refs. 72 and 73. The molecular mixture thermal conductivity is computed using conductivity values for the individual species and Wassilewa's formula [75],

$$k_l = \sum_{i=1}^{N_s} \frac{k_i}{1 + \frac{1}{X_i} \sum_{j=1(j \neq i)}^{N_s} X_j \phi'_{ij}} \quad (6.30)$$

where  $\phi'_{ij} = 1.075\phi_{ij}$  and  $\phi_{ij}$  is taken from Eq. (6.28).



For dilute gases, Chapman and Cowling [70] used kinetic theory to derive the following expression for the molecular binary diffusion coefficient  $D_{ij}$  between species  $i$  and  $j$ ,

$$D_{ij}^l = \frac{0.001858 T^{3/2} [(M_i + M_j)/M_i M_j]^{1/2}}{p \sigma_{ij}^2 \Omega_D} \quad (6.31)$$

Here, the diffusion collision integral  $\Omega_D$  is approximated by

$$\Omega_D = T^{*-0.145} + (T^* + 0.5)^{-2} \quad (6.32)$$

where  $T^* = T/T_{\varepsilon ij}$ . The values of the effective temperature  $T_{\varepsilon ij}$  and effective collision diameter  $\sigma_{ij}$  are taken to be averages of the separate molecular properties of each species, giving [70]

$$\sigma_{ij} = \frac{1}{2}(\sigma_i + \sigma_j) \quad (6.33)$$

and

$$T_{\varepsilon ij} = (T_{\varepsilon i} T_{\varepsilon j})^{1/2} \quad (6.34)$$

To evaluate the turbulent viscosity  $\mu_t$ , a turbulence model needs to be selected. An appropriate model selected in this study is the Baldwin-Lomax model. This model is very convenient to use and is also reliable for the flows like those considered here. The description of this model can be readily found in the literature [76–78]. Knowing turbulent viscosity  $\mu_t$ , the turbulent thermal conductivity  $k_t$  and turbulent diffusion coefficient  $D_{ij}^t$  are calculated from the turbulent Prandtl number and the turbulent Schmidt number, respectively.

#### **6.1.6 Radiative Transfer Model**

The radiative effects on the nozzle flowfield arise through the term  $-\nabla \cdot q_r$  in the energy equation and the radiative effects on the heat transfer on the nozzle walls arise

through the term  $q_{rw}$ . The exact expressions for both  $-\nabla \cdot q_r$  and  $q_{rw}$  are very complicated integro-differential equations and they are usually treated separately from the governing equations. Therefore, the term  $-\nabla \cdot q_r$  has been moved to the right hand side to be taken as the source term in the energy equation. As indicated earlier, the approximate Monte Carlo correlated formulations as seen in Eqs. (5.19)-(5.22) and (5.26) are employed to simulate the radiative heat transfer term. This treatment can provide a quantitative prediction of radiative interactions for the present problem.

## 6.2 Method of Solution

### 6.2.1 Grid Generation

Equation (6.1) is written in the physical domain  $(x, y)$  and must be transformed to an appropriate computational domain  $(\xi, \eta)$  for solution. An algebraic grid generation technique developed by Smith and Weigel [79] was used for grid generation in this study. From the computational point of view, it is desirable to have a uniform rectangular grid enclosed in a cube, where the exterior of the cube represents the physical boundaries. To have such grids, a body-fitted coordinate system was transformed linearly from the physical domain  $(x, y)$  to the computational domain  $(\xi, \eta)$  as follows:

$$\begin{aligned} x_1 &= x(\xi, 0) & \text{Lower} \\ y_1 &= y(\eta, 0) & \text{Boundary} \end{aligned} \tag{6.35}$$

$$\begin{aligned} x_2 &= x(\xi, 1) & \text{Upper} \\ y_2 &= y(\eta, 1) & \text{Boundary} \end{aligned} \tag{6.36}$$

$$\begin{aligned} x &= x(\xi, 1)\eta + x(\xi, 0)(1 - \eta) & \text{Between the} \\ y &= y(\xi, 1)\eta + y(\xi, 0)(1 - \eta) & \text{Boundaries} \end{aligned} \tag{6.37}$$

where  $0 \leq \xi \leq 1$ ;  $0 \leq \eta \leq 1$ . The grid should be concentrated in the regions of high gradients to predict the solutions accurately. Therefore, more grid points are required near the solid boundaries. The concentration of the grid in the  $\eta$ -direction can be accomplished by

$$\bar{\eta} = \frac{(\beta_y + 1) - (\beta_y - 1) \exp [-C(\eta - 1 + \alpha)/(1 - \alpha)]}{(2\alpha + 1)\{1 + \exp [C(\eta - 1 + \alpha)/(1 - \alpha)]\}} \quad (6.38)$$

where

$$C = \ln \left( \frac{\beta_y + 1}{\beta_y - 1} \right) \quad (6.39)$$

If  $\alpha$  is equal to zero ( $\alpha=0$ ), the compression takes place only near the lower wall ( $\eta=0$ ), and if  $\alpha$  is equal to one half ( $\alpha=1/2$ ), the compression takes place near both walls. The term  $\beta_y$  has a value between one to two, and as it gets closer to one, the grid becomes more concentrated near the walls. Employing this concentration, Eq. (6.37) is written in terms of  $\bar{\eta}$  as

$$\begin{aligned} x &= x(\xi, 1)\bar{\eta} + x(\xi, 0)(1 - \bar{\eta}) \\ y &= y(\xi, 1)\bar{\eta} + y(\xi, 0)(1 - \bar{\eta}) \end{aligned} \quad (6.40)$$

where  $0 \leq \bar{\eta} \leq 1$ .

Based on the above analysis, the grid mesh for the present problem is generated as seen in Fig. 6.2. Because the flow is assumed to be symmetric about the centerline of a two-dimensional nozzle, only the upper half of the nozzle is shown. It should be noted that the grid is concentrated in the normal direction in order to capture the boundary layer and the grid is kept uniform in the flow direction.

The above grid mesh was used for the flowfield simulation, but, the grid mesh for radiation simulation was quite different. A uniform grid mesh as seen in Fig. 6.3 was applied for radiation simulation for the present problem. Such a grid mesh is justifiable because radiation is a long-range phenomena and there is no need to use a concentrated grid mesh.

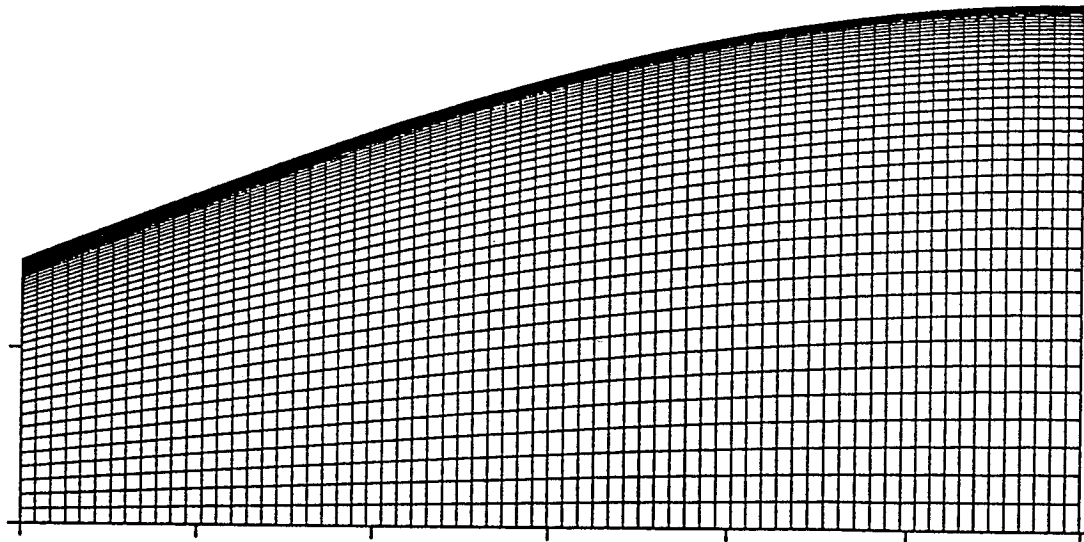


Fig. 6.2 Grid mesh for flowfield simulation.

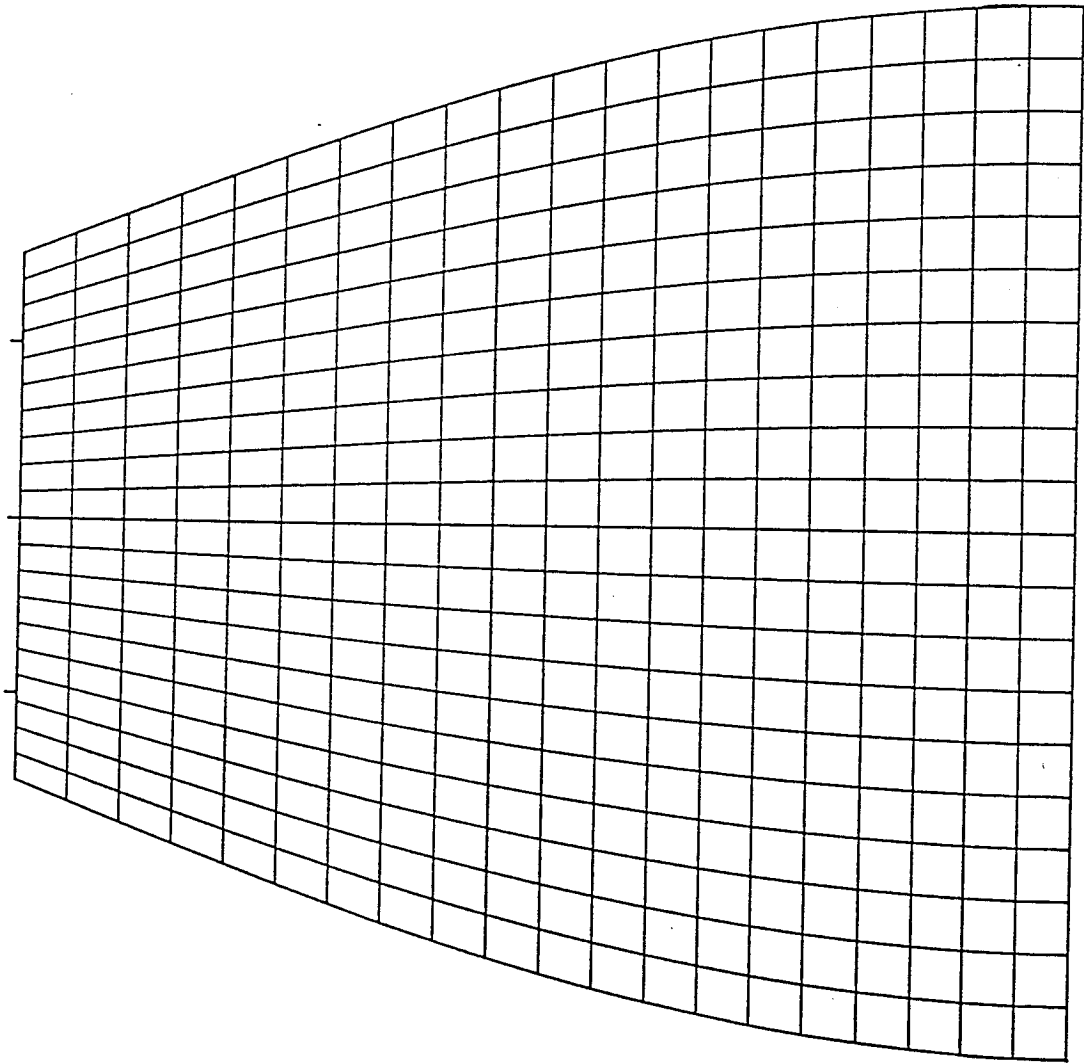


Fig. 6.3 Grid mesh for radiation simulation.

### 6.2.2 Numerical Algorithm

The governing equations, Eqs. (6.1), are expressed in the computational domain as

$$\frac{\partial \hat{U}}{\partial t} + \frac{\partial \hat{F}}{\partial \xi} + \frac{\partial \hat{G}}{\partial \eta} = \hat{H} \quad (6.41)$$

where

$$\begin{aligned} \hat{U} &= UJ \\ \hat{F} &= Fy_\eta - Gx_\eta \\ \hat{G} &= Gx_\xi - Fy_\xi \\ \hat{H} &= HJ \\ J &= x_\xi y_\eta - y_\xi x_\eta \end{aligned} \quad (6.42)$$

Here  $x_\xi$ ,  $x_\eta$ ,  $y_\xi$ ,  $y_\eta$  are the transformation matrices and  $J$  is the Jacobian of the transformation. The matrices can be computed numerically once the physical grid coordinates have been prescribed.

The governing equation system, Eq. (6.41), can be stiff due to the kinetic source terms contained in the vector  $H$ . To deal with the stiff system, the approach used in Refs. 80 and 81 was followed and the kinetic source terms were computed implicitly. In a temporally discrete form, Eqs. (6.41) then become

$$\hat{U}^{n+1} = \hat{U}^n - \Delta t \left[ \left( \frac{\partial \hat{F}}{\partial \xi} \right)^n + \left( \frac{\partial \hat{G}}{\partial \eta} \right)^n - \hat{H}^{n+1} \right] \quad (6.43)$$

After employing a Newton linearization for  $H$  and rewriting in delta form, Eq. (6.43) becomes

$$[I - \Delta t K^n] \Delta \hat{U}^{n+1} = -\Delta t \hat{R}^n \quad (6.44)$$

where

$$\hat{R}^n = \left( \frac{\partial \hat{F}}{\partial \xi} \right)^n + \left( \frac{\partial \hat{G}}{\partial \eta} \right)^n - \hat{H}^n \quad (6.45)$$

is the steady-state residual,  $I$  is the identity matrix,  $K^n$  is the Jacobian of  $H$  with respect to  $U$ ,  $(\partial H / \partial U)$ , and  $\Delta U^{n+1} = U^{n+1} - U^n$ .

Once the temporal discretization used to construct Eq. (6.44) has been performed, the resulting system is spatially differenced using the explicit, MacCormack predictor-corrector schemes [82]. This results in a spatially and temporally discrete, simultaneous system of equations at each grid point [80]. Each simultaneous system is solved using the Householder technique [81] in combination with the MacCormack technique, which is then used to advance the equations in time. The modified MacCormack technique then becomes

$$\begin{aligned}
 [I - \Delta t K_{ij}^n] \Delta U_{ij}^{\overline{n+1}} &= -\Delta t \delta^+ R_{ij}^n \\
 U_{ij}^{\overline{n+1}} &= U_{ij}^n + \Delta U_{ij}^{\overline{n+1}} \\
 [I - \Delta t K_{ij}^{\overline{n+1}}] \Delta U_{ij}^{n+1} &= -\Delta t \delta^- R_{ij}^n \\
 U_{ij}^{n+1} &= U_{ij}^n + 0.5 [\Delta U_{ij}^{\overline{n+1}} + \Delta U_{ij}^{n+1}]
 \end{aligned} \tag{6.46}$$

where  $\delta^+ R$  represents a forward spatial difference of  $R$  and  $\delta^- R$  a backward spatial difference. Stress terms are differenced in the conventional manner [82]. Equations (6.46) are used to advance the solution from time  $n$  to time  $n+1$  and this process is continued until the desired integration time has been reached.

The magnitude of the time step in Eqs. (6.46) is chosen based on the physical time scales present at any given time in the solution. The fluid dynamic time step,  $\Delta t_f$ , can be shown to be limited by the CFL condition [83]

$$\begin{aligned}
 \Delta t_f \leq & \left( \frac{|u\xi_x + v\xi_y|}{\Delta\xi} + \frac{|u\eta_x + v\eta_y|}{\Delta\eta} \right. \\
 & \left. + a \sqrt{\left( \frac{\xi_x}{\Delta\xi} + \frac{\eta_x}{\Delta\eta} \right)^2 + \left( \frac{\xi_y}{\Delta\xi} + \frac{\eta_y}{\Delta\eta} \right)^2} \right)^{-1}
 \end{aligned} \tag{6.47}$$

where  $a$  is the local speed of sound. The chemical relaxation time for species  $i$  is given by [84]

$$t_c = \frac{\rho f_i}{\dot{w}_i} \tag{6.48}$$

Changes in this relaxation time are then given by

$$\Delta t_c = \frac{\Delta(\rho f_i)}{\dot{w}_i} \quad (6.49)$$

since  $\dot{w}_i$  remains nearly constant over a time step. For accuracy, it is required that the chemical time step be chosen such that no change in mass fraction greater than 0.01 occurs over that time step. The computational time step  $\Delta t$  is then chosen to be the minimum of all the grid points in terms of the both fluid and chemical time steps, i.e.,

$$\Delta t = \min(\Delta t_f, \Delta t_c) \quad (6.50)$$

### **6.2.3 Boundary and Initial Conditions**

The governing equations, Eqs. (6.1), require boundary conditions along all four boundaries. For the problems to be considered, the inflow boundary is supersonic, so the velocities, static temperature, pressure, and species mass fractions are specified and fixed there. The outflow boundary is also supersonic, and the values of the velocities, static temperature, pressure, and species mass fractions are determined by extrapolation from upstream values. Only the upper half of the flow domain is computed due to the assumed symmetry of the flow. The upper boundary is treated as a solid wall. This implies a non-slip boundary condition. The wall temperature is given and wall species mass fractions and pressures are extrapolated from interior grid points, by assuming a non-catalytic wall as well as the boundary layer assumptions on the pressure gradient. Symmetry boundary conditions are imposed at the lower boundary, that is, at the centerline.

Equations (6.1) also require a set of initial conditions. The equations are initialized by setting values of the velocities, static temperature, pressure, and species mass fractions throughout the domain to the values chosen initially for boundary conditions at the inflow boundary. Having specified all required initial and boundary data, the equations are marched in time until steady state solutions are achieved.



### 6.2.4 Artificial Viscosity

With the numerical algorithm of Sec. 6.2.2, high frequency nonlinear instabilities can appear as the solution develops. For example, flow oscillations can result from the odd-even decoupling inherent in the use of second-order central differencing for the inviscid terms. In addition, physical phenomena such as shock waves can cause instabilities when they are captured by the finite difference algorithm. Artificial viscosity, or smoothing, is normally added to the solution algorithm to suppress these high frequency instabilities. In this study, the artificial viscosity  $F_{av}$  is added to the vector  $\hat{F}$  in Eq. (6.41) as following

$$F_{av} = (\lambda J)_{i,j} [C_1 \delta_\xi^2 P + C_2 \delta_\xi^2 T + C_3 \delta_\xi^2 f] (U_{i,j} - U_{i-1,j}) \quad (6.51)$$

where

$$\lambda = \frac{|\xi_x u + \xi_y v| + a \sqrt{\xi_x^2 + \xi_y^2}}{\Delta \xi} + \frac{|\eta_x u + \eta_y v| + a \sqrt{\eta_x^2 + \eta_y^2}}{\Delta \eta} \quad (6.52)$$

$$\delta_\xi^2 P = \frac{|P_{i+1,j} - 2P_{i,j} + P_{i-1,j}|}{P_{i+1,j} + 2P_{i,j} + P_{i-1,j}} \quad (6.53)$$

$$\delta_\xi^2 T = \frac{|T_{i+1,j} - 2T_{i,j} + T_{i-1,j}|}{T_{i+1,j} + 2T_{i,j} + T_{i-1,j}} \quad (6.54)$$

$$\delta_\xi^2 f = \frac{|f_{i+1,j} - 2f_{i,j} + f_{i-1,j}|}{f_{i+1,j} + 2f_{i,j} + f_{i-1,j}} \quad (6.55)$$

The other artificial viscosity  $G_{av}$  follows similar formulas as  $F_{av}$ . Equation (6.51) was suggested by Pulliam [85]. In its original form, only the term  $\delta_\xi^2 P$  was used; Singh et al. [86] found that for some problems especially those with chemical reaction this is not sufficient and suggested inclusion of the term  $\delta_\xi^2 T$  and  $\delta_\xi^2 f$ . In the term  $\delta_\xi^2 f$ ,  $f$  can be the mass fraction for one species or for several different species. The coefficient  $C_1$ ,  $C_2$  and  $C_3$  must be selected by numerical experiment. For the cases investigated in this study, all coefficients were fixed as a constant value of one half.

### **6.2.5 Solution Procedures**

With consideration of radiative heat transfer, solution procedures employed in this study are summarized as following:

(a) First, Eqs. (6.1) were solved without consideration of radiation in terms of the modified MacCormack schemes;

(b) The steady solutions for temperature, pressure and species mass fractions were then used in the Monte Carlo simulation. The computed radiative source term  $-\nabla \cdot q_r$  from the MCM was based on a different grid from that used for Eqs. (6.1). Linear interpolation and extrapolation were employed for the transformation of  $-\nabla \cdot q_r$  between the two grids;

(c) The transformed  $-\nabla \cdot q_r$  was substituted into Eqs. (6.1), and Eqs. (6.1) were solved again. If the differences between two consecutive steady solutions were smaller than a designated tolerance, the computation was terminated. Otherwise, steps (b) and (c) were repeated until solutions converge.

It is noted that there are two levels of numerical procedures employed here which result in two different iterative procedures. One is the numerical procedure for solving Eqs. (6.1) and their solutions were iterated with time. The other is the numerical procedure for evaluating the radiative source term using the MCM, which results in the iteration of steady state solutions.

## **6.3 Results and Discussion**

Based on the theoretical and numerical analyses described earlier, a computer code has been developed to simulate two-dimensional supersonic chemically reacting and radiating nozzle flows on a Cray X-MP machine. The specific goal in this study was to investigate the effects of radiation on the flowfield and heat flux on the nozzle wall. By referring to [2], several problems have been considered. They contain four parameters:

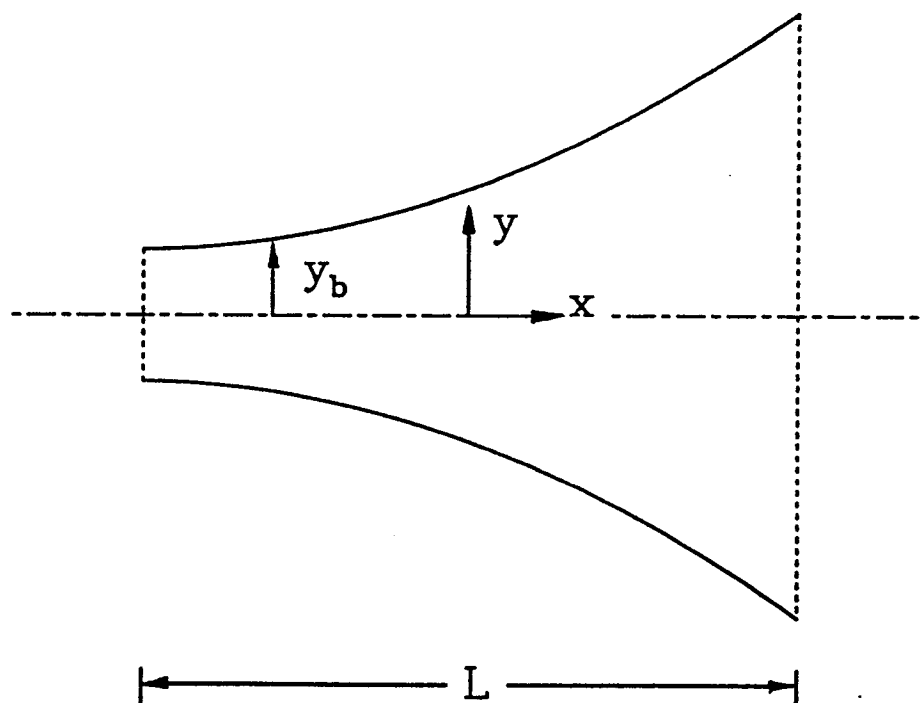
equivalence ratio of hydrogen and air, inlet flow temperature, wall temperature and nozzle size. Numerical solutions have been obtained for a variety of combinations of these parameters. In each problem, flow is introduced at the nozzle as a uniform velocity of 1230 m/s and a pressure of 1 atm. The grid size for solving the governing equations was  $71 \times 41$  (upper half of the nozzle). Further refinement of the grid produced only small changes in the results. For a given radiative source distribution, the residuals of Eqs. (1) were reduced by eight orders of magnitude in 3,000 iterations for a typical case and the steady state solutions were considered to have been obtained. The corresponding CPU time is about six minutes.

To check the accuracy of the computational scheme, a preliminary calculation has been carried out for a chemically reacting nozzle flow without consideration of radiation and the present solution is compared with that in Ref. 87. Figure 6.4 shows the physical model for this calculation. It is noted that the nozzle walls are adiabatic walls in this case. Figures 6.5 and 6.6 demonstrate the frozen and reacting temperature distributions along the centerline. The present solution is found to agree with the available solution [87].

For the temperature ranges considered, the important radiating species are OH and  $H_2O$ . But OH is a much less radiation participating species compared to  $H_2O$ . In addition, the concentration of OH is several times less than that of  $H_2O$  for the problems considered. So, the contribution of radiation from OH has been neglected in this study. For  $H_2O$ , there are five important absorption bands. All these bands have been taken into account and they consist of 295 narrow bands in the spectral range from  $150\text{ cm}^{-1}$  to  $7500\text{ cm}^{-1}$  [33]. In addition, for all the problems considered, the nozzle wall is assumed to be gray and the wall emissivity is taken to be 0.8. The inlet and outlet surfaces of the nozzle flow are treated as pseudoblack walls with the same temperatures as the local gases.

To assure that the statistical results make sense in the Monte Carlo simulation, two requirements, the accuracy of the statistical results and the independence of the results on the grid, must be met. In this study, the designated statistical accuracy of the results is

$$\frac{y_b}{L} = 0.1 + 0.008\left(\frac{x}{L}\right) + 0.36\left(\frac{x}{L}\right)^2$$



$$M_{in} = 1.3, P_{in} = 1.0 \text{ atm}, T_{in} = 3000 \text{ K}, L = 0.25 \text{ m}, \phi = 1.0$$

Fig. 6.4 Physical model for validation calculation.

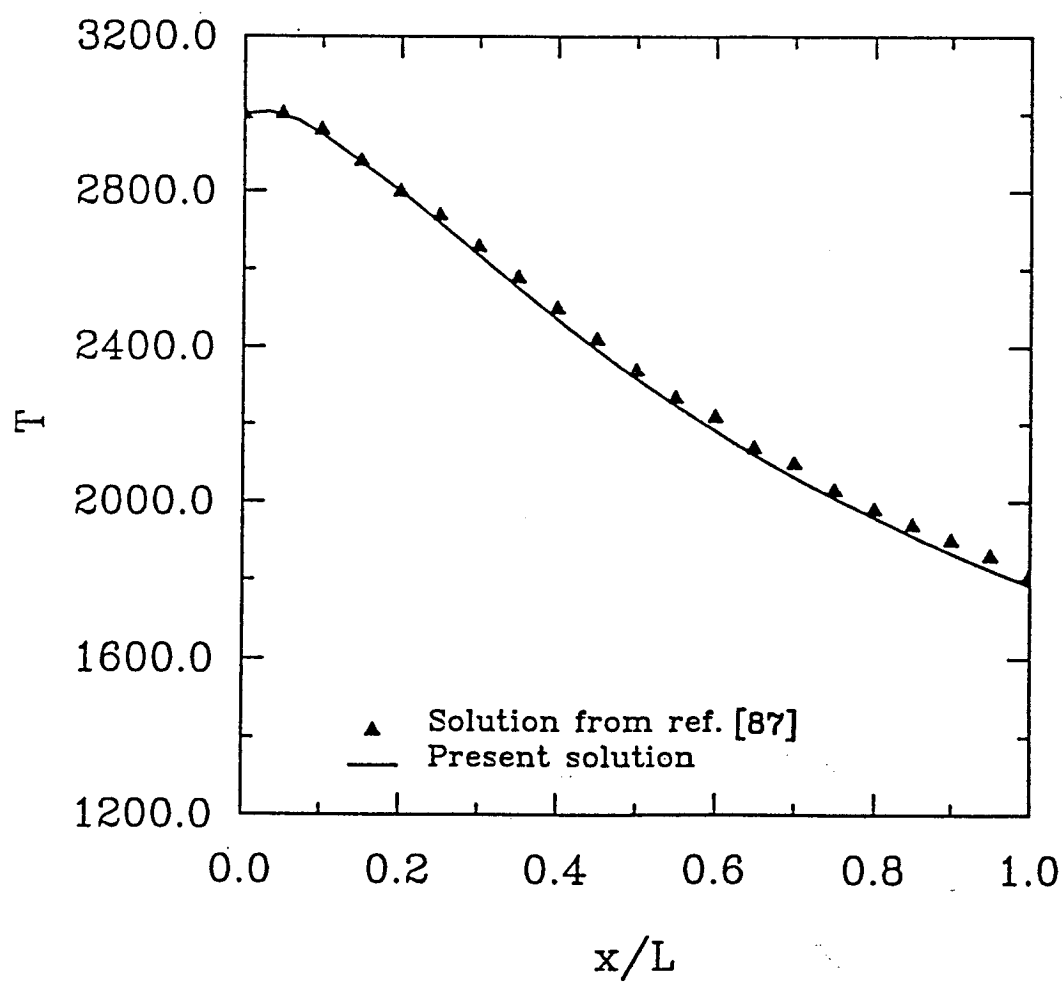


Fig. 6.5 Comparison of frozen temperatures along the centerline.

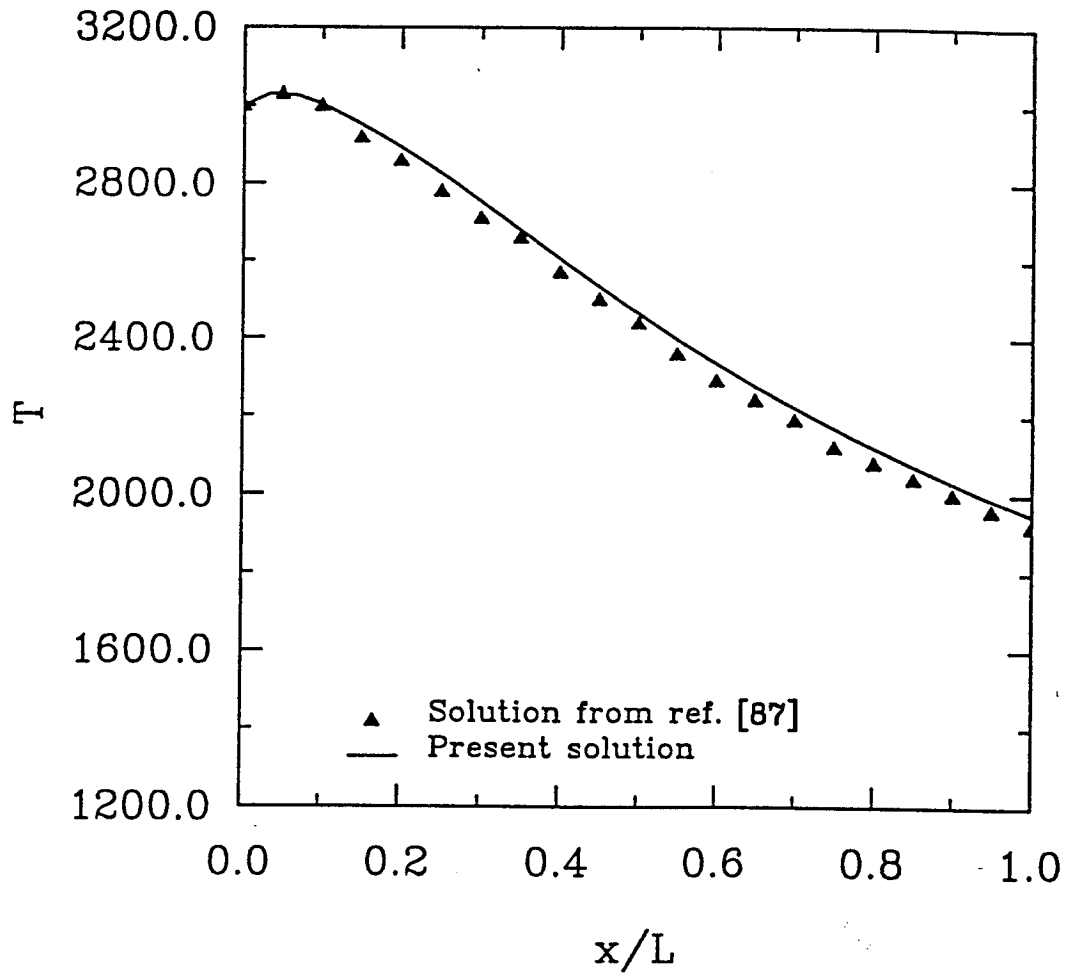


Fig. 6.6 Comparison of reacting temperatures along the centerline.

defined in such a way that when the relative statistical errors of results are less than  $\pm 5\%$ , the probability of the results lying within these limits is greater than 95%. Independence of the results on a grid is considered to have been achieved when the volume element number in the x direction is 20 and the volume element number in the y direction is 20 as shown in Fig. 6.3. For this grid, the total number of energy bundles had to be 5,000,000 and the required CPU time was about one hour in order to meet the designated statistical accuracy in results for a typical problem. To test the independence of the Monte Carlo results on the grid, the same problem was investigated with a finer grid in which the volume element number in the x direction was increased to 30 and the volume element number in the y direction was doubled. To obtain the same accurate results, the total number of energy bundles had to increase to 15,000,000 and the corresponding CPU time increased to three hours. Comparing the solutions for the two different grids, it was found that the difference for the net radiative wall flux was never more than 2%, and the difference for the radiative source term was a little higher but less than 10%. In fact, the net radiative wall flux is the quantity we are most interested in, and its accuracy seems more important to us.

The grid considered for Monte Carlo computations in this study is coarser than that for numerical solutions of the energy equation. The intermediate values of the radiative source term within the grid for solutions of Eqs. (6.1) are obtained by interpolation and extrapolation. This should not introduce significant errors as the radiative source term is a slowly varying function compared to the temperature and its derivatives [6]. The major CPU time consumed is in the Monte Carlo simulation. Fortunately, Monte Carlo subroutines only need to be called one or two times to obtain converged steady state solutions. The reason for this will be explained later. It is believed that the computational time for Monte Carlo simulations can be reduced considerably if the code is vectorized and parallelized.

The radiative effects on the flowfield were investigated first. It is common knowledge that convective heat transfer is very strong for a supersonic flow. Hence the effects of radiation may not be very important. To determine these effects quantitatively, a typical problem was selected in which the equivalence ratio of hydrogen and air, wall temperature, inlet flow temperature and the nozzle length are taken to be  $\phi=1.0$ ,  $T_w=1900$  K,  $T_i=1900$  K and  $L=2.0$  m. The inlet species mass fractions are  $f_{H_2} = 0.0283$ ,  $f_{O_2} = 0.2264$ ,  $f_{H_2O} = 0.0$ ,  $f_{OH} = 0.0$ ,  $f_O = 0.0$ ,  $f_H = 0.0$ ,  $f_{N_2} = 0.74529$ . Figures 6.7–6.10 show the temperature, pressure, density distributions and velocity vector plots, respectively. Figures 6.11–6.14 show the mass fraction distributions for the species  $H_2O$ ,  $OH$ ,  $H_2$  and  $O_2$ , respectively. Knowing this information is essential in analyzing the effect of radiative heat transfer. As the premixed mixture of hydrogen and air enters the nozzle, an exothermic chemical reaction takes place immediately, and the temperature, pressure, and density increase abruptly, reaching their peaks in a region closer to the inlet location (Figs. 6.7–6.9) while the velocity decreases slightly (Fig. 6.10). During this rapid change in temperature, pressure, and density, the two major products  $H_2O$  and  $OH$  experience a big jump in mass fraction (Figs. 6.11 and 6.12) while the two major reactants  $H_2$  and  $O_2$  experience a big drop in mass fraction (Figs. 6.13 and 6.14). As the flow continues to move downstream, supersonic expansion plays a major role, and the temperature, pressure, and density are decreased while velocity is increased. At the same time, the chemical reaction proceeds but it becomes very weak. This is why there is little change in mass fractions for the species  $H_2O$ ,  $OH$ ,  $H_2$  and  $O_2$  in the downstream region. Computation has been conducted for other cases also. Similar trends in results for temperature, pressure, density, velocity, and mass fractions for all species were also observed.

Figure 6.15 shows the radiative source distributions at three different locations for the case considered in Figs. 6.7–6.14. At the location  $x/L=0.1$ , temperature and pressure are very high and there is more radiant energy emitted than absorbed. Consequently, the



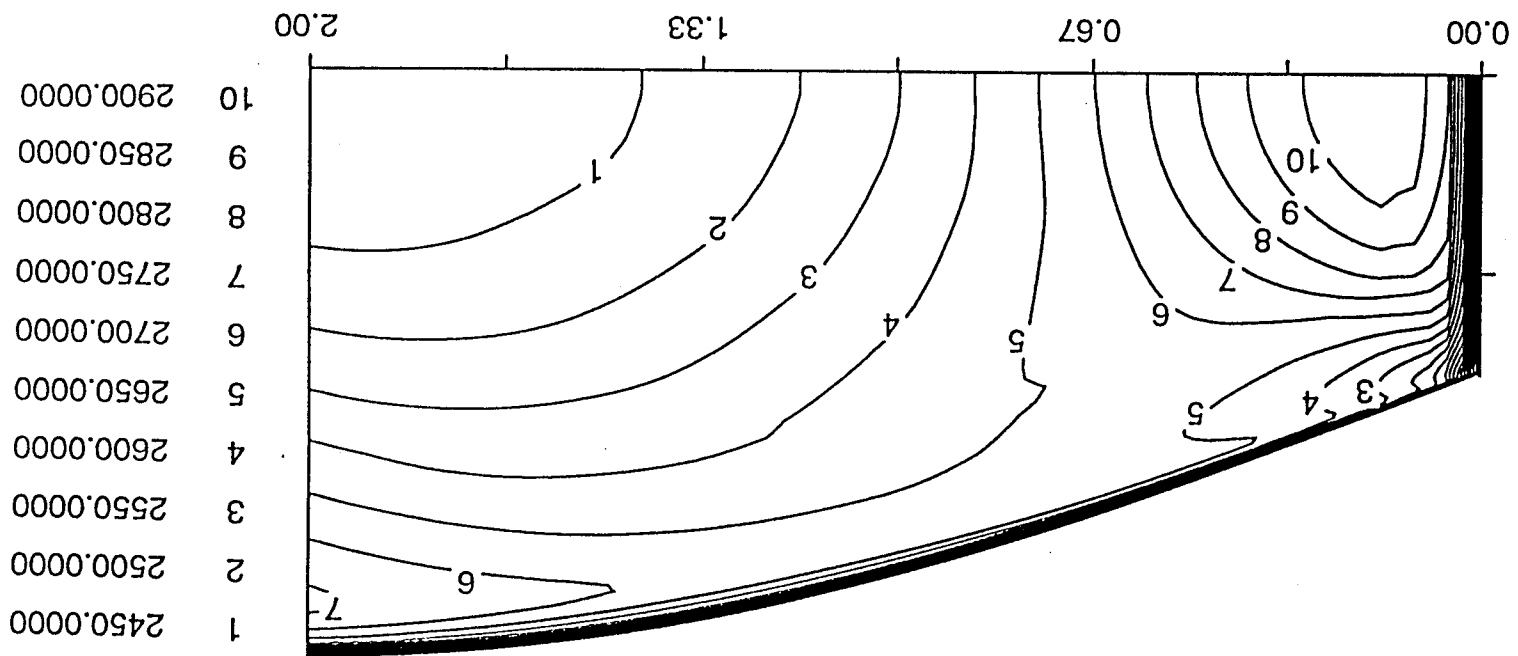


Fig. 6.7 Temperature contours in the nozzle.

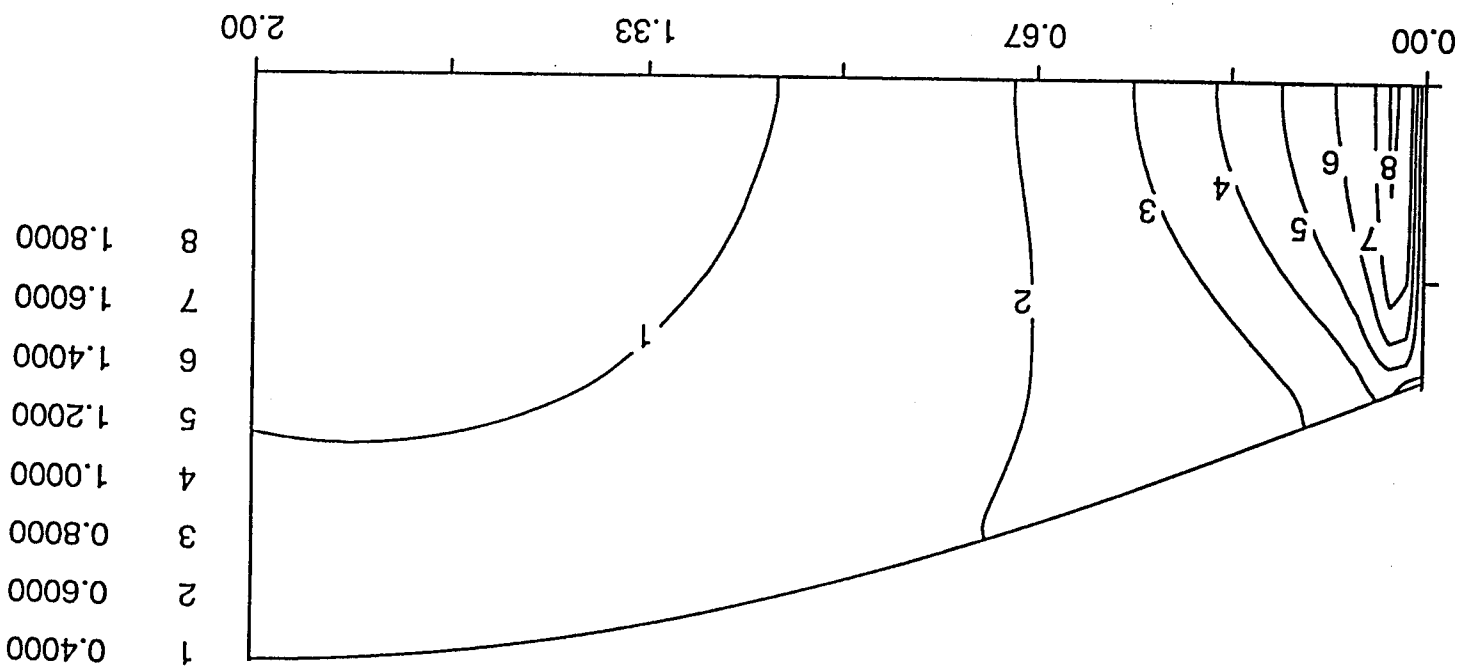


Fig. 6.8 Pressure contours in the nozzle.

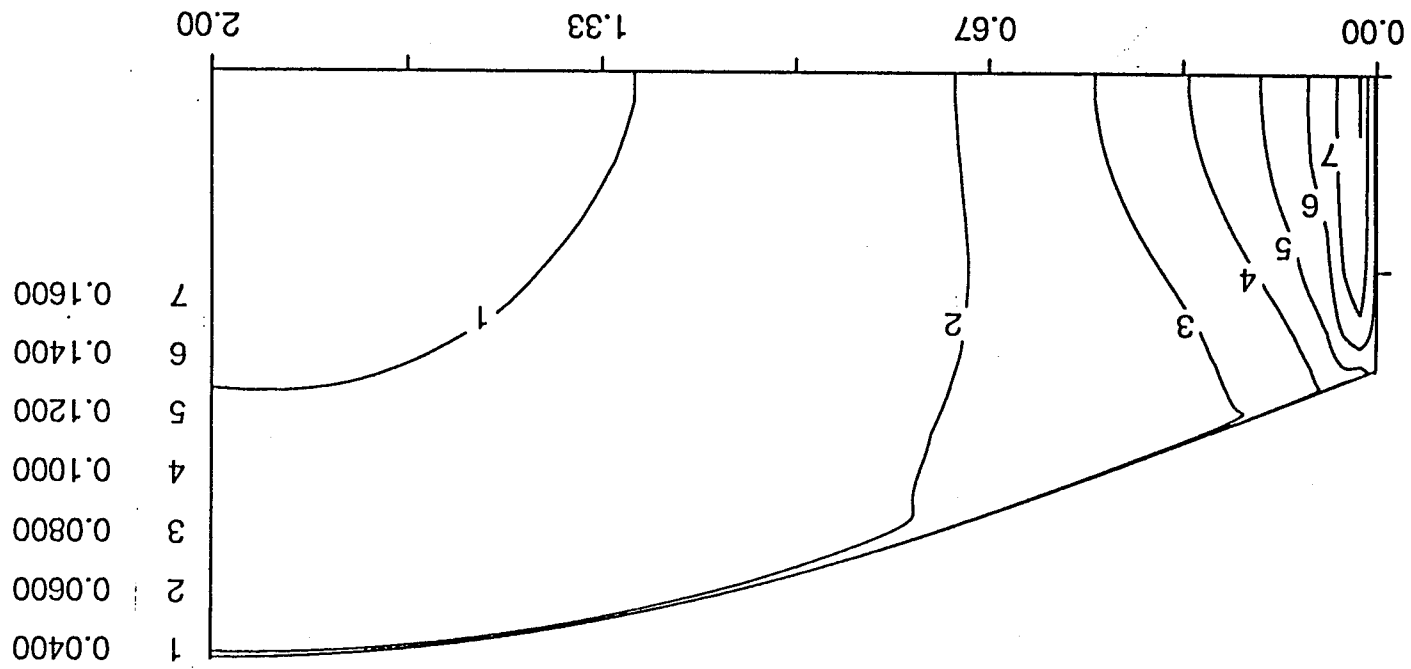


Fig. 6.9 Density contours in the nozzle.

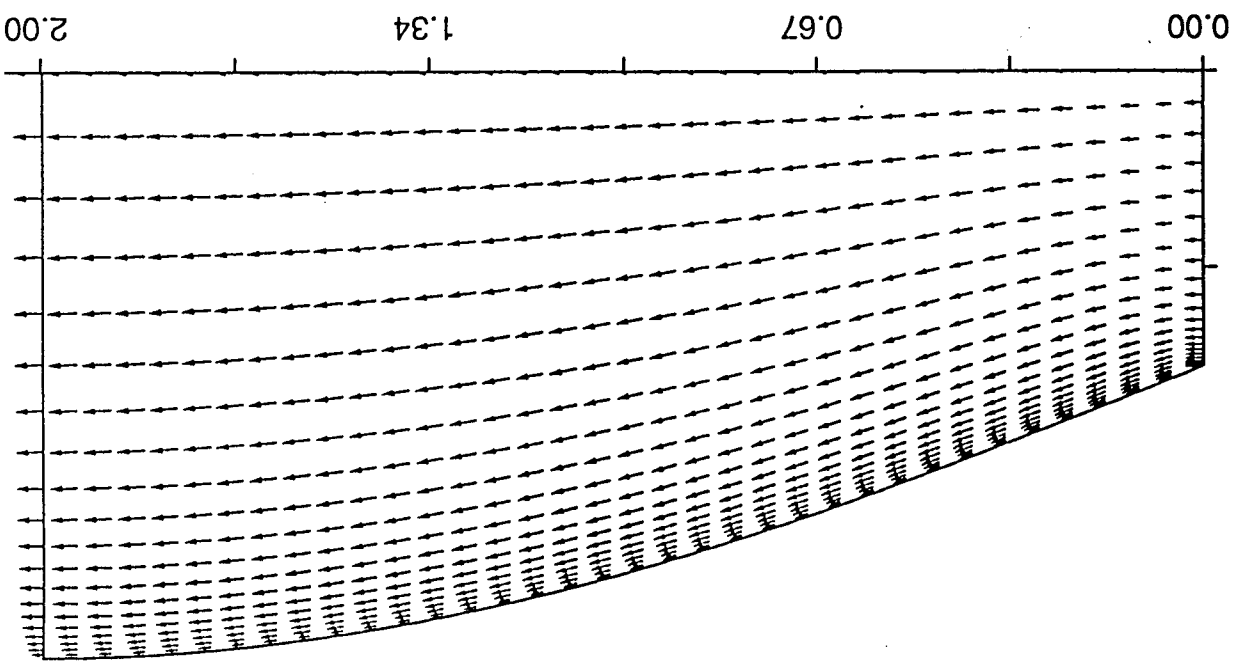


Fig. 6.10 Velocity vectors in the nozzle.

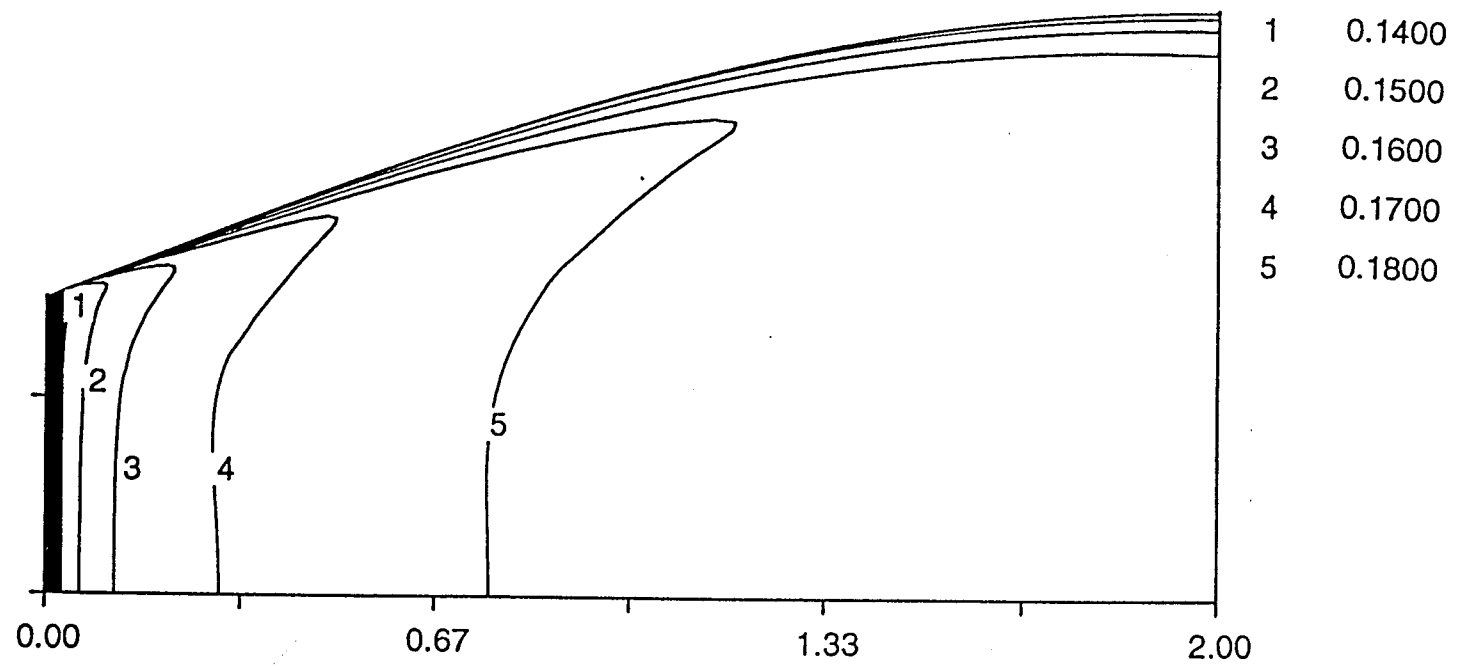


Fig. 6.11 H<sub>2</sub>O mass fraction contours in the nozzle.

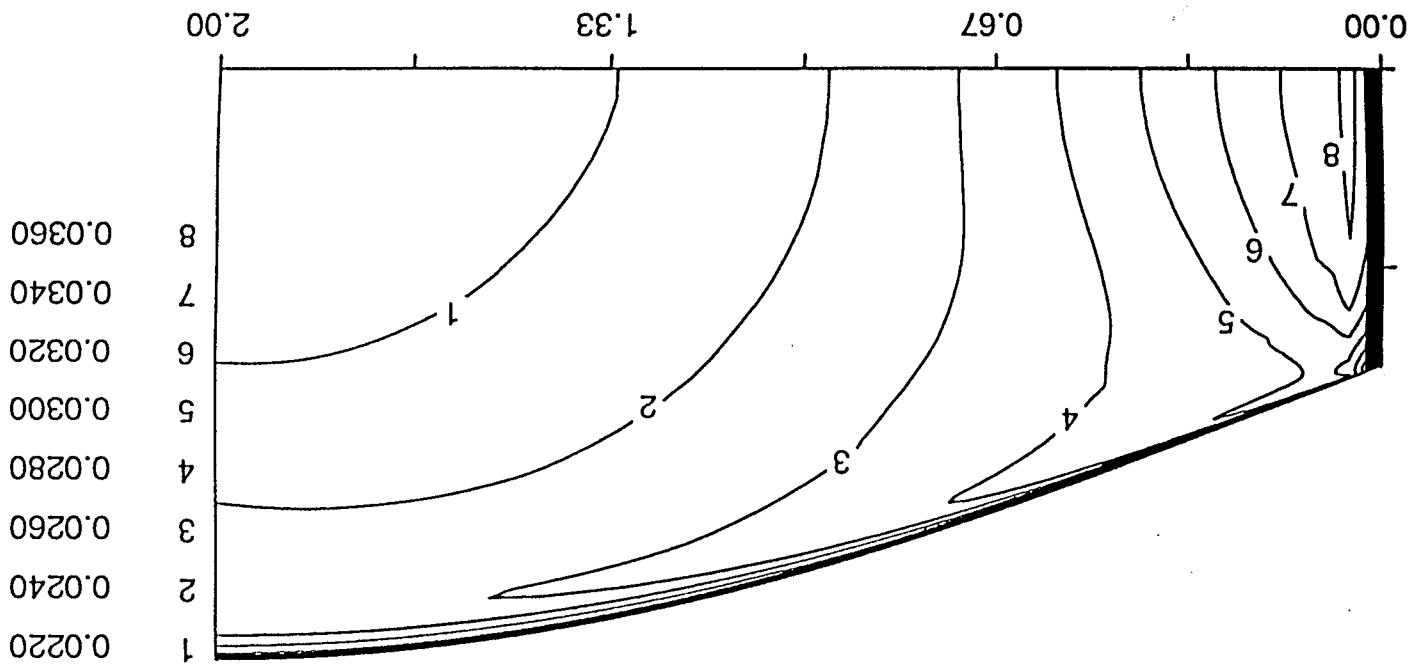


Fig. 6.12 OH mass fraction contours in the nozzle.

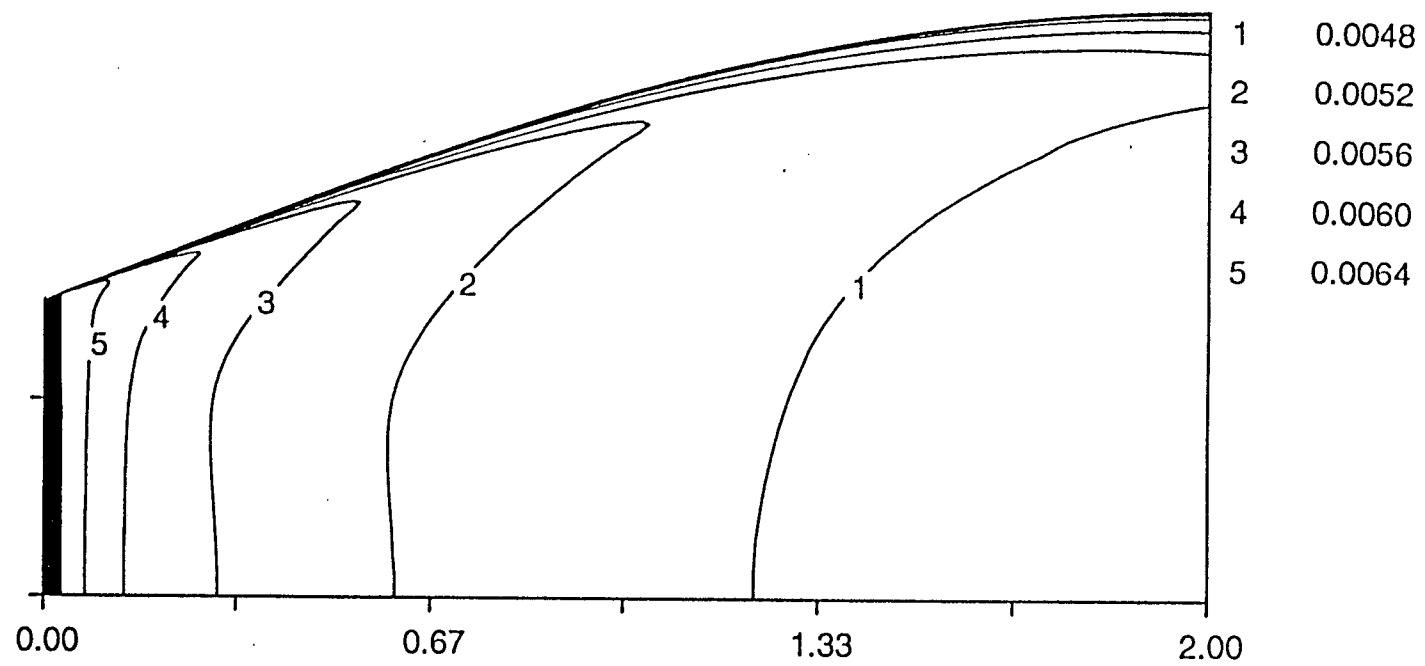


Fig. 6.13  $H_2$  mass fraction contours in the nozzle.

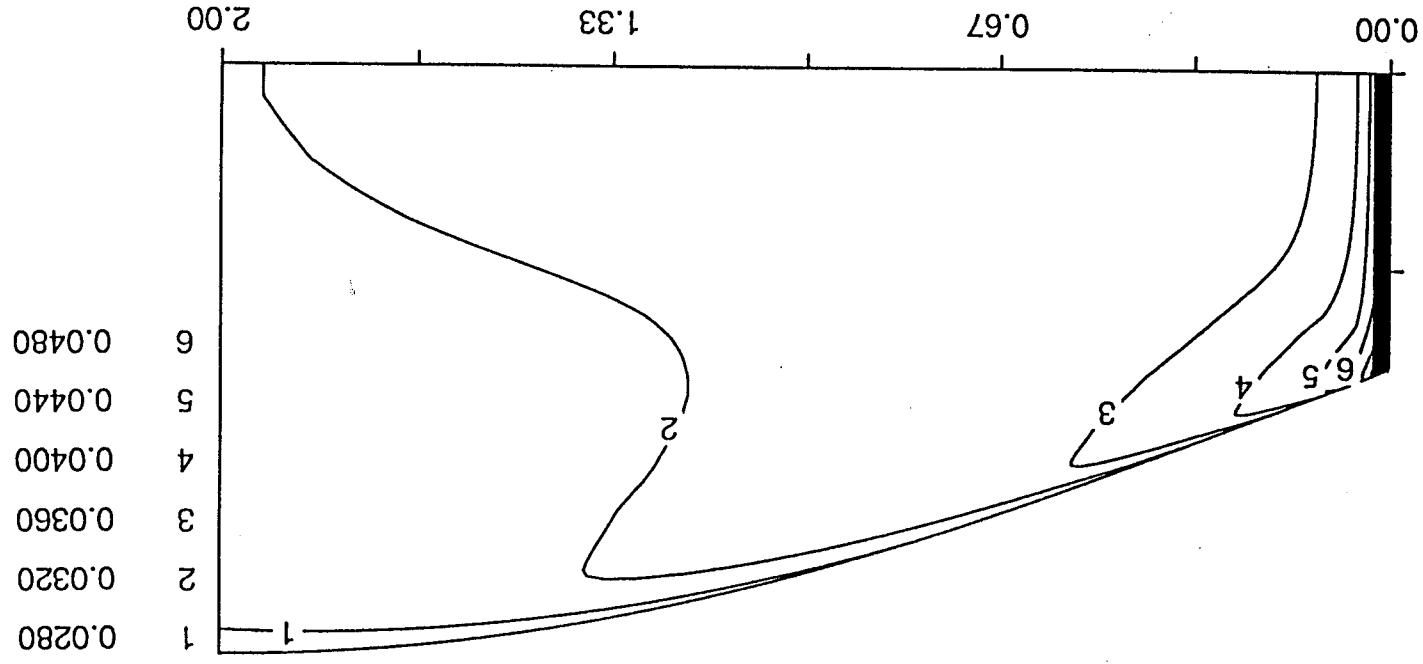


Fig. 6.14  $O_2$  mass fraction contours in the nozzle.



radiative source distribution is higher than at locations  $x/L=0.5$  and  $0.9$ . The trend in results for  $-\nabla \cdot q_r$  at the location  $x/L=0.1$  is seen to be different from the results of other locations due to a decrease in temperature as the distance from the center line increases. The convective heat transfer distributions for the same locations as in Fig. 6.15 were also calculated but they are not plotted in Fig. 6.15. This is because of large differences between the convective and radiative results; and also due to opposite signs for convective results at different locations. In most regions, the absolute value of the convective heat transfer is two or three orders of magnitude larger than the radiative source term. This situation does not change as long as the speed of the flow is very high. Consequently, the effects of radiation on the flowfield are very weak for supersonic flows. This confirms our expectation and also answers the question that the Monte Carlo subroutine only needs to be called one or two times to obtain converged steady state solutions. As a matter of fact, a case without radiation was considered and the differences in temperature, pressure, density, and species mass fractions between the two cases were found to be less than  $\pm 1\%$ .

The radiative effects on the heat transfer on the nozzle walls are investigated next. Unlike the radiative effects on the flowfield, the effects of radiation on the nozzle wall flux are significant when compared with those from conduction. The following results will demonstrate the relative importance of radiative and conductive wall fluxes and how they change with equivalence ratio, wall temperature, inlet flow temperature, and nozzle size. Here, the conductive wall flux is defined as

$$q_{cw} = -k(T_w) \left( \frac{\partial T}{\partial n} \right)_{wall} \quad (6.56)$$

where  $n$  represents normal direction to the wall.

The effects of the equivalence ratio  $\phi$  on  $q_{rw}$  and  $q_{cw}$  are illustrated in Fig. 6.16. For a specific  $\phi$  value,  $q_{cw}$  is seen to increase first, reach a peak and then decrease. This is compatible with the trends in temperature variation as seen in Fig. 6.7. Unlike  $q_{cw}$ ,  $q_{rw}$  is seen to increase with distance along the nozzle. This behavior is justifiable. In this

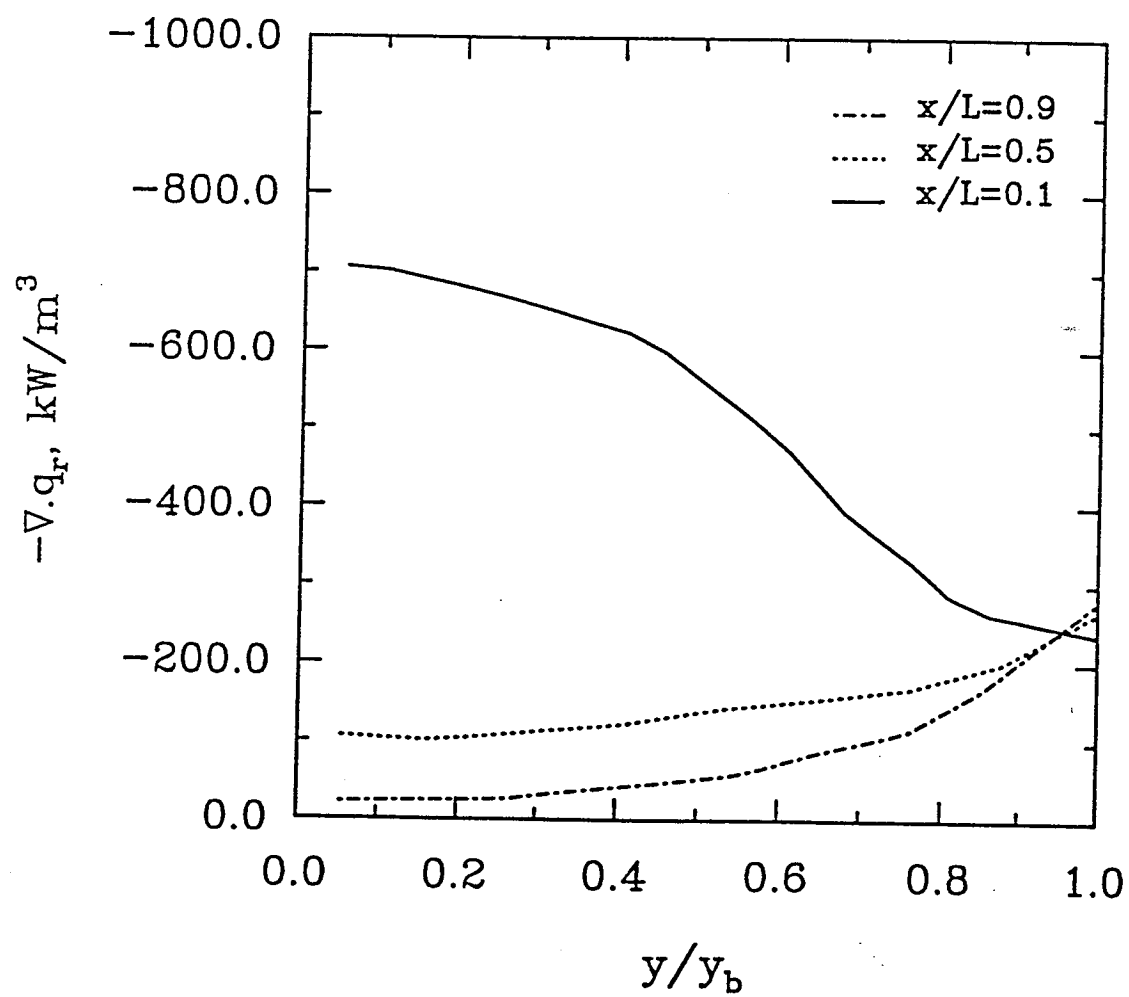


Fig. 6.15 Radiative source distribution at three locations.

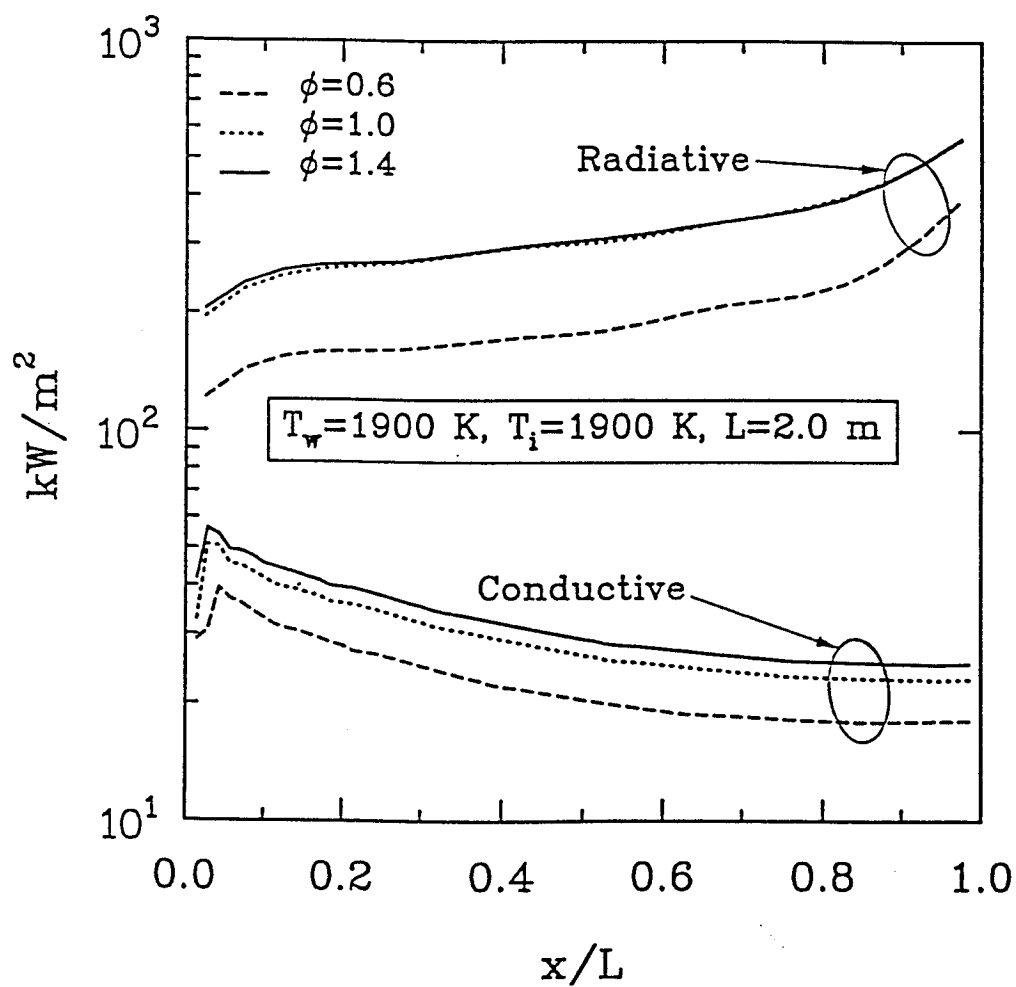


Fig. 6.16 Comparison of radiative and conductive wall fluxes for three different equivalence ratios.

study, the inlet and outlet of the flow are treated as the pseudoblack walls. The outlet flow temperatures are larger than the inlet flow temperatures and the outlet area is also bigger than the inlet area. In addition, as the flow goes downstream, the cross-sectional area of the flow increases. Consequently, the optical length increases. These two reasons result in higher value of  $q_{rw}$  as the distance from the inlet location increases. Comparing the values of  $q_{rw}$  and  $q_{cw}$  for each case, it is clear that radiation is predominant. Even in the inlet region,  $q_{rw}$  is more than two times higher than  $q_{cw}$ . The results for three different equivalence ratios reveal different behavior for combustion with lean and rich mixtures. As  $\phi$  increases from 0.6 to 1.0, the flow temperature and H<sub>2</sub>O mass fraction increase by about 10% and 50% respectively, and pressure decreases by about 5%. The effects of these changes result in a sizable increase in the values of  $q_{rw}$  and  $q_{cw}$ . However, as  $\phi$  increases from 1.0 to 1.4, the flow pressure decreases by about 5% and the H<sub>2</sub>O mass fraction increases by about 15%, but the temperature shows little change. This results in only a slight change in the values of  $q_{rw}$  and  $q_{cw}$ .

Figure 6.17 shows the effects of the nozzle wall temperature on  $q_{rw}$  and  $q_{cw}$ . The change of the nozzle wall temperature is found to have little influence on the combustion, and the flow temperature, pressure and H<sub>2</sub>O mass fraction remain almost the same in most regions as  $T_w$  varies from 1500 K to 2100 K. As a result, the magnitude of the radiant energy absorbed on the wall is very close for the three cases with different nozzle wall temperatures. The value of  $q_{rw}$  is equal to the absorbed radiant energy minus the emitted radiant energy. So  $q_{rw}$  is reduced with higher wall temperature, as seen in Fig. 6.17. As far as  $q_{cw}$  is concerned, except in the entrance region,  $q_{cw}$  is seen to exhibit minor changes among the cases with different wall temperatures.

The effects of the inlet flow temperature on  $q_{rw}$  and  $q_{cw}$  are demonstrated in Fig. 6.18. Inspection of the distribution of the  $q_{rw}$  value among the three cases reveals a very interesting feature of  $q_{rw}$ . The values of  $q_{rw}$  along the wall are not monotonically increased or decreased with  $T_i$ . The combined effects of temperature, pressure and H<sub>2</sub>O

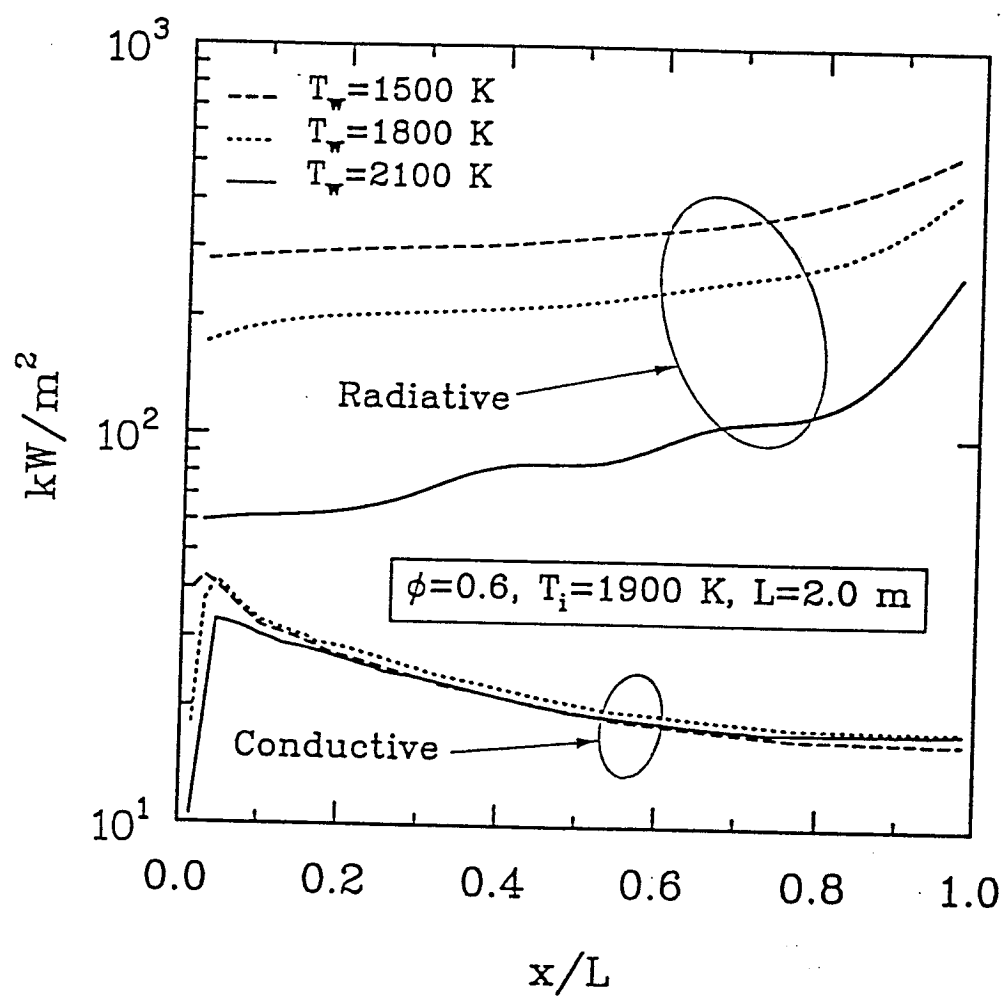


Fig. 6.17 Comparison of radiative and conductive wall fluxes for three different wall temperatures.

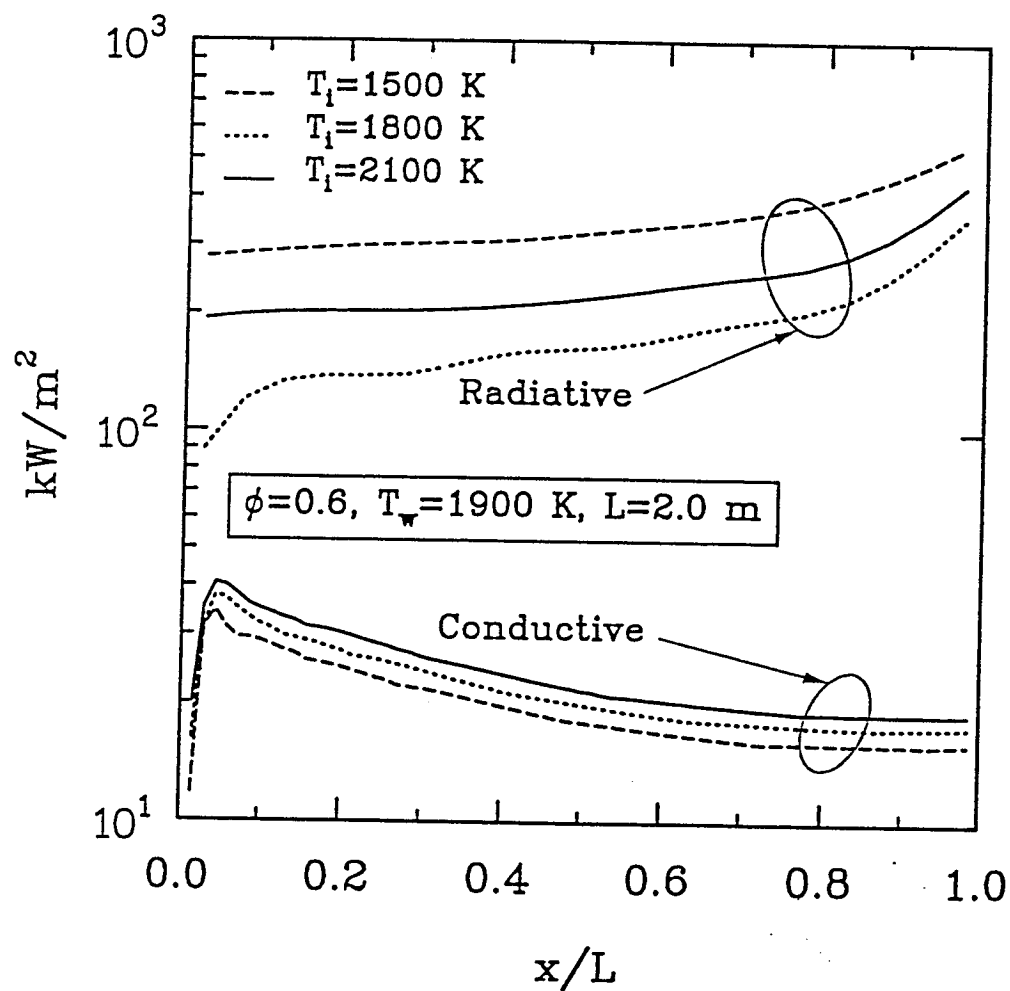


Fig. 6.18 Comparison of radiative and conductive wall fluxes for three different inlet temperatures.

mass fraction in the flow on radiation are responsible for this behavior. It is well known that increase of temperature, pressure and concentration of participating media enhances radiation. As  $T_i$  varies from 1500 K to 1800 K and then from 1800 K to 2100 K, the flow temperature increases by about 5% while the pressure and  $H_2O$  mass fraction decrease by about 10% and 15% respectively at each stage. An increase in temperature tries to reinforce the radiation while a decrease of pressure and  $H_2O$  mass fraction tries to reduce the radiation. So there exist two driving forces which compete with each other to affect the radiation. As a consequence of the competition, the lowest curve for  $q_{rw}$  is seen for the case with  $T_i = 1800$  K and the highest values are observed for the case with  $T_i = 1500$  K. Unlike  $q_{rw}$ , the values for  $q_{cw}$  are found to increase monotonically with  $T_i$ . This is because the convective wall flux is only dependent on temperature.

Finally, the effects of the nozzle size on  $q_{rw}$  and  $q_{cw}$  are illustrated in Fig. 6.19. By changing the nozzle length, geometrically similar nozzles with different sizes can be obtained. As the nozzle length is reduced from 2.0 m to 1.0 m and then from 1.0 m to 0.5 m, the flow temperature and  $H_2O$  mass fraction are decreased by about 5% while the pressure is increased by about 2% at each stage. The effect of increased pressure on the radiation is overshadowed by a decrease in the nozzle size, temperature and  $H_2O$  mass fraction. Hence, lower values of  $q_{rw}$  are seen in the figure as the nozzle length is reduced. For the smaller nozzle size, the flow temperature may be lower, but the normal derivative of temperature is actually higher. Therefore, contrary to  $q_{rw}$ , the value  $q_{cw}$  is observed to increase with a decrease in the nozzle size. The opposite trend between the values of  $q_{rw}$  and  $q_{cw}$  brings a question about the role of radiation in heat transfer on the nozzle wall. With a decrease of nozzle size, the differences between the values of  $q_{rw}$  and  $q_{cw}$  are reduced and the dominance of radiation is diminished. In fact, at  $L=0.5$ , the value of  $q_{cw}$  is larger than the value of  $q_{rw}$  in some parts of the nozzle wall. It is expected that radiation will become less important and conduction will replace radiation as the dominant mode of heat transfer on the nozzle wall if the nozzle size is reduced further.

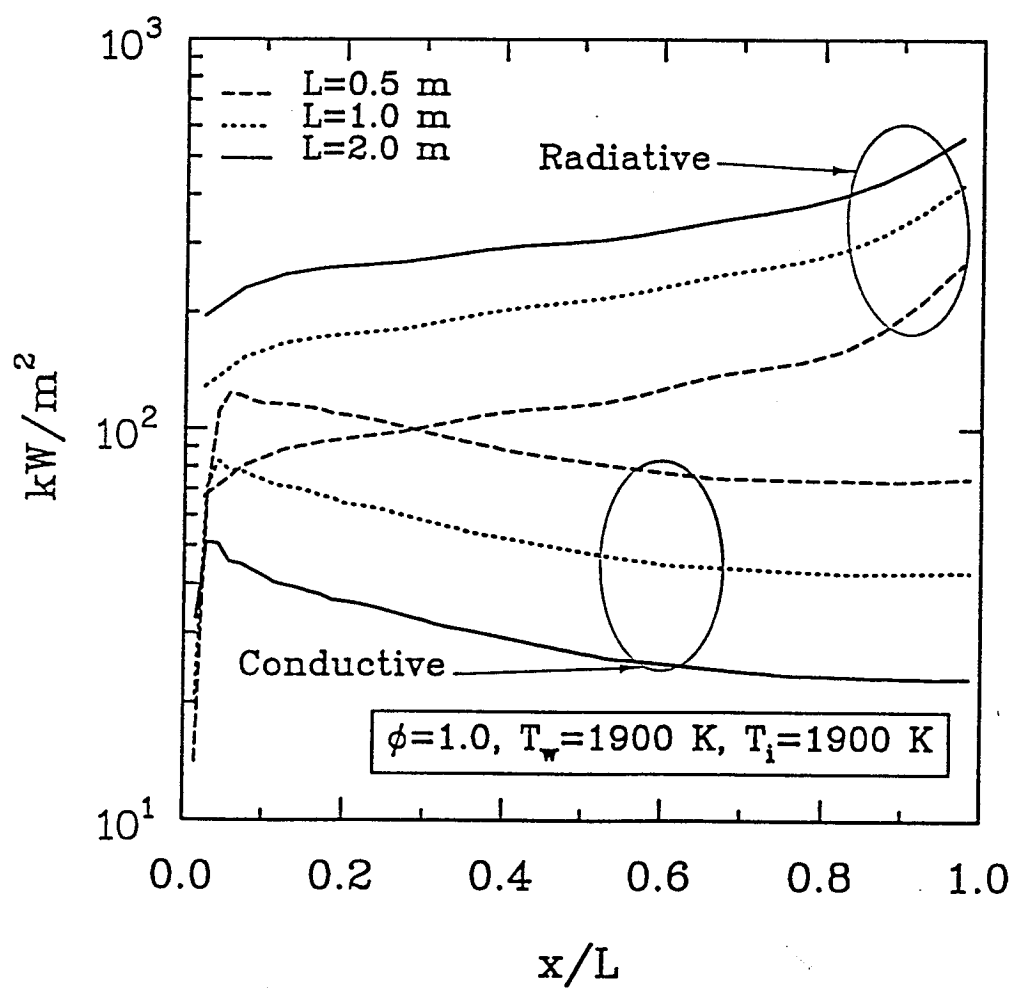


Fig. 6.19 Comparison of radiative and conductive wall fluxes for three different nozzle sizes.



## Chapter 7

### CONCLUDING REMARKS

The MCM has been applied to investigate radiative heat transfer in a nongray participating medium in an exact manner. The nongray model employed is based on a random statistical narrow band model. When a narrow band model is employed in the MCM, the spectral correlation only occurs between the transmittances of two different segments of the same path in the statistical relationship for determining the absorption location of an energy bundle. For the case with reflecting walls, Monte Carlo treatment with a narrow band model is similar to that with a gray model, and the spectral correlation between the reflected component of the wall radiosity and the transmittance occurring in other methods does not exist. Consideration of different problems reveals that the Monte Carlo solutions are in good agreement with available results of other methods but the MCM is much simpler to implement than other methods.

The validity of the Monte Carlo correlated formulations is further established by considering the steady-state energy transfer in laminar, incompressible, constant properties, fully developed flow of absorbing-emitting gases between two parallel plates. The nongray Monte Carlo solutions were found to be in good agreement with the available approximate solutions. The gray Monte Carlo solutions were also obtained for the same problem and they also essentially match the available analytical solutions.

The exact correlated and non-correlated Monte Carlo formulations are very complicated for multi-dimensional systems. Solutions of these formulations are extremely difficult, if not impossible. However, by introducing the assumption of an infinitesimal volume element, the approximate correlated and non-correlated formulations were obtained which were tractable compared to the exact formulations. Consideration of dif-

ferent problems and comparison of different solutions reveals that the approximate and exact correlated solutions agree very well, and so do the approximate and exact non-correlated solutions. However, the two non-correlated solutions lack physical meanings because they usually differ from the correlated solutions significantly. An accurate prediction of radiative heat transfer in any nongray and multi-dimensional system is possible by using the approximate correlated formulations.

By investigating the radiative interactions for chemically reacting supersonic flows of premixed hydrogen and air in an expanding nozzle, the correlated Monte Carlo method developed earlier has been found to be a very convenient and reliable tool to analyze radiative heat transfer in multi-dimensional nongray systems. For chemically reacting supersonic flows, the effects of radiation on the flowfield can be neglected but the radiative effects on the heat transfer on the nozzle wall are significant. The extensive parametric studies on the radiative and conductive wall fluxes have demonstrated that the magnitude of the radiative and conductive wall fluxes are very sensitive to the equivalence ratio when the equivalence ratio is less than 1.0 but they are less sensitive when the equivalence ratio is higher than 1.0. The change in the wall temperature has little effect on the combustion. Thus, the radiative wall flux is decreased with increases in wall temperature. But the conductive wall flux seems insensitive to changes in wall temperature. The radiative wall flux does not change monotonically with inlet flow temperature. Lower inlet flow temperature can yield higher radiative wall flux. The conductive wall flux, however, increases with an increase in the inlet flow temperature. The radiative wall flux decreases but the conductive wall flux increases with a reduction in nozzle size. For larger nozzles, the radiative wall flux is dominant over the conductive wall flux. However, the situation can be reversed when the nozzle size is reduced.

## REFERENCES

1. Kumar, A., 1986, "Numerical Simulation of Scramjet Inlet Flowfield," NASA TP-25117, May 1986.
2. Drummond, J. P., Hussaini, M. Y. and Zang, T. A., 1986, "Spectral Methods for Modelling Supersonic Chemically Reacting Flowfields," AIAA Journal, Vol. 24, No. 9, September 1986, pp. 1461-1467.
3. Drummond, J. P., Rogers, R. C., and Hussaini, M. Y., 1986, "A Detailed Numerical Model of a Supersonic Reacting Mixing Layer," AIAA Paper 86-1427, June 1986.
4. Chitsomboon, T., Kumar, A., Drummond, J. P., and Tiwari, S. N., 1986, "Numerical Study of Supersonic Combustion Using a Finite-rate Chemistry Model," AIAA Paper 86-0309, January 1986.
5. Tiwari, S. N., 1985, "Radiative Interaction in Transient Energy Transfer in Gaseous System," NASA CR-176644, December, 1985.
6. Siegel, R., and Howell, J. R., 1992, Thermal Radiation Heat Transfer, Third Edition, McGraw-Hill Inc., New York, 1992.
7. Modest, M. F., 1992, Radiative Heat Transfer, McGraw-Hill Inc., New York, 1992.
8. Sparrow, E. M., and Cess, R. D., 1978, Radiation Heat Transfer, Augmented Edition, McGraw-Hill Inc., New York, 1978.
9. Cess, R. D. and Tiwari, S. N., 1972, "Infrared Radiative Energy Transfer in Gases," Advances in Heat Transfer, Vol. 8, Academic Press, New York, 1972.
10. Edwards, D. K., 1976, "Molecular Gas Band Radiation," Advances in Heat Transfer, Vol. 12, Academic Press, New York, 1976.
11. Howell, J. R., 1983, "Radiative Transfer in Multidimensional Enclosures with Participating Media," ASME Paper 83-HT-32, 1983.
12. Howell, J. R., 1988, "Thermal Radiation in Participating Media: The Past, the Present, and Some Possible Futures," Journal of Heat Transfer, Vol. 110, November 1988, pp. 1220-1229.
13. Goody, R. M., 1964, Atmospheric Radiation, Oxford Press, London, pp. 234-243, 1964.

14. Chan, S. H. and Tien, C. L., 1969, "Total Band Absorptance of Nonisothermal Infrared Radiation Gases," Journal of Quantitative Spectroscopy and Radiative Transfer, Vol. 9, 1969, pp. 1261-1271.
15. Edwards, D. K. and Morizumi, S. J., 1970, "Scaling of Vibration-Rotation Band Parameters for Nonhomogeneous Gas Radiation," Journal of Quantitative Spectroscopy and Radiative Transfer, Vol., 1970, pp. 175-188.
16. Chan, S. H., 1987, "Numerical Methods for Multidimensional Radiative Transfer Analysis in Participating Media," in: Annual Review of Numerical Fluid Mechanics and Heat Transfer, T. C. Chawla, ed., Hemisphere, Washington, D. C., Chapter 6.
17. Howell, J. R., and Perlmutter, M., 1964, "Monte Carlo Solution of Thermal Transfer through Radiant Media between Gray Walls," Journal of Heat Transfer, Vol. 86, February 1964, pp. 116-122.
18. Perlmutter, M. and Howell, J. R., 1964, "Radiative Transfer through a Gray Gas between Concentric Cylinders Using Monte Carlo," Journal of Heat Transfer, Vol. 86, May 1964, pp. 169-179.
19. Howell, J. R., and Perlmutter, M., 1964, "Monte Carlo Solution of Radiant Heat Transfer in a Nongray Nonisothermal Gas with Temperature Dependent Properties," American Institute of Chemical Engineers Journal, Vol. 10, No. 4, July 1964, pp. 562-567.
20. Steward, F. R., and Cannon, P., 1971, "The Calculation of Radiative Heat Flux in a Cylindrical Furnace Using the Monte Carlo Method," International Journal of Heat and Mass Transfer, Vol. 14, No. 2, February 1971, pp. 245-262.
21. Dunn, W. L., 1983, "Inverse Monte Carlo Solutions for Radiative Transfer in Inhomogeneous Media," Journal of Quantitative Spectroscopy and Radiative Transfer, Vol. 29, No. 1, January 1983, pp. 19-26.
22. Gupta, R. P., Wall, T. F., and Truelove, J. S., 1983, "Radiative Scatter by Fly Ash in Pulverized-Coal-Fired Furnaces: Application of the Monte Carlo Method to Anisotropic Scatter," International Journal of Heat and Mass Transfer, Vol. 26, No. 11, November 1983, pp. 1649-1660.
23. Kobiyama, M., Taniguchi, H., and Saito, T., 1979, "The Numerical Analysis of Heat Transfer Combined with Radiation and Convection," Bulletin of the Japan Society of Mechanical Engineers, Vol. 22, No. 167, May 1979, pp. 707-714.
24. Kobiyama, M., 1986, "A Study on the Reduction of Computing Time of the Monte Carlo Method Applied to the Radiative Heat Transfer," Bulletin of the Japan Society of Mechanical Engineers, Vol. 29, No. 255, September 1986, pp. 3000-3006.

25. Taniguchi, H., Kudo, K., Otaka, M., Sumarsono, M., and Obata, M., 1991, "Non-gray Analysis on Radiative Energy Transfer through Real Gas Layer by Monte Carlo Method," Proceedings of the 7th International Conference on Numerical Methods of Thermal Problems.
26. Farmer, J. F., and Howell, J. R., 1992, "Monte Carlo Solution of Radiative Heat Transfer in a Three-dimensional Enclosure with an Anisotropically Scattering, Spectrally Dependent, Inhomogeneous Medium," Proceedings of the 28th National Heat Transfer Conference, San Diego, California, ASME HTD-Vol. 203, August 1992, pp. 301-309.
27. Modest, 1992, "The Monte Carlo Method Applied to Gases with Spectral Line Structure," Proceedings of the 28th National Heat Transfer Conference, San Diego, California, ASME HTD-Vol. 203, August 1992, pp. 79-84.
28. Zhang, L., Soufiani, A., and Taine, J., 1988, "Spectral Correlated and Non-correlated Radiative Transfer in a Finite Axisymmetric System Containing an Absorbing and Emitting Real Gas-particle Mixture," International Journal of Heat and Mass Transfer, Vol. 31, No. 11, November 1988, pp. 2261-2272.
29. Kim, T. K., Menart, J. A., and Lee, H. S., 1991, "Nongray Radiative Gas Analyses Using the S-N Discrete Ordinates Method," Journal of Heat Transfer, Vol. 113, November 1991, pp. 946-952.
30. Mani, M. and Tiwari, S. N., 1988, "Investigation of Supersonic Chemically Reacting and Radiating Channel Flow," NASA CR-182726, January, 1988.
31. Tiwari, S. N., Chandrasekhar, R., Thomas, A. M. and Drummond, J. P., 1991, "Investigation of Chemically Reacting and Radiating Supersonic Internal Flows," AIAA Paper 91-0572, January 1991.
32. McClatchey, R. A., Benedict, W. S., Clough, S. A., Burth, D. E., Calfee, R. F., Fox, K., Rothman, L. S., and Garing, J. S., 1973, "AFCRL Atmospheric Line Parameters Compilation," Air Force Cambridge Research Laboratories, Bedford, Massachusetts, AFCRL-TR-0096, January 1973.
33. Ludwig, C. B., Malkmus, W., Reardon, J. E., and Thompson, J. A. L., 1973, "Handbook of Infrared Radiation from Combustion Gases," NASA SP-3080.
34. Ludwig, C. B. (editor), 1979, Atmospheric Effects on Radiative Transfer, Proceedings of the Society of Photo-Optical Instrumentation Engineers, Vol. 195, August 1979.
35. Tien, C. L., 1968, "Thermal Radiation Properties of Gases," Advances in Heat Transfer, Vol. 5, Academic Press, New York, 1968.

36. Tiwari, S. N., 1976, "Band Models and Correlations for Infrared Radiation," Radiative Transfer and Thermal Control (Progress in Astronautics and Aeronautics), Vol. 49, American Institute of Aeronautics and Astronautics, New York, 1976.
37. Tiwari, S. N., 1978, "Models for Infrared Atmospheric Radiation," Advances in Geophysics, Vol. 20, Academic Press, New York, 1978.
38. Plass, G. N., 1958, "Models for Spectral Band Absorption," Journal of the Optical Society of America, Vol. 48, No. 10, October 1958, pp. 690-703.
39. Plass, G. N., 1960, "Useful Representation for Measurements of Spectral Band Absorption," Journal of the Optical Society of America, Vol. 50, No. 9, September 1960, pp. 868-875.
40. Wyatt, P. J., Stull, V. R., and Plass, G. N., 1962, "Quasi-Random Model of Band Absorption," Journal of the Optical Society of America, Vol. 52, No. 11, November 1962, pp. 1209-1217.
41. Edwards, D. K. and Menard, W. A., 1964, "Comparison of Models for Correlation of Total Band Absorption," Applied Optics, Vol. 3, No. 5, May 1964, pp. 621-625.
42. Edwards, D. K., Glassen, L. K., Hauser, W. C., and Tucher, J. S., 1967, "Radiation Heat Transfer in Nonisothermal Nongray Gases," Journal of Heat Transfer, Vol. 89C, No. 3, 1967, pp. 219-229.
43. Edwards, D. K. and Balakrishnan, A., 1972, "Slab Band Absorptance for Molecular Gas Radiation," Journal of the Quantitative Spectroscopy and Radiative Transfer, Vol. 12, 1972, pp. 1379-1387.
44. Edwards, D. K. and Balakrishnan, A., 1973, "Thermal Radiation by Combustion Gases," International Journal of Heat and Mass Transfer, Vol. 16, No. 1, January 1973, pp. 25-40.
45. Felske, J. D. and Tien, C. L., 1974, "A Theoretical Closed Form Expression for the Total Band Absorptance of Infrared Radiating Gases," International Journal of Heat and Mass Transfer, Vol. 17, No. 1, January 1974, pp. 155-158.
46. Tien, C. L. and Ling, G. R., 1969, "On a Simple Correlation for Total Band Absorptance of Radiating Gases," International Journal of Heat and Mass Transfer, Vol. 12, No. 9, September 1969, pp. 1179-1181.
47. Tiwari, S. N., 1977, "Applications of Infrared Band Model Correlations to Nongray radiation," International Journal of Heat and Mass Transfer, Vol. 20, No. 7, July 1977, pp. 741-751.

48. Soufiani, A., Hartmann, J. M., and Taine, J., 1985, "Validity of Band-model Calculation for CO<sub>2</sub> and H<sub>2</sub>O Applied to Radiative Properties and Conductive-radiative Transfer," Journal of Quantitative Spectroscopy and Radiative Transfer, Vol. 33, No. 3, March 1985, pp. 243-257.
49. Soufiani, A., and Taine, J., 1987, "Application of Statistical Narrow-band Model to Coupled Radiation and Convection at High Temperature," International Journal of Heat and Mass Transfer, Vol. 30, No. 3, March 1987, pp. 437-447.
50. Malkmus, W., 1967, "Random Lorentz Band Model with Exponential-tailed S<sup>-1</sup> Line-intensity Distribution Function," Journal of the Optical Society of America, Vol. 57, No. 3, March 1967, pp. 323-329.
51. Hartmann, J. M., Levi Di Leon, R., and Taine, J., 1984, "Line-by-line and Narrow-band Statistical Model Calculations for H<sub>2</sub>O," Journal of Quantitative Spectroscopy and Radiative Transfer, Vol. 32, No. 2, February 1984, pp. 119-127.
52. Tien, C. L. and Lowder, J. G., 1966, "A Correlation for Total Band Absorptance of Radiating Gases," International Journal of Heat and Mass Transfer, Vol. 9, No. 7, July 1966, pp. 698-701.
53. Godson, W. L., 1953, "The Evaluation of Infrared Radiation Fluxes Due to Atmospheric Water Vapor," Quarterly Journal of Royal Meteorological Society, Vol. 79, 1953, pp. 367-379.
54. Howell, J. R., 1968, "Application of Monte Carlo to Heat Transfer Problems," Advances in Heat Transfer, Vol. 5, Academic Press, New York.
55. Haji-Sheikh, A., 1988, "Monte Carlo Methods," in: Handbook of Numerical Heat Transfer, W. J. Minkowycz, E. M. Sparrow, G. E. Schneider and R. H. Pletcher, eds., Wiley, New York, Chapter 16.
56. Menart, J. A., Lee, H. S., and Kim, T. K., 1993, "Discrete Ordinates Solutions of Nongray Radiative Transfer with Diffusely Reflecting Walls," Journal of Heat Transfer, Vol. 115, February 1993, pp. 184-193.
57. Nelson, D. A., 1979, "Band Radiation within Diffuse-Walled Enclosures, Part I: Exact Solutions for Simple Enclosures," Journal of Heat Transfer, Vol. 101, February 1979, pp. 81-84.
58. Nelson, D. A., 1979, "Band Radiation within Diffuse-Walled Enclosures, Part II: An Approximate Method Applied to Simple Enclosures," Journal of Heat Transfer, Vol. 101, February 1979, pp. 85-89.

59. Rubenstein, R. Y., 1981, Simulation and Monte Carlo Method, Wiley, New York, 1981.
60. Binder, K., 1984, Application of the Monte Carlo Method in Statistical Physics, Springer-Verlag, Berlin, 1984.
61. Hammersley, J. M. and Handscomb, D. C., 1964, Monte Carlo Methods, Methuen, London, 1964.
62. Feller, W., 1964, An Introduction to Probability Theory and its Applications, Wiley, New York, 1964
63. Brown, G., 1956, "Monte Carlo Methods," in: Modern Mathematics for the Engineer, E. F. Beckenbach, ed., McGraw-Hill Book Co., New York, 1956.
64. Kim, T. K., Menart, J. A., and Lee, H. S., 1991, "S-N Discrete Ordinates Solutions of Nongray Radiative Transfer with Diffusely Reflecting Walls," Proceedings of the 28th National Heat Transfer Conference, Minneapolis, Minnesota, ASME HTD-Vol. 160, July 1991, pp. 79-87.
65. Tiwari, S. N., Singh, D. J. , and Trivedi, P. A., 1990, "Radiative Interactions in Laminar Incompressible and Compressible Internal Flows", AIAA Paper 90-0134, January 1990.
66. Kobiyama, M., Taniguchi, H. ,and Saito, T., 1979, "The Numerical Analysis of Heat Transfer Combined with Radiation and Convection", Bulletin of the Japan Society of Mechanical Engineers, Vol. 22, No. 167, May 1979, pp. 707-714.
67. Kobiyama, M., 1986, "A study on the Reduction of Computing Time of the Monte Carlo Method Applied to the Radiative Heat Transfer", Bulletin of the Japan Society of Mechanical Engineers, Vol. 29, No. 255, September 1986, pp. 3000-3006.
68. Anonymous, 1987, IMSL MATH/LIBRARY Reference Manual, IMSL, Inc., Houston, TX.
69. Krishnamurthy, R., Tiwari, S. N., and Liu, J., 1994, "Investigation of Entry Region Turbulent Flows of Nongray Gases," Heat and Mass Transfer 94 (Heat Transfer in Fires and Flame): Proceeding of the First ISHMT-ASME Heat and Mass Transfer Conference, January 5-7, Bombay, India; Vedams Books International, New Delhi, India, 1994.
70. Bird, R. B., Stewart, W. E. and Lightfoot, E. N., 1960, Transport Phenomena, John Wiley & Sons, New York, 1960.



71. McBride, B. J., Heimel, S., Ehlers, J. G. and Gordon, S., 1963, "Thermodynamic Properties to 6000 °K for 210 Substances Involving the First 18 Elements," NASA SP-3001, 1963.
72. White, F. M., 1974, Viscous Fluid Flow, McGraw-Hill Inc., New York, 1974.
73. Suehla, R. A. 1962, "Estimated Viscosities and Thermal Conductivities of Gases at High Temperatures," NASA TR R-132, 1962
74. Wilke, C. R., 1950, "A Viscosity Equation for Gas Mixtures," Journal of Chemical Physics, Vol. 18, No. 4, 1950, pp. 517-519.
75. Berman, H. A., Anderson, J. D. and Drummond, J. P., 1983, "Supersonic Flow over a Rearward Facing Step with Transverse Non-reacting Hydrogen Injection," AIAA Journal, Vol. 21, No. 12, December 1983, pp. 1707-1713.
76. Baldwin, B. S. and Lomax, H., 1978, "Thin Layer Approximation and Algebraic Model for Turbulent Flows," AIAA Paper 78-257, January, 1978.
77. Cebeci, T. and Bradshaw, P., 1984, Physical and Computational Aspects of Heat Transfer, Springer-Verlag , New York, 1984.
78. Anderson, J. D., 1989, Hypersonic and High Temperature Gas Dynamics, McGraw-Hill Inc., New York, 1989.
79. Smith, R. E. and Weigel, B. L., 1980, "Analytical and Approximate Boundary Fitted Coordinate System for Fluid Flow Simulation," AIAA Paper 80-0192, January 1980.
80. Bussing, T. R. A. and Murman, E. M., 1985, "A Finite Volume Method for Calculation of Compressed Chemically reacting Flows," AIAA Paper 85-0331, January 1985.
81. Householder, A. S., 1964, The Theory of Matrices in Numerical Analysis, Dover Publications, New York, 1964.
82. MacCormack, R. W., 1969, "The Effect of Viscosity in Hypervelocity Impact Cratering," AIAA Paper 69-354, April 1969.
83. Anderson, D. A., Tannehill, J. C., and Pletcher, R. H., 1984, Computational Fluid Mechanics and Heat Transfer, McGraw-Hill Inc., New York, 1984.
84. Li, C. P., 1971, "Time Dependent Solutions of Nonequilibrium Air Past a Blunt Body," AIAA Paper 71-595, June 1971.
85. Pulliam, T. H., 1985, "Artificial Dissipation Models for the Euler Equations," AIAA Paper 85-0438.

86. Singh, D. J., Carpenter, M. H., and Kumar, A., 1991, "Numerical Simulation of Shock-Induced Combustion/Detonation in a Premixed  $H_2$ -Air Mixture Using Navier-Stokes Equations," AIAA Paper 91-3358, June 1991.
87. Carpenter, M. H., 1988, "A Generalized Chemistry Version of SPARK," NASA CR-4196, 1988.

**APPENDICES**

## APPENDIX A:

### PROGRAM LISTING FOR MONTE CARLO SIMULATION

This code is developed to calculate radiative source distribution and net radiative wall flux in a one-dimensional problem. A lot of subroutines in the code are from the IMSL library. The spectral correlation has been taken into account. Input files consist of parameter statement file "param.inc", common statement file "common.inc", and three narrow band information files "y.dat", "fibig.dat", and "f2big.dat". Temperature, pressure, and concentration distributions should be also given before calculation.

```

program moncar

include 'paramm.inc'

include 'commonm.inc'

parameter (mx=22,mz=22)

external gamfun,bs2vl,funtao

real rwksp(20000),tarray(2),len(3)

dimension rf(mx),t2(mx),xl(mx)

dimension sg(mx),sq(mx),nn(mx),em(3)

dimension xp(mx),zp(mz),tm(mx,mz)

common/cgas/p,xh2o,xn2,xo2,xco2,dlx

common/worksp/ rwksp

common/ct/tp

data xh2o,xn2,xo2,xco2/1.0,0.0,0.0,0.0/

data em/0.90,0.8,0.1/

data len/1.0,60.,100.0/

```

```

c open(unit=4,file="tinbig.dat")

  open(unit=5,file="tout.dat")

  call iwkin(20000)

  call coefbs

c read(4,*) (t2(i),i=1,mx)

  dlx=1.0/float(mx-2)

  dlz=1.0/float(mz-2)

  xp(1)=0.0

  xp(2)=0.5*dlx

  xp(mx)=1.0

  zp(1)=0.0

  zp(2)=0.5*dlz

  zp(mz)=1.0

  do 1 i=3,mx-1
1  xp(i)=xp(i-1)+dlx

  do 2 j=3,mz-1
2  zp(j)=zp(j-1)+dlz

  do 3 i=1,mx

  do 3 j=1,mz

    tm(i,j)=500.0+500.0*(1.0-(2.0*zp(j)-1.0)**2)*xp(i)

3  continue

  do 303 j=1,mz

    tm(mx,j)=300.0

303 continue

  do 999 i9=3,mx,2

```

```
do 304 j=1,mz
  t2(j)=tm(i9,j)
304 continue

time1=etime(tarray)

pi=3.1415926

n=100000

p=1.0

do 910 i1=2,2
  e1=em(i1)
  e2=em(i1)
do 900 i2=2,2
  alx=len(i2)
  dlx=alx/(real(mx)-2.0)
  nran=15249649
  call rnset (nran)
  sum=0.0
do 20 i=1,mx
  rf(i)=0.0
  sg(i)=0.
20 sq(i)=0.0

  xl(2)=0.5/(real(mx)-2.0)
do 5 i=2,mx-1
  xl(i)=xl(2)+float(i-2)/(real(mx)-2.0)
  t=t2(i)
  call baneng(t,1)
```

```
sq(i)=qv
sum=sum+sq(i)
5 continue
t=t2(1)
call surwc(t)
sq(1)=sqw*e1
sq(mx)=sqw*e2
sum=sum+sq(1)+sq(mx)
sqm=sum/float(n)
do 13 i=1,mx
nn(i)=ifix(sq(i)/sqm+0.5)
13 continue
is1=1
ntt=0
nt=0
23 go to (30,31,36,120),is1
30 it=1
go to 39
31 it=mx
go to 39
36 it=2
38 t=t2(it)
gamma=gamfun(t)
call baneng(t,2)
39 is2=is1
```

```
ar=rnunf()
go to (40,41,45),is1
40 ran=rnunf()
   ran=ws1+ran*(ws2-ws1)
   waveno=bsval(ran,kxord,xks1,nxd1,bss1)
   go to 471
41 ran=rnunf()
   ran=ws1+ran*(ws2-ws1)
   waveno=bsval(ran,kxord,xks1,nxd1,bss1)
   go to 471
45 ran=rnunf()
   waveno=bsval(ran,kxord,xkv1,nxd1,bsv1)
47 park=bs2vl(waveno,t,kxord,kyord,xk1,yk1,nxd1,
+nyd1,bscol1)
   pardlt=bs2vl(waveno,t,kxord,kyord,xk1,yk1,nxd1,
+nyd1,bscol2)
471 nt=nt+1
   i=it
   go to (48,48,49),is1
48 u=0.0
   sumk=0.0
   sumb=0.0
   go to 50
49 ran1=rnunf()
   if(ran1.gt.0.5) go to 491
```



```

    rx=bsval(ran1,kxord,xkb1,nb,bsb1)
    go to 492
491 ran1=1.0-ran1
    rx=-bsval(ran1,kxord,xkb1,nb,bsb1)
492 rx1=dlx/abs(rx)
    u=xh2o*p*rx1
    beta=2.0*gamma*pardlt
    ar=(1.0-funtao(u,park,beta))*ar
    u1=0.0
    sumk1=0.0
    sumb1=0.0
    us=u
    sumks=park*u
    sumbs=sumks*beta
    if(rx.lt.0.) go to 496
494 i=i+1
    if(i.gt.(mx-1)) go to 80
    ta=t2(i)
    gama=gamfun(ta)
    park=bs2vl(waveno,ta,kxord,kyord,xk1,yk1,nxd1,
    +nyd1,bsco11)
    pardlt=bs2vl(waveno,ta,kxord,kyord,xk1,yk1,nxd1,
    +nyd1,bsco12)
    deltu=p*rx1*xh2o
    u1=u1+deltu

```

```

sumk1=sumk1+park*deltu
sumb1=sumb1+park*deltu*2.0*gama*pardlt
u2=u1+us
sumk2=sumk1+sumks
sumb2=sumb1+sumbs
efk1=sumk1/u1
efb1=sumb1/u1/efk1
efk2=sumk2/u2
efb2=sumb2/u2/efk2
dtao=funtao(u1,efk1,efb1)-funtao(u2,efk2,efb2)
if(dtao.lt.ar) go to 85
go to 494
496 i=i-1
if(i.lt.2) go to 79
ta=t2(i)
gama=gamfun(ta)
park=bs2vl(waveno,ta,kxord,kyord,xk1,yk1,nxd1,
+nyd1,bscol1)
pardlt=bs2vl(waveno,ta,kxord,kyord,xk1,yk1,nxd1,
+nyd1,bscol2)
deltu=p*rx1*xh2o
u1=u1+deltu
sumk1=sumk1+park*deltu
sumb1=sumb1+park*deltu*2.0*gama*pardlt
u2=u1+us

```

```

sumk2=sumk1+sumks
sumb2=sumb1+sumbs
efk1=sumk1/u1
efb1=sumb1/u1/efk1
efk2=sumk2/u2
efb2=sumb2/u2/efk2
dtao=funtao(u1,efk1,efb1)-funtao(u2,efk2,efb2)
if(dtao.lt.ar) go to 85
go to 496
50 ran1=rnunf()
go to (54,55),is2
54 rx=sqrt(1.-ran1)
541 i=i+1
if(i.gt.(mx-1)) go to 80
ta=t2(i)
gama=gamfun(ta)
park=bs2vl(waveno,ta,kxord,kyord,xk1,yk1,nxd1,
+nyd1,bsco11)
pardlt=bs2vl(waveno,ta,kxord,kyord,xk1,yk1,nxd1,
+nyd1,bsco12)
deltu=p*xh2o*dlx/rx
go to (543,543,544),is1
543 u=u+deltu
sumk=sumk+park*deltu
sumb=sumb+park*deltu*2.0*gama*pardlt

```

```

    efk=sumk/u
    efb=sumb/u/efk
    tao=funtao(u,efk,efb)
    if(tao.lt.ar) go to 85
    go to 541
544 u1=u1+deltu
    sumk1=sumk1+park*deltu
    sumb1=sumb1+park*deltu*2.0*gama*pardlt
    u2=u1+us
    sumk2=sumk1+sumks
    sumb2=sumb1+sumbs
    efk1=sumk1/u1
    efb1=sumb1/u1/efk1
    efk2=sumk2/u2
    efb2=sumb2/u2/efk2
    dtao=funtao(u1,efk1,efb1)-funtao(u2,efk2,efb2)
    if(dtao.lt.ar) go to 85
    go to 541
55 rx=-sqrt(1.-ran1)
551 i=i-1
    if(i.lt.2) go to 79
    ta=t2(i)
    gama=gamfun(ta)
    park=bs2vl(waveno,ta,kxord,kyord,xk1,yk1,nxd1,
    +nyd1,bscol1)

```

```
pardlt=bs2vl(waveno,ta,kxord,kyord,xk1,yk1,nxd1,  
+nyd1,bsco12)  
deltu=-p*xh2o*dlx/rx  
go to (553,553,554),is1  
553 u=u+deltu  
sumk=sumk+park*deltu  
sumb=sumb+park*deltu*2.0*gama*pardlt  
efk=sumk/u  
efb=sumb/u/efk  
tao=funtao(u,efk,efb)  
if(tao.lt.ar) go to 85  
go to 551  
554 u1=u1+deltu  
sumk1=sumk1+park*deltu  
sumb1=sumb1+park*deltu*2.0*gama*pardlt  
u2=u1+us  
sumk2=sumk1+sumks  
sumb2=sumb1+sumbs  
efk1=sumk1/u1  
efb1=sumb1/u1/efk1  
efk2=sumk2/u2  
efb2=sumb2/u2/efk2  
dtao=funtao(u1,efk1,efb1)-funtao(u2,efk2,efb2)  
if(dtao.lt.ar) go to 85  
go to 551
```

```
79 is2=1
    go to 86
80 is2=2
    go to 86
85 is2=3
86 go to (90,91,110),is2
90 i=1
    go to 92
91 i=mx
92 ran=rnunf()
    if((is2.eq.1.and.ran.gt.e1).or.(is2.eq.2.and.ran.gt.e2))
    +go to 50
    sg(i)=sg(i)+sqm
59 if(nt.lt.abs(nn(it))) go to 39
    ntt=ntt+nt
    nt=0
102 if(is1.ne.3) go to 104
    it=it+1
    if(it.le.(mx-1)) go to 38
104 is1=is1+1
    go to 23
110 sg(i)=sg(i)+sqm
    go to 59
120 call sub200(sg,mx)
    qw1=-(sq(1)-sg(1))*0.001
```

```

qw2=-(sq(mx)-sg(mx))*0.001

write(5,25) e1,e2,alx,n

25 format(1x,'e1=',f6.3,2x,'e2=',f6.3,2x,'x=',f9.3,2x,'n=',i9/)

write(5,26) qw1,qw2

26 format(1x,'qw1=',f15.6,4x,'qw2=',f15.6/)

do 130 i=2,mx-1

rf(i)=-sg(i)+sq(i)

rf(i)=-rf(i)/dlx*0.1

write(5,27) xl(i),rf(i)

27 format(1x,f15.6,4x,f15.6)

130 continue

time2=etime(tarray)

time=time2-time1

write(5,390) time

390 format(1x,'cpu time spent =',f9.3////)

900 continue

910 continue

999 continue

stop

end

c

c

subroutine coefbs

external bs2in,bsnak

include 'paramm.inc'

```

```

include 'commonm.inc'

dimension fd11(nxd1,nyd1),fd12(nxd1,nyd1),yd1(nyd1)

open(unit=7,file="y.dat")

open(unit=8,file="f1big.dat")

open(unit=9,file="f2big.dat")

read(7,*) (yd1(i),i=1,nyd1)

read(8,*) (i,xd1(i),(fd11(i,j),j=1,nyd1),i=1,nxd1)

read(9,*) (i,xd1(i),(fd12(i,j),j=1,nyd1),i=1,nxd1)

call bsnak(nxd1,xd1,kxord,xk1)

call bsnak(nyd1,yd1,kyord,yk1)

call bs2in(nxd1,xd1,nyd1,yd1,fd11,ldf1,kxord,
+kyord,xk1,yk1,bscol1)

call bs2in(nxd1,xd1,nyd1,yd1,fd12,ldf1,kxord,
+kyord,xk1,yk1,bscol2)

return

end

c

c

subroutine baneng(t,iflag)

include 'paramm.inc'

include 'commonm.inc'

external planck,gamfun,bs2vl,emicoe,bsint

dimension bre1(nxd1),cpmul(nxd1,nb)

dimension tgl(nxd1)

common/cgas/p,xh2o,xn2,xo2,xco2,dlx

```



```

common/cpar/gamma,park,pardlt
common/ct/tp
eps=1.0e-03
gamma=gamfun(t)
tp=t
delomg=xd1(2)-xd1(1)
dmu=1.0/float(nb-1)
do 5 i=1,nb
mu(i)=1.0-dmu*float(i-1)
5 continue
do 30 i=1,nxd1
x=xd1(i)
r=planck(x)
park=bs2vl(x,t,kxord,kyord,xk1,yk1,nxd1,
+nyd1,bscol1)
pardlt=bs2vl(x,t,kxord,kyord,xk1,yk1,nxd1,
+nyd1,bscol2)
go to (25,10) iflag
10 do 15 j=1,nb
xa=mu(j)
call qdags(emicoe,1.0,xa,eps,eps,r1,err)
cpmul(i,j)=2.0*r1*r*delomg
15 continue
25 call qdags(emicoe,1.0,0.0,eps,eps,r1,err)
bre1(i)=4.0*r1*r*delomg

```

```
30 continue
    qv=0.0
    do 40 i=1,nxd1
        qv=qv+brel(i)
40 continue
    go to (50,55) iflag
50 go to 99
55 eps4=1.0e-7
    d=brel(1)
    tg1(1)=0.0
    do 60 i=2,nxd1
        d=d+brel(i)
        tg1(i)=d/qv
        if(((tg1(i)-tg1(i-1)).le.eps4) tg1(i)=tg1(i-1)+eps4
60 continue
    call bsnak(nxd1,tg1,kxord,xkv1)
    call bsint(nxd1,tg1,xd1,kxord,xkv1,bsv1)
    do 70 j=1,nb
        cpmu(j)=0.0
        do 80 i=1,nxd1
            cpmu(j)=cpmu(j)+cpmul(i,j)
80 continue
    cpmu(j)=cpmu(j)/qv
70 continue
    call bsnak(nb,cpmu,kxord,xkb1)
```

```

    call bsint(nb,cpmu,mu,kxord,xkb1,bsb1)

99 return

    end

c

c

    function emicoe(x)

    common/cgas/p,xh2o,xn2,xo2,xco2,dlx

    common/cpar/gamma,park,pardlt

    eti=sqrt(1.0+xh2o*p*dlx*park/gamma/pardlt/x)-1.0

    tao=exp(-2.0*gamma*pardlt*eti)

    emicoe=-(1.0-tao)*x

    return

    end

    function gamfun(t)

    common/cgas/p,xh2o,xn2,xo2,xco2,dlx

    ts=296.0

    gamfun=0.066*p*(7.0*xh2o*ts/t+sqrt(ts/t)*(1.2*(xh2o+xn2)+
    +0.8*xo2+1.6*xco2))

    return

    end

c

c

    subroutine surwc(t)

    include 'paramm.inc'

    include 'commonm.inc'

```

```

external planck,bsint,qdags

dimension t1(nxd1)

common/ct/tp

eps=1.0e-04

x1=99999.0

s=5.6696e-08

power=s*t**4

tp=t

call qdags(planck,0.0,xd1(1),eps,eps,r1,err)

call qdags(planck,0.0,xd1(nxd1),eps,eps,r2,err)

sqw=r2-r1

ws1=r1/power

ws2=r2/power

eps4=1.0e-7

t1(1)=ws1

do 10 i=2,nxd1

x=xd1(i)

call qdags(planck,0.0,x,eps,eps,re,err)

t1(i)=re/power

if(t1(i).le.t1(i-1)) t1(i)=t1(i-1)+eps4

10 continue

call bsnak(nxd1,t1,kxord,xks1)

call bsint(nxd1,t1,xd1,kxord,xks1,bss1)

return

end

```

c

c

```
function planck(x)
```

```
common/ct/tp
```

```
c1=3.740e-08
```

```
c2=1.4387
```

```
planck=c1*x**3/(exp(c2*x/tp)-1.0)
```

```
return
```

```
end
```

```
function funtao(u,park,beta)
```

```
funtao=exp(-beta*(sqrt(1.0+2.0*u*park/beta)-1.0))
```

```
return
```

```
end
```

c

c

```
subroutine sub200(sg,mx)
```

```
dimension sg(990)
```

```
ms=(mx+1)/2
```

```
do 210 i=1,ms
```

```
is=mx-i+1
```

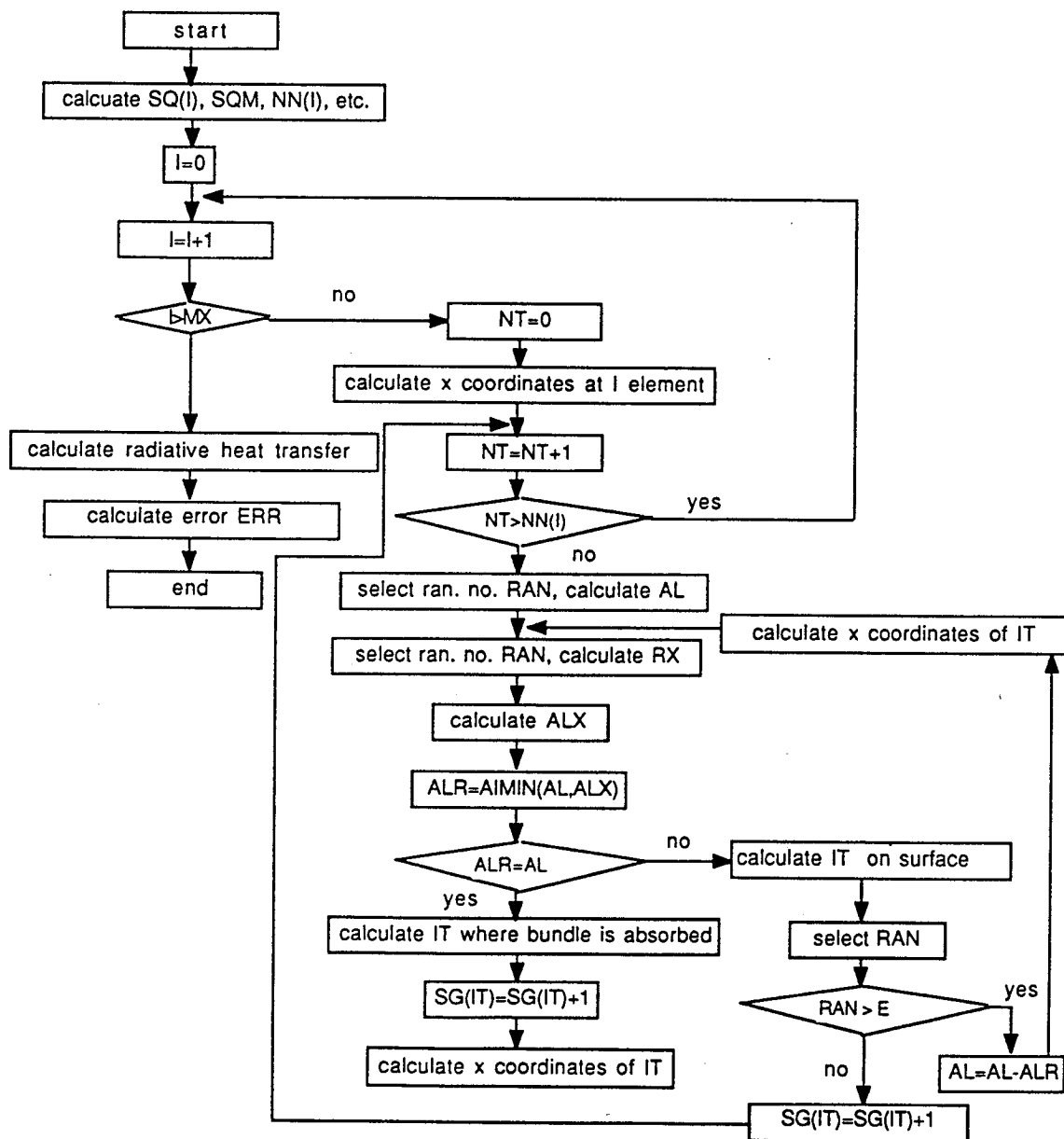
```
sg(i)=(sg(i)+sg(is))/2.
```

```
210 sg(is)=sg(i)
```

```
240 return
```

```
end
```

## COMPUTER FLOW CHART FOR APPENDIX A



**APPENDIX B:**  
**PROGRAM LISTING FOR RADIATIVE INTERACTIONS**  
**IN LAMINAR FLOWS USING MONTE CARLO SIMULATION**

This code is developed to investigate the radiative interactions in laminar flows between two parallel plates. The Monte Carlo simulation subroutine "moncar" used here is the same as given in Appendix A.

```

program mcom
include 'param.inc'
include 'common.inc'
parameter (mx=100,n=20)
real rwksp(20000),tarray(2)
external fcn,neqnf
dimension q(n),tn(mx),te(mx),qgr(n)
dimension ald(10),qtd(3),temper(4),pres(4)
common /a1/qly,aky,h,alx,tw,q,qgr
common/worksp/ rwksp
common/cgas/p,xh2o,xn2,xo2,xco2,dlx
data xh2o,xn2,xo2,xco2/1.0,0.0,0.0,0.0/
data w/0.5/,eps/1.0e-04/
data pres/1.0,1.0,5.0,10.0/
data temper/300.0,500.0,1000.0,2000.0/
data qtd/1.0e06,5.0e05,1.0e07/
data ald/0.01,0.05,0.1,0.5,1.0,5.0,10.0,20.0,50.0,100.0/

```

```
open(unit=5,file="ngput.dat")
call iwkin(20000)
call coefbs
n1=50000
errrel=1.0e-03
itmax=50
e=1.0
time1=etime(tarray)
do 599 ii=1,1
p=pres(ii)
do 690 ij=2,2
tw=temper(ij)
fb = (4186.8/360*130.)*((tw/273.0)**1.48)
do 691 it=2,2
qt=qtd(it)
do 692 kk=6,6
alx=ald(kk)
h=alx/(real(2*n)-1.0)
dlx=h
qly=12.0*qt*h/(1000.0*alx)
aky=fb/h/1000.0
qrt=qt*alx/fb
iter=0
sumt=0.0
sumt1=0.0
```



```

write(5,1) n1,n,alx,tw,p,qt
1 format(//1x,'n1=',i10,1x,'n=',i3,2x,'alx=',f9.3,
*2x,1x,'tw=',f9.3,2x,'p=',f6.2,2x,'qt=',1pe9.3)
do 3 i=1,n
tn(i)=tw
3 continue
tn(1)=tw
99 iter=iter+1
if(iter.gt.21) go to 98
timea=etime(tarray)
call moncar(n1,n,alx,e,tn,q)
timeb=etime(tarray)
delt=timeb-timea
sumt=sumt+delt
do 4 i=1,n
te(i)=tn(i)
call baneng(te(i),1)
qgr(i)=qv
4 continue
timea1=etime(tarray)
call neqnf(fcn,errrel,n,itmax,te,tn,fnorm)
timeb1=etime(tarray)
delt1=timeb1-timea1
sumt1=sumt1+delt1
do 6 i=1,n

```

```

    tn(i)=(1.0-w)*te(i)+w*tn(i)
6  continue
    do 7 i=1,n
        if(abs((tn(i)-te(i))/tn(i)).gt.eps) go to 99
7  continue
98 write(5,11) iter
11 format(2x,'iter=',i5/)
    write(5,12) (i,tn(i),i=1,n)
12 format(2x,i6,2x,1pe12.5)
    mi=2*n
    do 13 i=n+1,mi
        tn(i)=tn(mi-i+1)
13  continue
    do 15 i=1,mi
        x=real(i-1)*h/alx
        tn(i)=(tn(i)-tw)/qrt*(x-x*x)*6.
15  continue
    sum=0.0
    do 17 i=2,mi
        su=(tn(i)+tn(i-1))*h/2./alx
        sum=sum+su
17  continue
    write(5,18) sum
18 format(/'bulk temperature for monte carlo solution=',1pe11.4////)
    time2=etime(tarray)

```

```

time=time2-time1

time1=time2

write(5,39) time,sumt,sumt1

39 format(1x,'cpu time spent =',f9.3/1x,
      *'cpu time spent for monte carlo simulation=',f9.3/1x,
      *'cpu time spent for solving set of equations=',f9.3///)

692 continue

691 continue

690 continue

599 continue

      stop

      end

c

c

      subroutine fcn(tn,f,n)

      parameter (m=20)

      dimension tn(n),f(n),q(m),qgr(m)

      common /a1/qly,aky,h,alx,tw,q,qgr

      tn(1)=tw

      f(1)=0.0

      do 2 i=2,n-1

      x=real(i-1)*h/alx

      f(i)=qgr(i)-(tn(i-1)-2.*tn(i)+tn(i+1))*aky

      *+qly*(x-x**2)-q(i)

2 continue

```

```
x=real(n-1)*h/alx
```

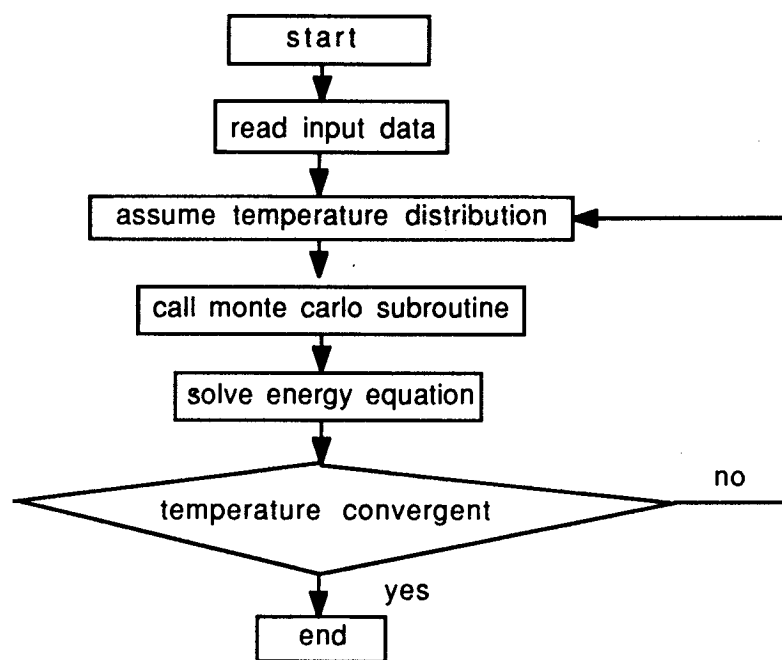
```
f(n)=qgr(n)-(tn(n-1)-2.*tn(n)+tn(n))*aky
```

```
*+qly*(x-x**2)-q(n)
```

```
return
```

```
end
```

## COMPUTER FLOW CHART FOR APPENDIX B



1 2 3 4 5 6 7 8 9 10 11 12 13 14 15 16 17 18 19 20 21 22 23 24 25 26 27 28 29 30 31 32 33 34 35 36 37 38 39 40 41 42 43 44 45 46 47 48 49 50 51 52 53 54 55 56 57 58 59 60 61 62 63 64 65 66 67 68 69 70 71 72 73 74 75 76 77 78 79 80 81 82 83 84 85 86 87 88 89 90 91 92 93 94 95 96 97 98 99 100